MASTER

An automated tuning mechanism for the racetrack microtron Eindhoven

de Wit, F.F.

Award date:
1999

Eindhoven University of Technology
Department of Applied Physics
Physics and Applications of Accelerators

An Automated Tuning Mechanism for the Racetrack Microtron Eindhoven

F.F. de Wit
VDF/NK 99-05

M.Sc Thesis February 1998 - February 1999

Supervision and guidance: Ir. W.H.C. Theuws
dr. J.I.M. Botman
Ir. S.R. Weijers
dr.Ir. M. Weiss

Summary

In the Eindhoven Racetrack Microtron, an electron accelerator, misalignments and magnetic-field imperfections are very important factors that influence the beam. Compared to other microtron projects, the approach to meet the required settings is different in the Racetrack Microtron Eindhoven (RTME). While other microtron projects aimed to reduce uncertainties and misalignments, e.g. by reducing magnetic-field inhomogeneities, using specially designed pole plates based on measured field maps, the aim of the RTME design is to keep tolerances within standard limits, taking additional design steps to counteract the errors. This makes construction cheaper and easier, but also puts more demands on correction schemes.

The function of the correction and tuning schemes is to adjust the parameter settings to counteract the influence of misalignments and correct setting errors. The basic strategy is to use 25 measured beam positions to tune the adjustable parameters.

The aim of the study presented in this report is finding an iterative mechanism using the measured beam positions for tuning the adjustable parameters to the values necessary to accelerate the beam of electrons from 10 to 75 MeV, while using as little iterations as possible.

To achieve this, a non-linear model-based feedback tuning mechanism was chosen. For this mechanism, simplified analytical models were developed, and the beam behaviour predicted by these was compared to the behaviour in the existing numerical model of the RTME that has no significant simplifications. The simplified models appeared to predict the beam behaviour insufficiently accurate to be used successfully in the tuning mechanism.

A suggested brute-force tuning algorithm, based on the numerical calculations of the beam behaviour, is outlined.

Contents

Preface

This report will present the results of research conducted on an automated tuning mechanism for the Racetrack Microtron Eindhoven (RTME). This electron accelerator, part of an accelerator chain, is being developped for use in experiments generating e.g. transition radiation. The tuning of the racetrack microtron is a complex problem for which an automated tuning mechanism was needed. Before formulating the tuning problem however, the layout of the machine, and certain important aspects about its functioning are explained (chapter 1). This is done because the tuning problem in itself is closely linked to the actual design and construction of the machine. At the end of this introductory chapter the scope of the report is formulated, and the chosen tuning strategy is explained further in chapter 2. The chapters 3 and 4 explain the type and structure of the models that were developed for the tuning strategy while chapter 5 compares the beam behaviour they predict to the calculated beam behaviour in the RTME, and outlines an alternate brute-force algorithm, based directly on the numerical calculated response. Chapter 6 presents the conclusions.

1 The Racetrack Microtron Eindhoven

1.1 The Racetrack Microtron accelerator chain

The Racetrack Microtron Eindhoven (RTME) is part of a larger set-up, originally intended to be used as an injection chain for an electron storage ring. Today it is further developed for future experiments for generating EM-radiation, e.g. transition radiation. The chain has three components: a travelling-wave linear electron accelerator, a beam-transport line, and the RTME. Though the main subject of this report is the tuning of the RTME, the other components of the accelerator chain will be discussed in the next sections too, before the RTME. This is done because these two systems determine the beam quality of the injection beam of the RTME which is important for the operation of the microtron. At the end of this introductory chapter the scope of the present report is presented.

1.2 The linac

The linac, shown in figure 1.1, is a medical accelerator that produces a beam of electrons with an energy of 10 MeV [5]. The electron source consists of a filament combined with an anode into an electron gun. A voltage of approximately 10 V is applied to this filament to heat it. Periodically both ends of the filament are put at a potential of -45kV and the electrons are accelerated in the electrical field between the filament and the grounded anode. This 45keV electron beam now enters the RF structure.

The -45kV pulse that operates the electron gun is also fed into the microwave source which generates a high power pulse that is guided into the disk-loaded travelling wave guide. The pulse duration has a typical length of 1 to 2 μs, at a microwave frequency of 2998 MHz. The disks, with circular irises in the centre, provide a longitudinal electrical-field component needed for acceleration, and slow down the Electro-Magnetic wave to match the phase velocity to the velocity of the electrons [6]. At the beginning of the beam path in the linac, the disks are closer to each other than at the end, the spacing increasing until the speed of the electrons is nearly constant. This is caused by relativistic effects as the electrons finally have a velocity very near to the speed of light.

The electrons are accelerated at the crest of the accelerating wave. Since only a limited area around the crest can give an appropriate acceleration, only pulsed

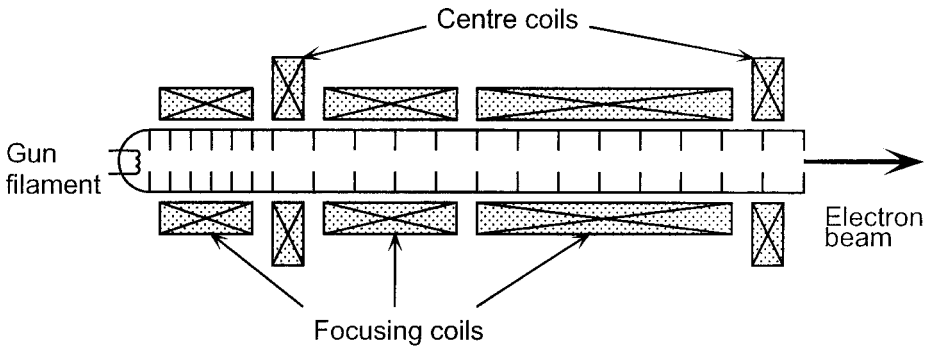

Figure 1.1: The travelling-wave 10MeV linac.

Table 1.1: General linac parameters

length[m]	2.25
accelerating frequency[MHz]	2998
pulse duration[μs]	1 to 2
power during pulse[MW]	2
final energy[MeV]	10
energy spread	3%

beams are possible. This pulse frequency must be distinguished from the pulsed RF power delivery.

As the power of the RF pulse is fixed, the final energy of the electrons is determined by the number of electrons generated in the electron gun. This number can be adjusted by changing the current through the filament. At two places the beam can be steered: behind the electron gun, and at the exit of the accelerator. The beam can be steered in horizontal and vertical direction, using air coils. There are three focussing solenoids that can be set separately.

It has been found that the steering coils behind the electron gun are not necessary to centre the beam so they are not used.

Table 1.1 summarises the main parameter values for the 10 MeV linac or linac-10. Gun filament current, and the current through all coils and solenoids will be adjusted to maximise beam current and centre the beam. The beam position is measured behind the accelerator.

1.3 Beam transport line

To transport the beam from the 10MeV-linac to the racetrack microtron a beam-transport line has been designed, shown in figure 1.2. This beam-line is doubly

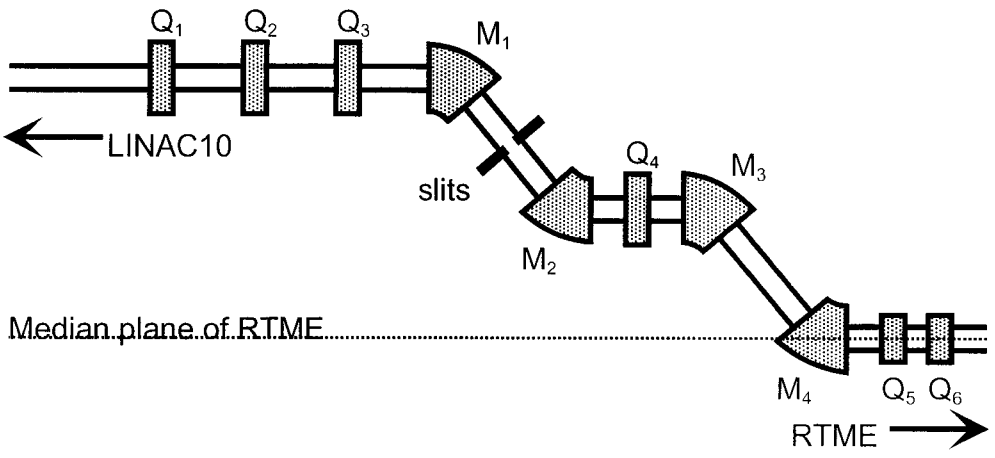

Figure 1.2: Beam transport line.

achromatic, meaning that the energy deviation of a particle does not influence its final position in transverse phase space after going through the entire set of elements.

The beam-line also has a negative dispersion, meaning that if the energy of a particle is larger, it will have a shorter path length and consequently a shorter transition time and so, the pulse stretches. This effect is compensated as the first part of the trajectory through the microtron (section 1.4), will compress the pulse again because the dispersion is positive [7]. All bending magnets have the same current source, yielding an identical, 50° bend. M_3 and M_4 can be adjusted relatively to that current. Between M_1 and M_2 a slit is placed. It is placed here because, due to dispersion in M_1 the particles with deviating energies fan out from the centre orbit. It is therefore possible to select an energy range by limiting the deviation of the particles that reach M_2 by placing the slit. To have a maximum beam current, M_1 and the parameters of the linac are tuned such that the maximum amount of particles passes through the slit. The energy profile of the beam is a Gaussian curve with a mean equal to the linac energy. As the energy doesn't change in the beam-line, the injection energy for the RTME, is determined by M_1,and therefore the excitation current through all bending magnets, and the energy profile of the linac. If the current is maximised, the mean energy will be equal to the linac energy as the majority of particles has an energy around the mean value. The slit limits the energy spread to 1%. This is necessary for injection into the microtron.

To adjust the position at the point of injection of the microtron the last two bending magnets, M_3 and M_4, will be adjusted. Also quadrupoles Q_5 and Q_6 have an added dipole field which can be used to adjust the horizontal direction [8]. The beam position will be measured at two locations on the microtron cavity axis, before and after the beam passes the acceleration cavity.

1.4 The racetrack microtron

The Eindhoven racetrack microtron is an electron accelerator, which will accelerate the electrons from 10 to 75 MeV. When an electron beam with an energy in the range of several tens to a few hundreds of MeV's is needed, the most commonly used machine is a linear accelerator. This will accelerate the particles in one straight line using one large RF-structure or several ones placed in line. A microtron uses one resonant acceleration cavity several times, and uses a magnetic field to guide the particles back to the entrance of the cavity. In a classical microtron this is done with one magnet, and the particles will have circular orbits. A racetrack microtron, like the one in Eindhoven, has two 180° bending magnets set apart at a small distance, that give the orbits the shape of a racetrack, hence the name. This gives the advantage of having more room to place the cavity, diagnostics and corrections.

For a racetrack microtron there are two important conditions. First, the orbits of the particles must be closed, and secondly the isochronism must be maintained. Because the beam has to be accelerated properly, it has to arrive at a specific phase with respect to the acceleration wave. Therefore the transition time of the first orbit must be equal to an integer number of periods of the microwaves in the acceleration cavity [1]:

$$t_1 = \frac{2L}{\beta_1 c} + \frac{2\pi}{B_r e c}(E_0 + E_{inj} + E_{cav}) = \frac{\mu}{f}, \tag{1.1}$$

with L the drift length between the two magnets, B_r the resonant magnetic field, E_0 the electron rest energy, E_{inj} the kinetic energy at injection. E_{cav} the energy gain in the cavity, β_1 the relative velocity with respect to the speed of light in the first orbit, and μ the so called initial mode number. The initial mode number is the length of the first orbit expressed in wavelengths of the accelerating microwaves. An equation like 1.1 can be made for every orbit, but they are dependent. The transition time between two successive orbits must also be an integer multiple. This difference in time exists through differences in speed, and differences in orbit length. The time difference between orbits n and $(n-1)$ is expressed as:

$$\Delta t = \frac{2L(\beta_{n-1} - \beta_n)}{\beta_{n-1}\beta_n c} + \frac{2\pi}{B_r e c^2} E_{cav} = \frac{\nu}{f}, \tag{1.2}$$

where ν is the so called incremental harmonic number, expressing the difference in length of two successive orbits, and β_n and β_{n-1} are the relative velocities in orbits n and $(n-1)$. Equations(1.1) and(1.2) are the conditions that indicate if the orbits are isochronous. These conditions can only be satisfied if the electrons are highly relativistic, i.e. $\beta_{n-1} = \beta_n = 1$ which eliminates the twelve equations for each orbit. The speed difference between orbits is now considered negligible. With this assumption two basic equations for a racetrack microtron can now be derived:

$$E_r = \left(\frac{\nu}{\mu - \nu - 2L/\lambda} \right) E_{inj}, \tag{1.3}$$

and

$$B_r = \frac{2\pi f}{ec^2} \frac{E_r}{\nu}, \tag{1.4}$$

where $\lambda = c/f$, the wavelength of the resonant frequency f in the cavity. The resonant acceleration frequency f is determined by the linac travelling wave guide resonant structure, and the injection energy, E_{inj}, is the result of the optimised current through the slit (section 1.3) which makes it equal to the mean beam energy. Because there are two equations and three parameters, either one of B_r, E_r or E_{inj} can be chosen freely. The sections 1.2 and 1.3 show that the adjustment of the linac-beam-line combination involves some extensive tuning E_{inj} has been chosen to be fixed at 10 MeV while the other two are derived from this value.

Both ν and N should be kept a small as possible to maximise phase acceptance and minimise the effect of repetitive errors such as field imperfections and cavity errors.

1.4.1 Two-sector magnets

The RTME has been designed with magnets that have two sectors which have different magnetic-field strengths, see figure 1.3. The sector below the tilted line is the low field sector, above the high field sector. This construction provides strong focussing at the sector edge because the beam passes this edge at a large angle which gives large edge focussing. The factor that gives the relative field difference between high and low field sector is indicated with a. Focussing is necessary to keep oscillation amplitudes small that would resonate if focussing were absent.

As a direct result from the choice to use two sectors the magnets must be tilted over a small angle to make the bend 180°, as shown in figure 1.3. Though this introduces a source of possible errors in the construction, since the additional small angle is more difficult to align than a simple 90° with respect to the cavity axis, edge focussing at the entrance and exit are a positive result.

The tilt angle, τ, can be calculated from the known geometrical features and design parameters by,

$$\tan\tau = \frac{\sin 2\theta}{(\frac{a+1}{a-1} - \cos 2\theta)}, \tag{1.5}$$

with θ the angle between the sector edge and the cavity axis, and a the relative strength of the high field against the low field sector.

Since a and θ can be chosen freely, they have been set to optimize acceptance [2]. B_L and therefor B_H must satisfy the following relations to the resonant field B_r:

$$B_L = \{\frac{1}{a} + \frac{1}{\pi}(1 - \frac{1}{a})(2\theta + \sin 2\theta)\} B_r. \tag{1.6}$$

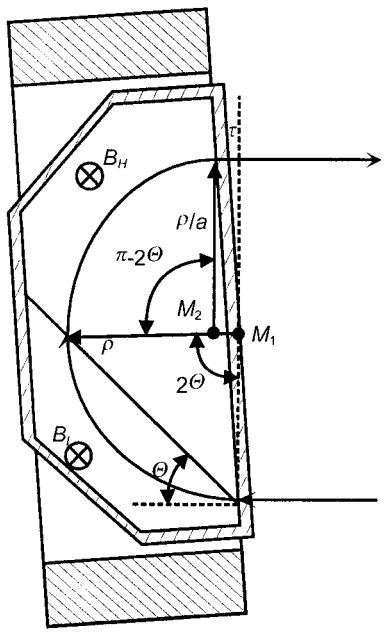

Figure 1.3: Two-field-sector magnet

and

$$B_H = aB_L = \{1 + \frac{1}{\pi}(a-1)(2\theta + \sin 2\theta)\}B_r. \tag{1.7}$$

The spatial extent of fringe fields has been assumed to be negligible. The design up to this point, not taking in account any inhomogeneities, would give a machine shown in figure 1.4.

This completes the design of the basic accelerator. The hard-edge values for the RTME-parameters can be found in table 1.2.

1.4.2 Beam position monitors

To check if the beam position is correct, two Beam Position Monitors (BPM's) have been placed in every orbit, and one near the point of extraction. They are located 30cm left and right of the correction dipoles, as can be seen in figure 1.4.

On basis of several considerations a stripline monitor has been chosen as the most convenient position monitor type [10]. As there are twelve complete orbits, and a monitor in the extraction orbit, the position is measured at 25 locations in the machine. This information is the primary input for tuning and beam positioning.

1.4.3 The correction magnets

As mentioned in the Scope, the intention of the RTME design was to use correction mechanisms to counteract errors and inaccuracies, and avoid complex hardware additions to minimise the uncertainties. The inhomogeneity of the bending magnets

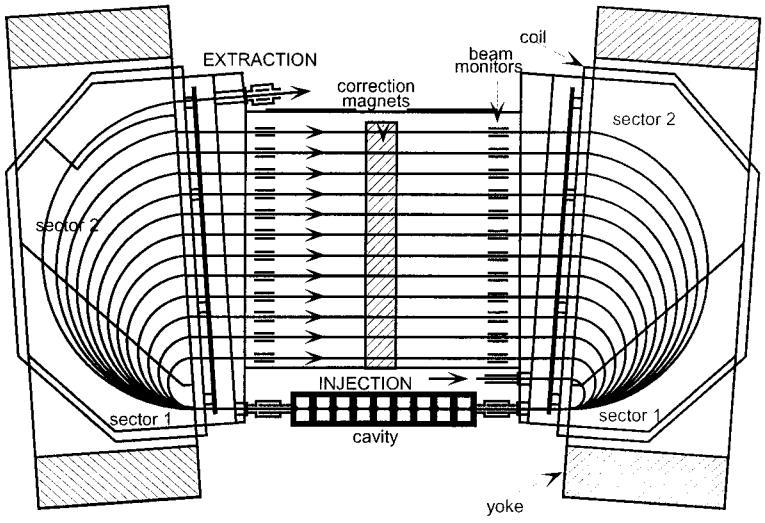

Figure 1.4: Layout of the RTME

is an important uncertainty. Impurities in the metal, and a field dip due to the large pole surface cause different beam direction errors because particles experience different fields during their path through the magnet. This will cause every orbit to exit the magnet with an angle ϕ_{exit}, making the total bend equal to $(180° - \phi_{exit})$. Also alignment of the magnets is important, since that could disturb the orbits too. In all three dimensions the magnets can have either a shift error or a rotation error. Webers [2] has demonstrated that, with the exception of the tilt angle in the horizontal plane, τ, all alignment accuracy's are well within the known maximal error limits.

These two errors both influence the beam by changing the direction. Therefore the effects can be compensated using correction dipoles placed in the centre of the drift between the bending magnets [2] (figure 1.4). These dipoles can now steer every orbit separately to close it.

The inhomogeneities give a different deviation angle for every orbit, while a tilt angle will give the same deviation angle for all orbits.

1.5 The numerical model

As mentioned in subsection 1.4.3, magnetic-field inhomogeneities can be expected for large magnets as used in the RTME. The resulting exit angles are so large that the beam would not reach the point of extraction if they were left uncompensated. To counteract these deviations, some of the parameter settings have been changed using a numerical model to simulate beam behaviour [2]. This model, called BANBA [9], was developed as a library of functions and procedures using Pascal. BANBA uses measured field maps of the bending magnets and an estimated fieldmap for the

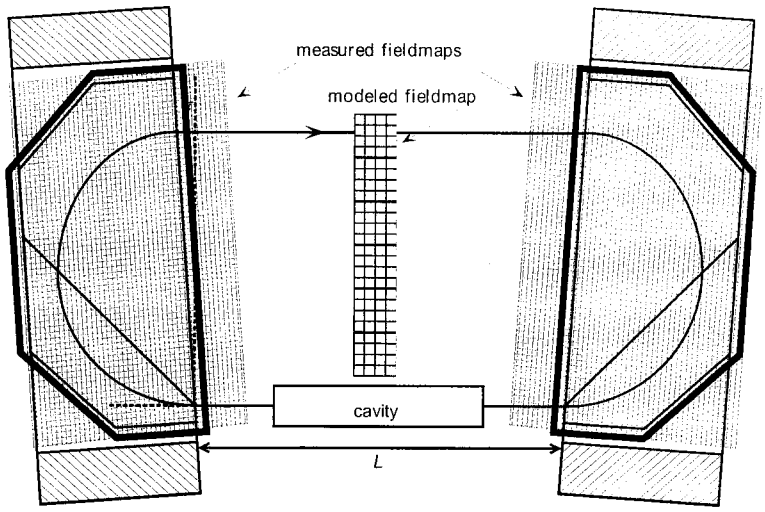

Figure 1.5: magnetic field maps used in model

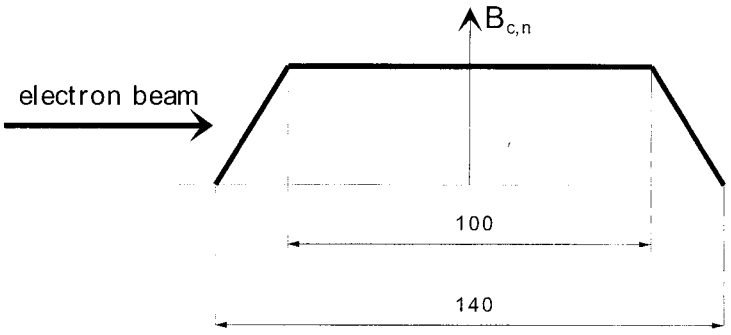

Figure 1.6: Profile of the magnetic field for correction magnets (dimensions in mm)

correction dipoles.(figure 1.5).

The correction dipole field maps have linearly increasing fringe fields to a homogeneous area. In figure 1.5 a profile of the magnetic field perpendicular to the median plane of the RTME is given.

The model uses a fourth-order Runge-Kutta integration to calculate the orbits from the equations of motion of a charged particle in a magnetic field. The particle motion in the cavity is calculated by using a model for the particle EM-field interaction [3]. The measurements of the bending magnet field maps showed that the average fields of the magnets were not entirely equal. A compensation factor was introduced to cope with that.

To determine the appropriate settings for the RTME parameters, these parameters were divided in two groups [2]: parameters that, after construction, can no longer be changed, and adjustable parameters. The first group contains for instance

Table 1.2: The RTME parameters

parameter	hard-edge	actual
Magnet dimensions $(l \times b \times h)$[mm^3]	$500 \times 1500 \times 450$	
resonant magnetic field, B_r [T]	0.524	
Low field, B_L [T]	0.511	
High field, B_H [T]	0.598	
Field ratio, a	1.17	
Sector angle, θ	45°	
mode number μ	26	
mode number ν	2	
electron energy at injection [MeV]	10	
electron energy at extraction [MeV]	75	
energy gain per turn [MeV]	5	
number of orbits	13	
RF frequency [MHz]	2998	
Tilt angle, τ [degrees]	4.48	4.00
Drift length, L [m]	0.990	0.985
Magnetic field strengths	100%	100.3% (left)
of bending magnets		102.3% (right)

τ and L, the tilt angle and distance between the magnets. It is important to consider that every dipole magnet will dissipate a certain amount of power. This power can be minimised by making sure that as little current as possible is used for correction. Therefore the tilt angle can be adjusted to mininise the average exit angle. The distance L was adjusted to make sure that isochronism was affected as little as possible, as the orbit length changed due to the tilting of the magnets.

The second stage involved adjustments of the magnetic fields of the left and right magnets, B_{left} and B_{right}, and the dipole correction magnets $B_{c,1..12}$. In an iterative process the bending magnetic fields were adjusted and the correction dipoles calculated. The values were readjusted when isochronism wasn't acceptable. After a few iterations a sufficient approximation of isochronism was reached [2]. The resulting values are given in tables 1.2 and 1.3

1.6 Scope

The use of the numerical model (section 1.5), demonstrates that if the errors are known. the settings can be calculated. When tuning the RTME however, the alignment errors are unknown, and parameter settings can be different from their actual value. Both can cause serious disturbance of the beam, and need to be corrected for. As the alignment errors can not be corrected directly, they need to be compensated by using the adjustable parameters. The tuning has to use the limited informa-

Table 1.3: dipole settings

n	$B_{c,n}$	n	$B_{c,n}$
1	105.480	7	274.609
2	200.159	8	234.375
3	226.965	9	182.617
4	268.286	10	77.393
5	280.444	11	-37.329
6	276.807	12	-229.053

tion of the position monitors (section 1.4.2), to find the settings for the adjustable parameters without knowing the errors in both alignment and settings.

This tuning problem will be formulated in chapter 2, and the definition of the adjustable parameters as it is used in the rest of the report is shown. The general approach and some possibilities for tuning are explored and The choice for a non-linear model based feedback strategy is explained. Chapter 3 shows the type of non-linear model used. The models developped to be used in the tuning mechanism are clarified in chapter 4, and their aplicability is shown in chapter 5. This chapter closes with a suggested brute-force algorithm based on the numerical calculations. The conclusions can be found in chapter 6.

2 The Tuning Problem

2.1 Tuning the RTME

The previous chapter showed that, knowing the magnet inhomogeneities, adjustments can be made to counteract the resulting deviations and calculating the effect with the numerical model from section 1.5. During this optimisation process adjustments were made to all parameters, including those who are fixed after construction. i.e. tilt angle τ and magnet spacing L. When tuning the RTME, alignment errors and parameter setting errors will have to be compensated by changing only the adjustable parameters, which does not include alignment parameters.

The tuning problem is formulated as:

All parameter settings have been calculated, but due to alignment errors and setting errors, the adjustable parameter settings have to be changed to position the beam such that it can be accelerated to 75 MeV.

It is important to note that errors can occur in both non-adjustable and adjustable settings, while the correction only can be done by using the latter. Also the limited information about the beam quality and position provided by the 25 Beam Position Monitors 1.4 is a complicating factor.

Before outlining the general tuning strategy, the tuning parameters are defined. This is done first to show the kind of quantities that need to be adjusted. This is important in the choice of the tuning strategy.

2.2 The parameters of the RTME

Equations(1.3) and (1.4) give the dependency between the energy gain in the cavity, E_r, the resonant magnetic field, B_r, and the injection energy. E_{inj}. As there are two equations and three unknown parameters, one can be chosen freely. As both linac and beam transport system have to be adjusted for every change in the injection energy (section 1.3), and as this is much more difficult to do than to change either the equivalent of B_r or E_r, this parameter has been chosen not to be varied. After optimisation of the beam current and alignment of the beam with the microtron

median plane, the parameters determining E_{inj}, i.e. the current through bending magnet M_1 and the linac parameters, are fixed.

To be able to adjust the beam position, it is preferable that all parameters are independent. In the case of the RTME-tuning this means that all parameters must be distinguishable in their influence on the beam. The bending magnets can both be set separately. However, they have a similar influence on the beam when their settings are deviated. When the magnetic field is increased in the left bending magnet, the radius of the semi-circular orbit is decreased and the orbit becomes shorter. Since the ideal orbit radius is larger than the radius for the higher field, the position at exit is now offset towards the cavity axis. Since the exit angle is dependent on the beam path through the magnet, it will also be changed with respect to the intended orbit. Though the beam passes through the right magnet in reversed direction compared with the left, a similar effect can be deduced. Here the displacement occurs on the cavity axis, and so does the exit angle. To see if this influence is also equal for the positions that are further in the beam path, the position measurements on two BPM's have been plotted against the magnetic field deviation for both magnets, as shown in figure 2.1. The BPM's have been numbered in the order that the beam passes. Therefore the first orbit contains numbers 1 and 2, and the twelfth orbit numbers 23 and 24. Number 25 is located at the point of extraction. The plots in figure 2.1 show the positions at BPM 9 and 25.

Gerlowski [4] has compared the variation of the left and right magnet and an alternative representation by the mean magnetic field, simply indicated by 'Mean', and the field difference, indicated by 'Diff'. Figure 2.2 shows that the plots for these parameters are quite different. This indicates that, in comparison with separating both magnet settings, the parameters Mean and Diff are more independent in their influence. To have a better view of what these parameters do, and to get a quantitative check of the independence, a step of 0.1% has been taken in each parameter and the positions at all 25 monitors have been plotted against their number. This gives an idea of the shape of the orbit, with respect to the ideal orbit. To check the independence and express this in a number, the 25 positions for each parameter, as plotted in figure 2.3, were put in four 25 dimensional vectors. The inner product between $\vec{u}$ and $\vec{v}$, can be expressed as:

$$\vec{u} \cdot \vec{v} = \mid \vec{u} \mid \cdot \mid \vec{v} \mid \cdot \cos\phi \tag{2.1}$$

yielding the angle between the vectors, ϕ. The inner product between the vector for left and right magnet deviations yields approximately 121.5° and for Mean and Diff, 109.1°. The vectors should be perpendicular, and obviously the Mean and Diff vectors are meet that criteria much closer than the other pair [4]. Mean is now indicated by M and Diff by D.

Having redefined the two parameters for the bending magnets, the two parameters associated with the cavity are defined i.e. the phase at injection and the

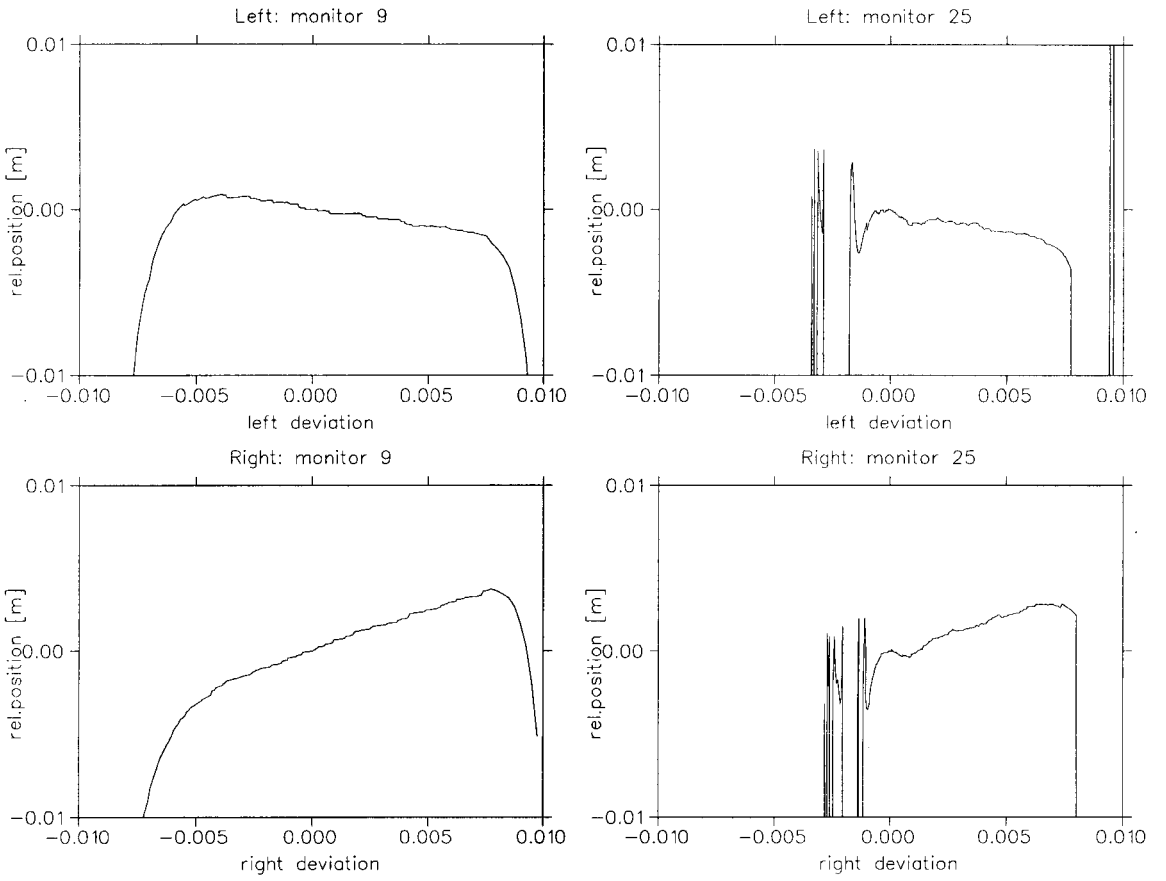

Figure 2.1: Responses left and right magnetic field deviations on BPM's 9 and 25

acceleration wave amplitude. It is important to note that if the phase of the acceleration wave in the cavity, at the moment the particles enter is within the stability range, from 0 to 18°, a particle will stay close enough to the ideal orbit and not be lost, given no further disturbances or errors. Though acceleration will not be exactly 5 MeV every time, the average will be close to that value. If this phase is outside the given region, the energy will either be too low or too high for the particle to pass through the first few orbits and it will be lost. This phase at injection with respect to the acceleration wave is indicated as P from now on. P can be changed by shifting the microwave phase, a problem however is that it can not be measured directly.

The amplitude of the acceleration wave is the second parameter connected to the cavity. With this parameter the amount of energy gained by a particle per passage through he cavity varies. This amplitude is indicated by E, because it is expressed in energy units rather than in potential units. The amplitude is directly linked to the amount of power guided into the acceleration cavity: more power means a higher amplitude.

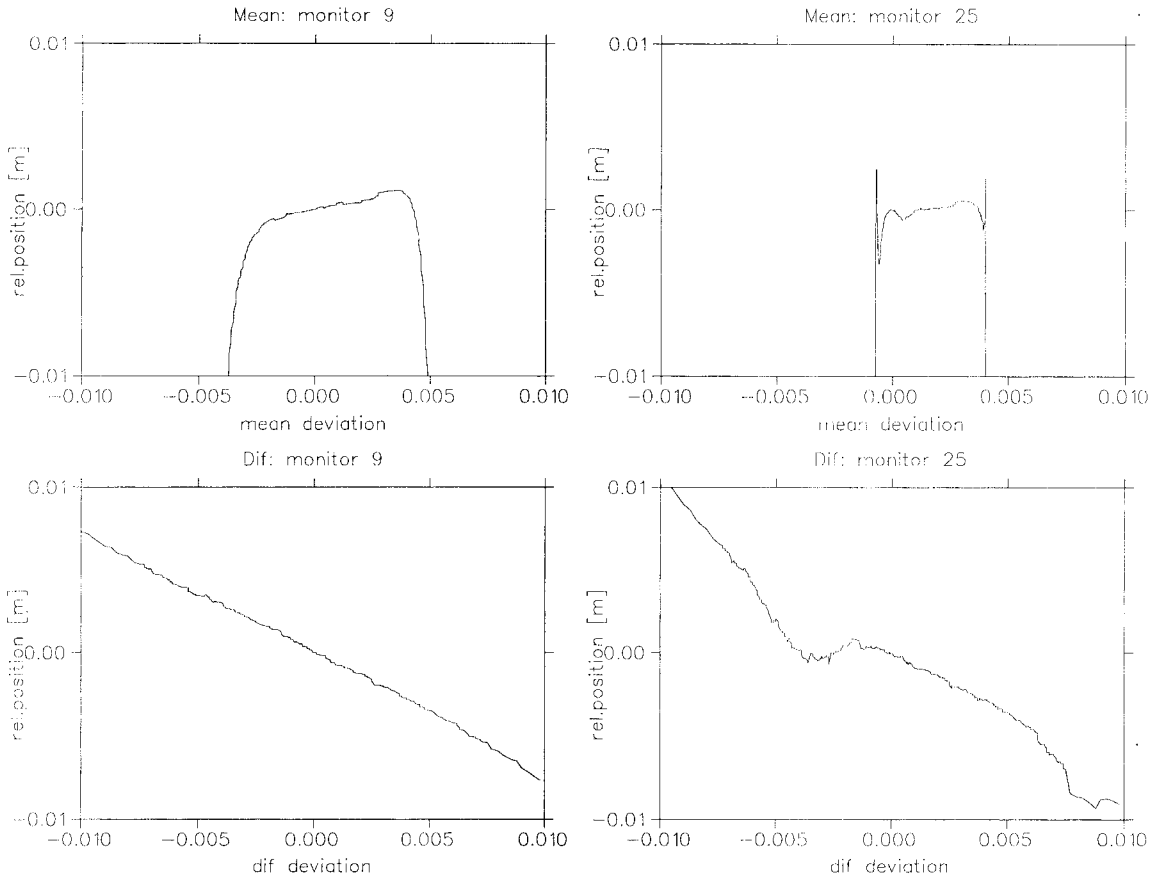

Figure 2.2: Responses 'Mean' and 'Diff' at monitors 9 and 25

Both settings are included into the RF power set-up of the linac-RTM combination. Figure 2.4 shows the positions for deviations of both P and E on BPM 9 and 25. As these are quite different, it is assumed that these parameters are independent.

The twelve correction dipoles are all separate parameters. There is a great difference between these twelve and the parameters M, D, P and E. The latter four have a repetitive effect, because the beam passes through magnets and cavity in every orbit. The correction dipoles only influence one orbit, and can cause changes in orbit obviously only after the beam passes them. On top of that, the influence is largely linear. The correction dipoles are numbered as they are passed by the beam, starting in orbit 1, with dipole 1. The dipoles will be indicated with $Dip1$ to $Dip12$. Because of their more general influence, M, D, P and E are indicated as 'main parameters'.

For the response of at all 25 monitors for all 16 parameters see internal report VDF/NK 99-06 [12]. A sample graph is shown in appendix B.

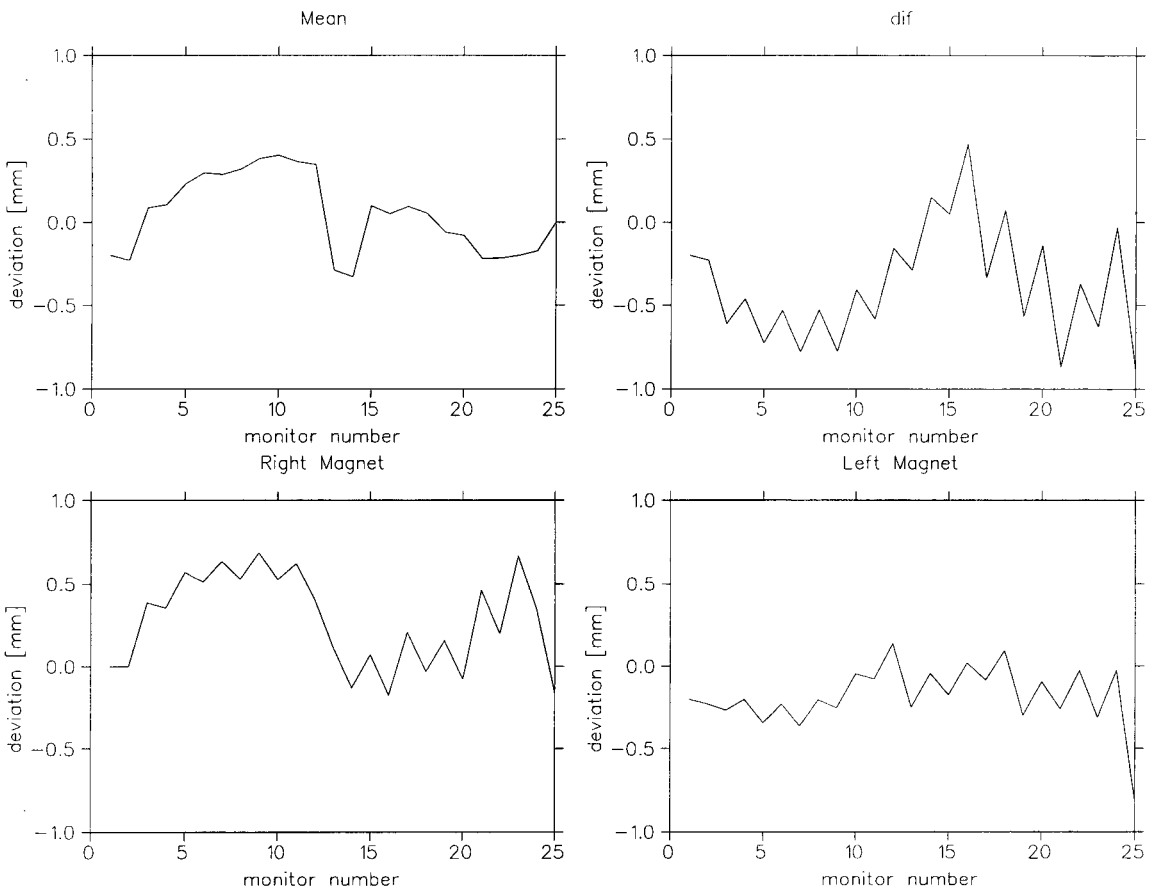

Figure 2.3: Relative orbits resulting from a 0.1% parameter deviation

2.3 Tuning strategies

For the RTME, an iterative feedback tuning has been chosen. It would not be usefull to inject an electron beam continuously, while changing the parameters. This could cause an extensive beam-loss and subsequently cause a great deal of excess radiation. To minimise the damage by this excess production of radiation, and of the beam loss, every iteration consists of a parameter setting, a position measurement and a calculation to find the adjustments. Only during the position measurement an electron beam is injected. This necessary lack of beam in the machine during the setting of the parameters and the calculations, and the long setting time of the bending magnets makes a dynamic control not very useful. Figure 2.5 explains the tuning scheme. The adjustments that have to be made to the parameters, can be calculated either directly or indirectly. The indirect calculation will try to find a representation of the known measured positions first using a fully modelled system, with no approximations or estimates. The numerical model from section 1.5 is an example of this kind of model. The representation or state estimate does not neces-

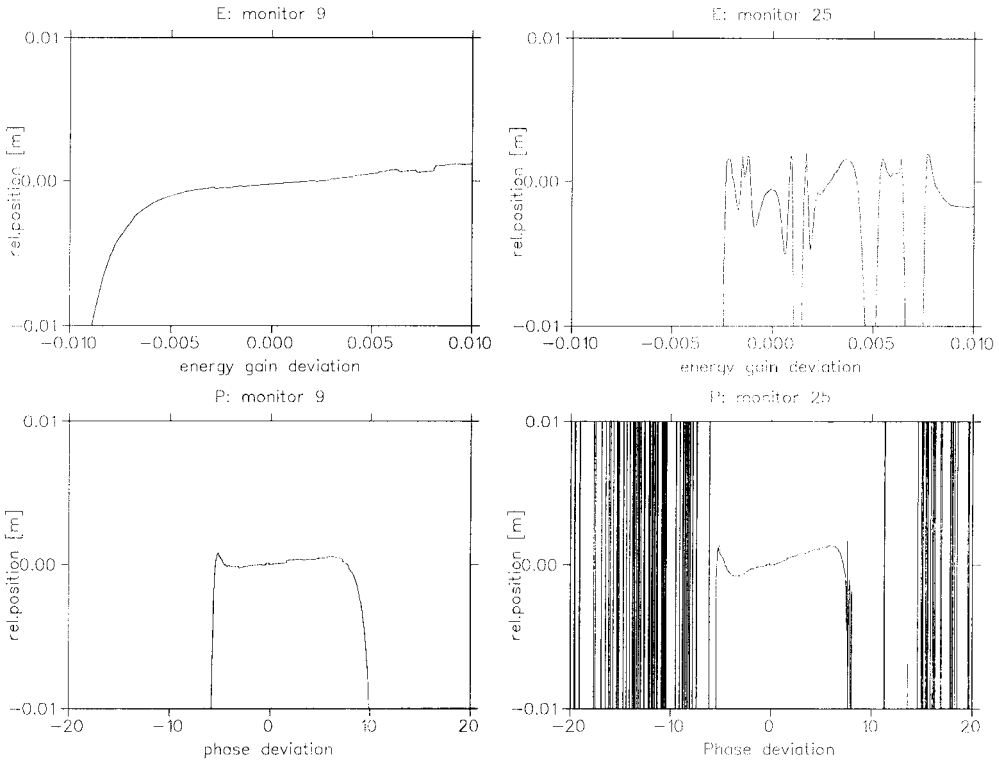

Figure 2.4: Responses for P and E at BPM 9 and 25

sarily have to represent the real existing state, but is a tool to come to an estimate of the orbit lengths and positions at the cavity entrance. With this information about the errors in isochronism and closed orbit condition, the parameter settings can be estimated. This method is relatively simple, but rather inefficient, because finding the state estimate is a labour-intensive process, while it does not yield the solution directly.

The direct method uses a simplified or reduced model, that is used to directly estimate the settings from the measured positions. Instead of trying to estimate the isochronism and closed orbit errors, their cause, the parameter setting errors, are estimated.

When a direct calculation of the parameters has to be done, a linearised 16×25 matrix that correlates parameters and positions could be used. This matrix would contain the conversion factors for the positions to the parameters based on small variations around a certain centre-point. Though this would be a very simple and direct method of tuning, it is not very useful in this case. The position plots for M and D in figure 2.2 show a very non-linear behaviour for relatively small deviations, and the choice of the centre-point can therefore drastically change the predicted values. As the setting inaccuracies for the parameters are not known, the centre-point is not clearly defined. The area in which the matrix would be applicable would

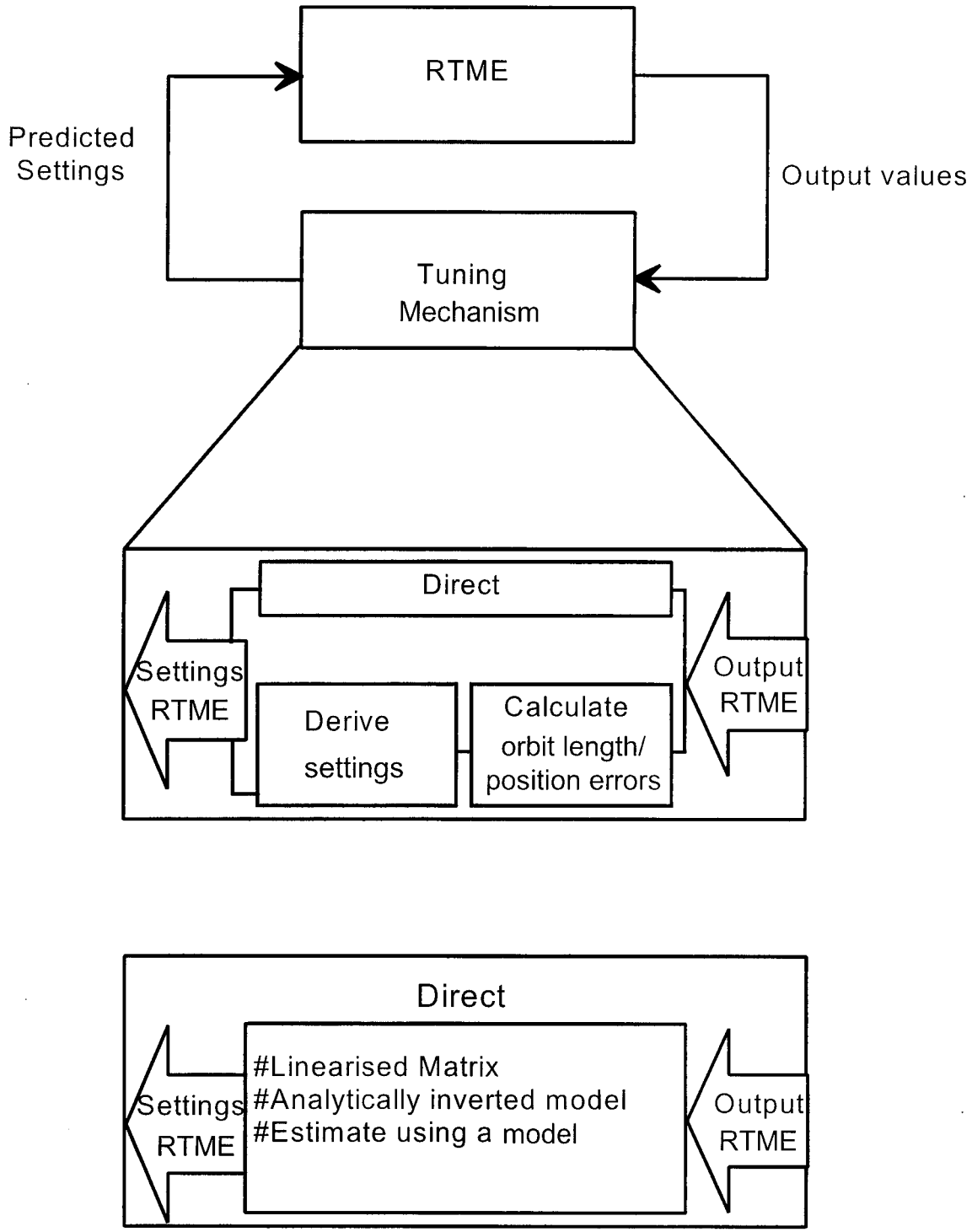

Figure 2.5: Tuning strategy: The tuning mechanism is specified into two possible approaches: direct and indirect. The lower rectangular gives several possibilities for the direct method.

Table 2.1: Parameter definitions

M	mean magnetic field bending magnets
D	magnetic field difference bending magnets
P	phase of the accelerating wave at the moment of injection
E	amplitude of the accelerating wave in energy units
$Dip1..12$	correction dipole fields

be small, making it necessary to develop a number of linearised matrixes to cover the range of values the parameter errors can take. Therefore a linear approach was discarded and a non-linear approach was taken. The basis of this non-linear tuning was a simplified model of the RTME, preferably analytical and invertable. If the model could be inverted directly, then the input of the positions would immediately yield the parameter settings for the RTME. A possible alternative using a non-invertable model would use this model to estimate the parameter settings while trying to minimise the difference between output of the model and the actual output of the RTME.

A non-linear, model based feedback mechanism, using a simplified model of the RTME for a direct parameter calculation, was chosen as the preferred method of tuning.

2.4 Concluding remarks

The tuning problem has been defined, and so have the adjustable parameters, summarised in table 2.1. For tuning, a non-linear, model based, feedback strategy has been chosen. The non-linear models can take many forms, which are outlined briefly in chapter 3.

3 Non-linear Modelling of the RTME

3.1 Classification of models

Non-linear models can be made in various levels of complexity. It is the amount of information about the modelled system used in the model, that gives a criterium of classification for these models.

The "Black Box" model is at one end of the scale. This type uses very little information about the internal mechanisms and dynamics of the system, and mostly tries to simulate behaviour by extrapolation, after using a sort of fitting procedure. This procedure adjusts the model parameters in such a way that, when given an input, it will emulate the output that would be give by the modelled system. This is continued until the model emulates the system close enough for the tuning strategy. A neural network representation of a system is a form of a Black Box model.

Black Box models are relatively easy to construct as no extensive knowledge about the internal processes of the system is necessary. They are not very flexible however, and outside a certain range they are inaccurate and inefficient, as they only have been 'trained' to emulate the response to a limited range of input.

At the opposite end of the scale is the "White" model. These types of models use extensive knowledge on internal dynamics and behaviour of a system. The system is described by modelling the actual processes inside, that are the fundamental causes of the behaviour. Not the input-output correlation is described, but the process itself, which does not explicitly limit the range of inputs the model can take. Though White models are harder to construct they are much more flexible and efficient than their Black Box counterparts.

An example of a White model is the numerical model described in section 1.5.

3.2 A "grey" model approach to the RTME tuning

For the feedback tuning strategy of the RTME we need to develop a model that is accurate in describing the processes inside the RTME, preferably analytical, and does not require a large calculation time. The White numerical model is not analytical due to the use of a numerical integration, and has an extensive calculation time up to hours. As a Black Box model would never be as accurate as a model based on the knowledge that is available of the machine, a "grey" model approach

was chosen. This model must contain an accurate description of the RTME, but have an analytical expression of these processes and a relatively short calculation time. The description chosen is one similar to geometrical electron-optics, which uses basic matrices that represent bends, drifts and lenses. This rules out however, the use of field maps in the description of the bending magnets which decreases the accuracy of the model.

3.3 Concluding remarks

For a tuning mechanism that is capable of compensating the many possible errors in the RTME settings and alignment an automated, non-linear, model based, feedback algorithm is chosen. The use of a simplified "grey" model is preferred above the numerical "white" model, and a "Black Box" model to keep efficiency and accuracy high but shorten the calculation time for tuning. A non-linear, preferably analytical model must be developed now. It is preferable that the model can also be inverted analytically, for optimum use in the feedback tuning strategy, this is not necessary however.

4 Description of the Applied Models

4.1 General outline of model structure

As mentioned in chapter 3, a mathematically less complex representation of the particle motion in the RTME has to be developed to get a model suitable for use in a feedback construction. Two models have been developed, with a different level of simplification. The model presented in section 4.2 ignores the two-sector magnet design and takes homogeneous magnets for the 180° bend. Assumptions for this model include the approximation of tilt by a small angle, which should be equal to zero for this magnet type. The second model (section 4.3) uses 'perfect' hard-edge two-sector magnets that have no fringe fields. Both models do not have inhomogeneities and they therefore have the racetrack shaped orbits that name this type of electron accelerator.

The model structure is based upon functions that each represent a basic electron-optical "element", i.e. a drift or a bend. Each function takes a six-dimensional input vector, x_{in}, and transforms it to a similar output vector x_{out}. As every element of x_{out} is expressed in the elements of x_{in} this is a transformation similar to that of a matrix though not, equal to those used in geometrical electron optics. These vectors look like this:

$$[\, x \; y \; x' \; y' \; s \; E \,] \tag{4.1}$$

Components x and y give the position of the particle in horizontal and vertical directions. To explain the co-ordinate system figure 4.1 shows the axes. They originate at the cavity, which is placed at the central line in the drift space between the magnets. The layout of a homogeneous magnet microtron, as discussed in section 4.2, is plotted in the background. For all discussed models the cavity is placed at a similar position, and the axes also originate there. The next pair, x' and y', give the direction expressed in a horizontal and a vertical component. These are also shown in figure 4.1 in the bottom half. Direction 1 has two positive components, pointing in the positive y and x direction. Direction 2 points in the exact opposite direction and therefore has two negative components, as shown in the figure. The two components x' and y' form a vector which length is normed at 1:

$$\sqrt{x'^2 + y'^2} = 1. \tag{4.2}$$

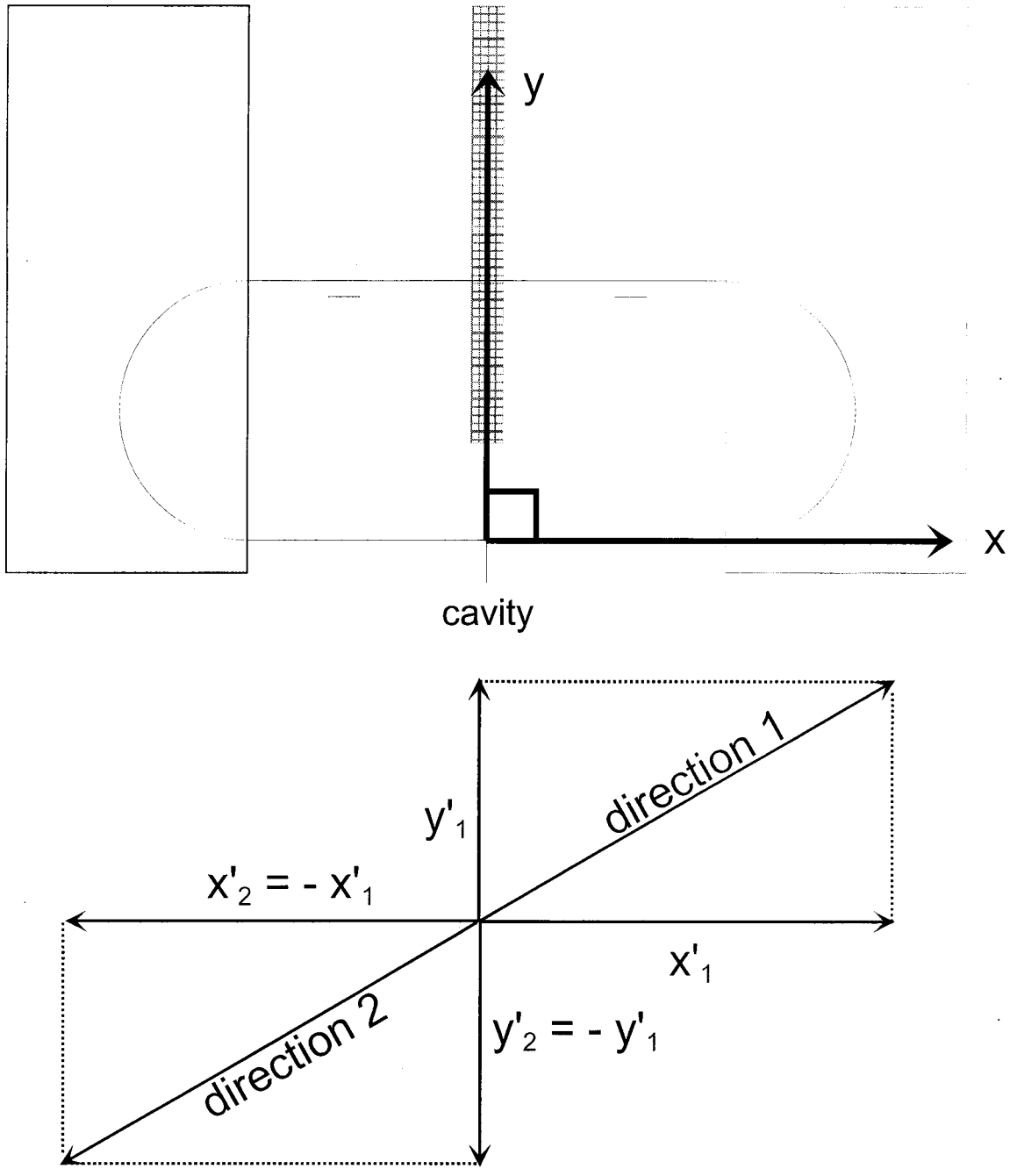

Figure 4.1: The used co-ordinate system

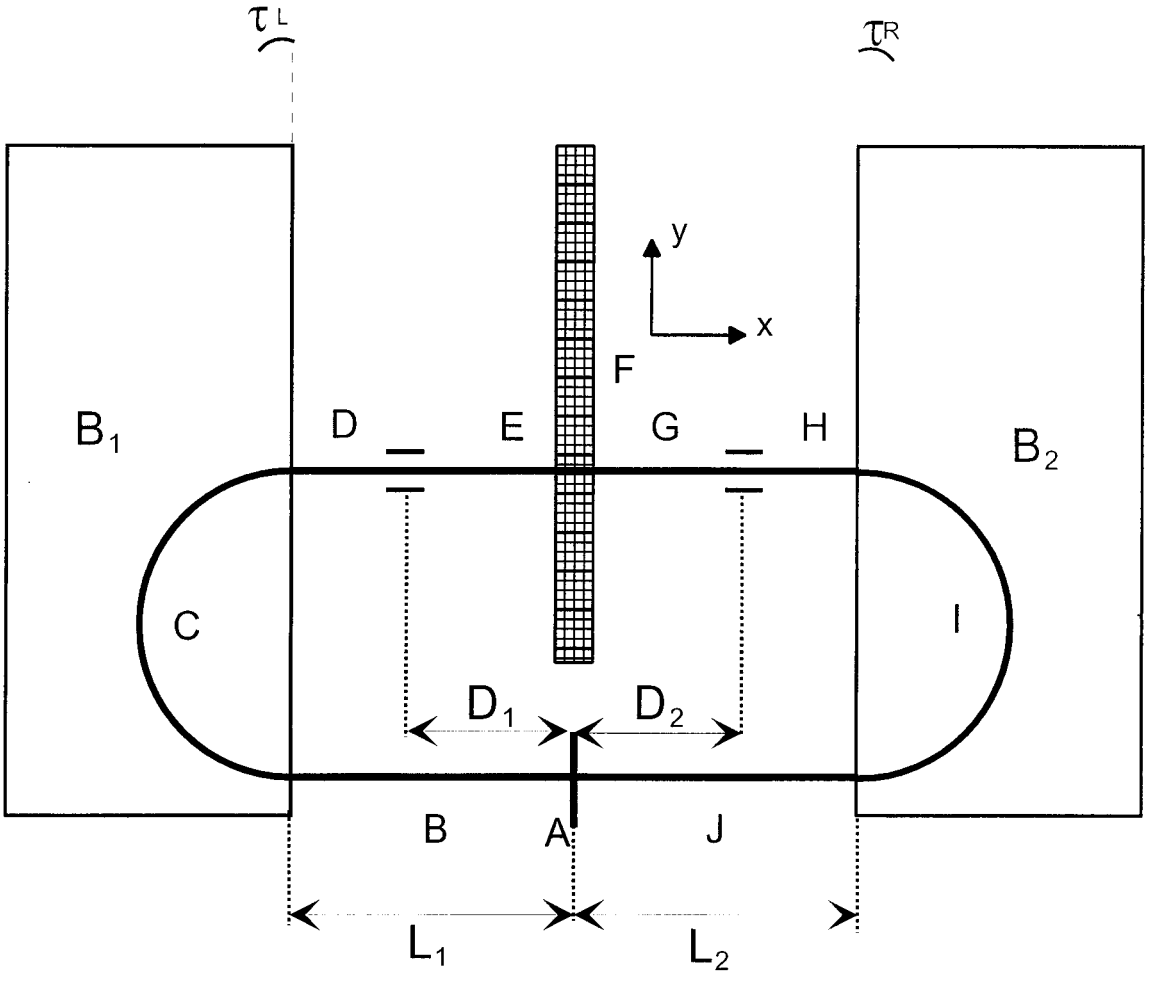

Figure 4.2: Homogeneous magnet model

The fifth component s represents the total distance the particle has travelled from injection, and E gives the total energy of the particle.

4.2 Homogeneous magnet model

As a first analytical model of the RTME behaviour, a model of one of the intermediate designs from chapter 1 was made, shown in figure 4.2. This model has hard edge, homogeneous magnets, which do not have field-sectors. The acceleration cavity used is assumed to be infinitely flat, and provides some focusing. These are the same assumptions as made in the numerical model. The correction magnets are also considered infinitely thin, and a small angle approximation is taken to calculate the direction change. The 180° bending magnets are not tilted. The magnet alignment errors are considered small only taken into account in the bend. The errors are

indicated with the angle τ_L and τ_R for left and right magnet.
Distances between cavity and both magnets are indicated by L_1 and L_2. The distance of the BPM's to the vertical axis is indicated by D_1 and D_2.

In figure 4.2 the letters A to J indicate functions which represent the transformations that were distinguished. In the following subsections these functions are described. Every property with sub-index 'i' is taken or derived from the incoming particle property vector x_{in}. When the sub-index is 'f' this is the resulting value for the outgoing particle, summarised in x_{out}.

Function A: cavity
In the model the acceleration cavity has been taken to be infinitely thin. The cavity model is based on a similar one made by Rosenzweig and Serafini [3]. In the model, which was developed by Webers [2], the assumption is made that $\beta = 1$, which simplifies the equations slightly because the time can be replaced by the orbit length s_i [2]. This is identical to the cavity model used for the numerical model.

First the energy gain and focussing are calculated:

$$\delta E = E_c \cos(\frac{s_i}{\lambda} \cdot 2\pi + \phi_c), \tag{4.3}$$

with λ the wavelength of the acceleration wave, and ϕ_c the phase at injection and,

$$\frac{1}{f} = -\frac{3}{8}\left(\frac{\delta E}{E_i}\right)^2 \frac{1}{Lcav}, \tag{4.4}$$

with f the focussing distance, and L_{cav} the length of the cavity. The outgoing particle has the following vector elements:

$$\begin{cases} x_f &= x_i = 0 \\ y_f &= y_i \\ x'_f &= -\sqrt{1 - {y'_f}^2} \\ y'_f &= y'_i - \frac{1}{f} \cdot y_i \\ s_f &= s_i \\ E_f &= E_i + \delta E \end{cases} \tag{4.5}$$

Function B: drift from cavity to magnet edge
This function describes a drift from $x = 0$ to $x = -L_1$. The alignment error τ_L is assumed to be negligible, and therefore not taken into account. The vertical position change is also assumed to be negligible, which yields that the path length s_f will only be influenced by the horizontal movement. These are the resulting final vector

elements:

$$\begin{cases} x_f &= -L_1 \\ y_f &= y_i - L_1 \frac{y'_i}{x'_i} \\ x'_f &= x'_i \\ y'_f &= y'_i \\ s_f &= s_i + L_1 \\ E_f &= E_i \end{cases} \tag{4.6}$$

Function C: left 180° bend

In the calculation of the radius of the orbit of a charged particle in a magnetic field β, the factor of the particle velocity and the speed of light, is taken in account. In this function it is assumed that $\beta = 1$ as the electrons are highly relativistic. Because

$$\gamma = 1 + \frac{E_i}{E_0} \tag{4.7}$$

for ρ this yields

$$\rho = \frac{\gamma \beta E_0}{B_1 e c} = \frac{E_0 + E_i}{B_1 e c} \tag{4.8}$$

with E_0 the rest energy of the electron, B_1 the left magnetic field, e the elementary charge, and c the speed of light. For the orbit length calculation it is also assumed that the particle will make a full 180° bend, which is equivalent to the assumption that y'_i is negligible at the entrance of the magnet, and the tilt angle τ_L is negligible. The tilt angle τ_L is only taken in account for the final direction components x'_f and y'_f. With these approximations the final vector becomes:

$$\begin{cases} x_f &= -L_1 \\ y_f &= y_i + 2\rho \\ x'_f &= -x'_i - \tau_L y'_i \\ y'_f &= y'_i - \tau_L x'_i \\ s_f &= s_i + \pi\rho \\ E_f &= E_i \end{cases} \tag{4.9}$$

Function D: drift from left magnet to left BPM

This is a drift to position $x = -D_1$. It is assumed that the initial horizontal position x_i is at the edge of the magnet, and that the magnet is not tilted. Therefore $x_i = -L_1$. Once again, y'_i is assumed to be negligibly small. Hence the orbit length

increases only with the horizontal distance $(L_1 - D_1)$. This yields:

$$\begin{cases} x_f &= -D_1 \\ y_f &= y_i + (L_1 - D_1)\frac{y'_i}{x'_i} \\ x'_f &= x'_i \\ y'_f &= y'_i \\ s_f &= s_i + (L_1 - D_1) \\ E_f &= E_i \end{cases} \tag{4.10}$$

Function E: drift from left BPM to correction magnet
A drift from $x = -D_1$ to $x = 0$. Assumptions are the same as for all other drifts i.e. vertical drift has a negligible influence on the path length. Therefore the final particle properties are:

$$\begin{cases} x_f &= 0 \\ y_f &= y_i + D_1\frac{y'_i}{x'_i} \\ x'_f &= x'_i \\ y'_f &= y'_i \\ s_f &= s_i + D_1 \\ E_f &= E_i \end{cases} \tag{4.11}$$

Function F: correction dipole
As the dipole is considered infinitely thin, it becomes a rotation of the direction vector $[x'_i, y'_i]$ over an angle k. The final direction can be expressed as:

$$\begin{cases} x'_f &= \cos k x'_i - \sin k y'_i \\ y'_f &= \sin k x'_i + \cos k y'_i \end{cases} . \tag{4.12}$$

Because k is considered small, the cosine and sine are approximated as: $\cos k = 1$ and $\sin k = k$. As the position doesn't alter, neither does the path length, and therefore this yields:

$$\begin{cases} x_f &= x_i = 0 \\ y_f &= y_i \\ x'_f &= x'_i - k y'_i \\ y'_f &= k x'_i + y'_i \\ s_f &= s_i \\ E_f &= E_i \end{cases} \tag{4.13}$$

Function G: drift from correction magnet to right BPM

Drift from $x = 0$ to $x = D_2$. The same assumptions as for all drifts are valid i.e. vertical drift does not affect the path length. This gives the following result:

$$\begin{cases} x_f &= D_2 \\ y_f &= y_i + D_2 \frac{y'_i}{x'_i} \\ x'_f &= x'_i \\ y'_f &= y'_i \\ s_f &= s_i + D_2 \\ E_f &= E_i \end{cases} \tag{4.14}$$

Function H: drift from right BPM to right magnet

Drift from $x = D_2$ to $x = L_2$, the magnet edge. As with function B, the tilt angle, τ_R, is assumed to be negligible, and therefore the drift will be unchanged. As in B the y'_i is assumed to be small and not of influence on the path length, which gives for the final vector:

$$\begin{cases} x_f &= L_2 \\ y_f &= y_i + (L_2 - D_2) \frac{y'_i}{x'_i} \\ x'_f &= x'_i \\ y'_f &= y'_i \\ s_f &= s_i + (L_2 - D_2) \\ E_f &= E_i \end{cases} \tag{4.15}$$

Function I: right 180° bend

The assumption that $\beta = 1$ made in function C, is also taken here. Therefore because:

$$\gamma = 1 + \frac{E_i}{E_0} \tag{4.16}$$

for ρ this yields:

$$\rho = \frac{\gamma \beta E_0}{B_2 e c} = \frac{E_0 + E_i}{B_2 e c} \tag{4.17}$$

with again E_0 the electron rest energy, B_2 the right magnetic field, e the elementary charge and c the speed of light. Because y'_i is assumed negligible, and the bend therefore is a full 180° the final particle properties are equal to:

$$\begin{cases} x_f &= L_2 \\ y_f &= y_i - 2\rho \\ x'_f &= -x'_i + \tau_R y'_i \\ y'_f &= \tau_R + y'_i \\ s_f &= s_i + \pi\rho \\ E_f &= E_i \end{cases} \tag{4.18}$$

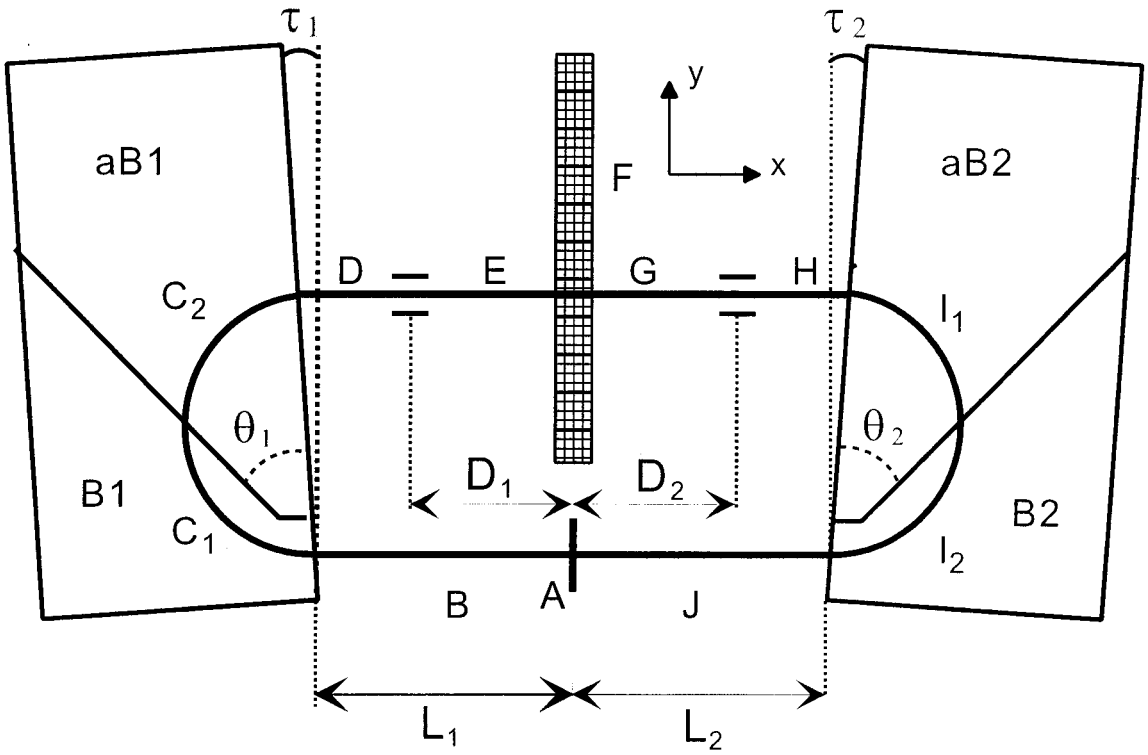

Figure 4.3: Two-field-sector magnet model

Function J: drift from right magnet to cavity
Drift from $x = L_2$ to $x = 0$. Assumption as above: no influence on path length of vertical direction.

$$\begin{cases} x_f &= 0 \\ y_f &= y_i - L_2 \frac{y'_i}{x'_i} \\ x'_f &= x'_i \\ y'_f &= y'_i \\ s_f &= s_i + L_2 \\ E_f &= E_i \end{cases} \tag{4.19}$$

4.3 Two-field-sector magnet model

The model shown in figure 4.3 is a hard-edge two-sector magnet model. the model has an idealised magnet structure, without fringe fields, and a perfectly homogeneous magnetic field, in each sector.

Tilt angles are indicated with τ_1 for the left magnet, and τ_2 for the right magnet. The angle of the sector edge to the magnet edge (see figure 4.3), is given by θ_1 for left and θ_2 for right. Distances are indicated as in figure 4.3: drift lengths by L_i

(left) and L_2 (right), distances from the vertical axis to the BPM's marked as D_1 and D_2, for respectively left and right.

In comparison with the homogeneous magnet model the two-sector magnet adds two more functions to the model, because every sector is calculated separately. The assumption that y' has no influence on the path length is dropped, as is obviously the assumption that τ_1 and τ_2 are negligibly small. The correction magnets do no longer take the assumption that the angle k is small.

Below the functions that are different from those in section 4.2 will be described, but some have minor changes and these will be described. refering to the corresponding functions in section 4.2.

Function B: drift from cavity to left magnet edge

The homogeneous magnets have a tilt that should be equal to zero. The two sector magnets are tilted however and if the beam is displaced vertically the drift-length changes slightly. To find the exact point where the beam enters the magnet, the intersection of the current orbit, and the magnet edge is calculated. A parametric representation of the particle orbit as soon as it leaves the cavity:

$$(x, y) = (0, y_i) + S(x'_i\ ,\ y'_i). \tag{4.20}$$

and of the magnet edge:

$$(x, y) = (-L_1, 0) + t(-\sin\tau_1\ ,\ \cos\tau_1) \tag{4.21}$$

This yields a set of equations:

$$\begin{cases} Sx'_i &= -L_1 - t\sin\tau_1 \\ y_i + Sy'_i &= t\cos\tau_1 \end{cases} \tag{4.22}$$

The solutions are:

$$t = \frac{y_i + Sy'_i}{\cos\tau_1}, \tag{4.23}$$

and

$$S = \frac{-L_1 - yi\tan\tau_1}{x'_i + y'_i\tan\tau_1} \tag{4.24}$$

S is the effective distance travelled by the particle and from this the horizontal and vertical distances can be calculated by multiplying them with respectively x'_i or y'_i.

Therefore we can derive the final properties as being:

$$\begin{cases} x_f &= Sx'_i \\ y_f &= y_i + Sy'_i \\ x'_f &= x'_i \\ y'_f &= y'_i \\ s_f &= s_i + S \\ E_f &= E_i \end{cases} \tag{4.25}$$

Function C_1: first bend in left magnet

The particle's orbit through the low field sector is part of a circle. As β is no longer assumed to be equal to one, the radius of the orbit is given by:

$$\rho = \frac{\gamma_i \beta_i E_0}{ecB_1}, \tag{4.26}$$

with e the elementary charge, c the speed of light, B_1 the field of the low field sector, and E_0 the electron rest energy. For γ_i and β_i we have the following relations:

$$\gamma_i = 1 + \frac{E_i}{E_0}, \tag{4.27}$$

and

$$\beta_i = \sqrt{1 - \frac{1}{{\gamma_i}^2}}. \tag{4.28}$$

The center of orbit (p, q) is given by:

$$(p, q) = (x_i, y_i) + \rho(y'_i\ ,\ -x'_i), \tag{4.29}$$

and therefore :

$$\begin{aligned} p &= x_i + \rho y'_i \\ q &= y_i - \rho x'_i \end{aligned} \tag{4.30}$$

The particle orbit can now be written as:

$$(x, y) = (p, q) + \rho(\cos\phi\ ,\ \sin\phi). \tag{4.31}$$

The parameter ϕ is the angle between the positive x-direction and the line connecting the centre of the circular movement $M_1 = (p, q)$, to the position of the particle. Figure 4.4 shows the situation for both bends in the left magnet. In the right half of the figure the definition of ϕ is shown. The orbit can now be calculated if the initial angle, ϕ_i and the final angle , ϕ_f are known. The sector edge, can be written as:

$$(x, y) = (-L_1, 0) + t(-\sin(\theta_1 + \tau_1)\ ,\ \cos(\theta_1 + \tau_1)) \tag{4.32}$$

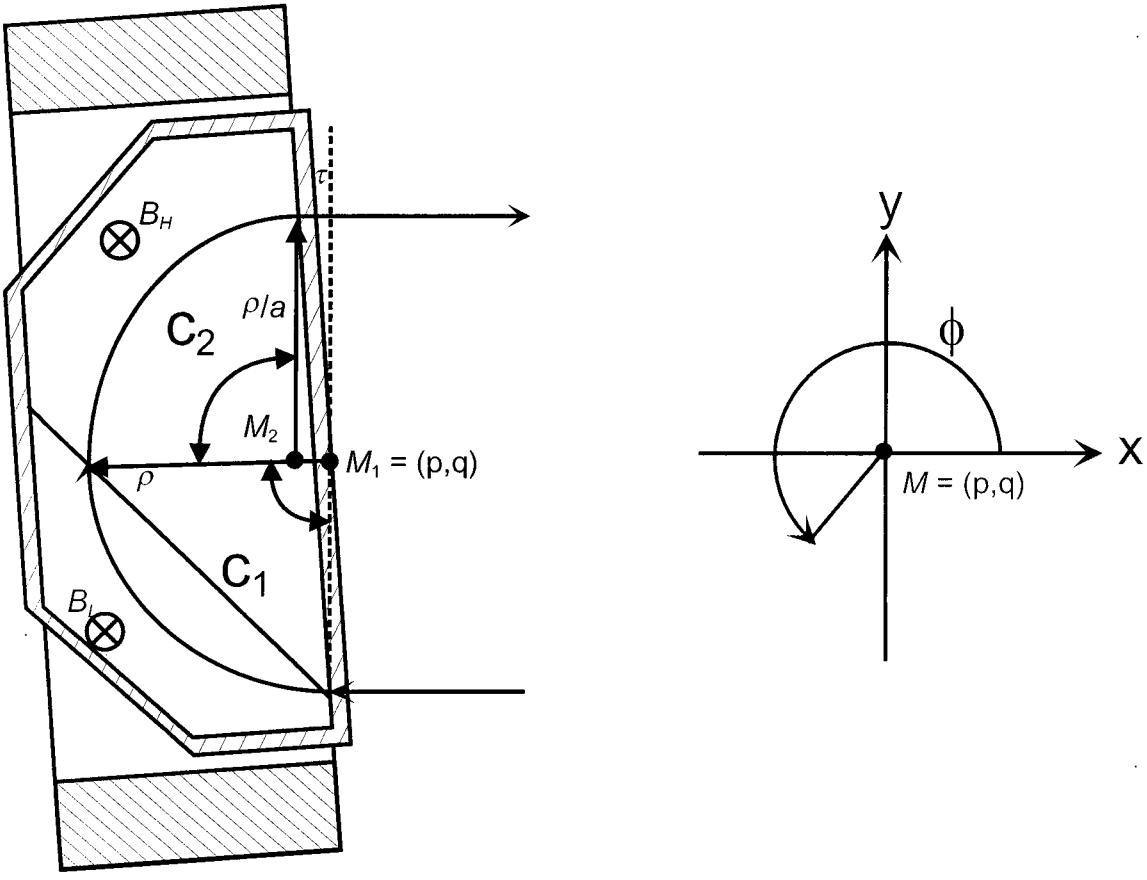

Figure 4.4: Situation for the partial bends

The parameter t is a position coordinate along the sector edge. The initial and final angle now have to be calculated. The initial angle is given by:

$$\phi_i = \frac{3}{2}\pi + \arctan(\frac{y'_i}{x'_i}) \tag{4.33}$$

As the particle describes an orbit that is a circle section, it is possible to describe the distance between particle and centre-point of this orbit in the radius ρ.

$$\rho^2 = (p - x_p)^2 + (q - y_p) \tag{4.34}$$

with x_p and y_p the horizontal and vertical particle position. If the sector edge representation (equation 4.32) is inserted in equation 4.34 and the result is worked out to factors of parameter t and simplified, this gives:

$$t^2 + 2\{(p + L_1)\sin(\theta_1 + \tau_1) - q\cos(\theta_1 + \tau_1)\}t + (p + L_1)^2 + q^2 - \rho^2 = 0, \tag{4.35}$$

and with:

$$b = 2\{(p + L_1)\sin(\theta_1 + \tau_1) - q\cos(\theta_1 + \tau_1)\}. \tag{4.36}$$

and

$$c = (p + L_1)^2 + q^2 - \rho^2, \tag{4.37}$$

this becomes:

$$t^2 + bt + c = 0. \tag{4.38}$$

Since the highest solution for t is sought we find:

$$t = -\frac{1}{2}b + \frac{1}{2}\sqrt{b^2 - 4c}. \tag{4.39}$$

With t the final position relative to the centre-point is calculated as:

$$x = (-L_1 - t\sin(\theta_1 + \tau_1)) - p. \tag{4.40}$$

and

$$y = t\cos(\theta_1 + \tau_1) - q. \tag{4.41}$$

The final angle ϕ_f then is:

$$\phi_f = \pi + arctan(\frac{y}{x}) \tag{4.42}$$

The final properties can now be calculated:

$$\begin{cases} x_f &= p + \rho\cos\phi_f \\ y_f &= q + \rho\sin\phi_f \\ x'_f &= \sin\phi_f \\ y'_f &= -\cos\phi_f \\ s_f &= s_i + \rho(\phi_i - \phi_f) \\ E_f &= E_i \end{cases} \tag{4.43}$$

Function C_2: second bend in left magnet

In this case the radius ρ is smaller by a factor $\frac{1}{a}$:

$$\rho = \frac{\gamma_i\beta_i E_0}{ecaB_1} \tag{4.44}$$

with a the factor between low and high field ($a = 1.17$). This bend is also shown in figure 4.4. The parametric representation of the orbit is the same as for Function C, and therefore we need to find the initial and final angle and the centre-point. For the initial angle it's largely the same as for the previous function:

$$\phi_i = \pi + \arctan(\frac{x'_i}{y'_i}) \tag{4.45}$$

as for the centre-point M_2:

$$\begin{aligned} p &= x_i + \rho y'_i \\ q &= y_i - \rho x'_i \end{aligned} \tag{4.46}$$

Instead of the sector edge, the magnet edge is now intersected. This can be expressed as equation 4.21:

$$(x, y) = (-L_1, 0) + t(-\sin\tau_1 \ , \ \cos\tau_1) \tag{4.47}$$

Here t is a co-ordinate giving the position along the magnet edge. With increasing t the position moves up from the cavity axis at $x = 0$. By the same principle as for Function C_1 the parameter t is calculated from:

$$t^2 + bt + c = 0 \tag{4.48}$$

with

$$\begin{aligned} b &= 2\{(p + L_1)\sin(\tau_1) - q\cos(\tau_1)\} \\ c &= (p + L_1)^2 + q^2 - \rho^2 \end{aligned} \tag{4.49}$$

which yields:

$$t = -\frac{1}{2}b + \frac{1}{2}\sqrt{b^2 - 4c}, \tag{4.50}$$

Calculation of the final position relative to the center-point:

$$\begin{aligned} x &= (-L_1 - t\sin(\tau_1) - p) \\ y &= t\cos(\tau_1) - q \end{aligned} \tag{4.51}$$

which gives for ϕ_f:

$$\phi_f = \frac{\pi}{2} - \arctan(\frac{x}{y}). \tag{4.52}$$

This gives us the following final properties:

$$\left\{ \begin{array}{rcl} x_f &=& p + \rho\cos\phi_f \\ y_f &=& q + \rho\sin\phi_f \\ x'_f &=& \sin\phi_f \\ y'_f &=& \cos\phi_f \\ s_f &=& s_i + \rho(\phi_i - \phi_f) \\ E_f &=& E_i \end{array} \right. \tag{4.53}$$

Function D: drift from magnet to left BPM

This is a drift to $x = -D_1$. Changes are limited to the orbit length calculation, which takes in account the initial position and the direction of the particle:

$$s_f = s_i + \frac{(-D_1 - x_i)}{x'_i} \tag{4.54}$$

The vertical position also uses the initial horizontal position instead of the assumed edge position in the Homogeneous magnet model:

$$y_f = y_i + (-D_1 - x_i)\frac{y'_i}{x'_i} \tag{4.55}$$

The other final particle properties remain the same.

Function E: Drift from BPM to correction magnet
Drift from $x = -D_1$ to $x = 0$. Changes are limited to the orbit length:

$$s_f = s_i + \frac{L_1}{x'_i}, \tag{4.56}$$

and the vertical position:

$$y_f = y_i + L_1\frac{y'_i}{x'_i} \tag{4.57}$$

Function F: correction magnet
In contrast with the homogeneous magnet model, the small angle approximation is not used here. Therefore equation (4.12) is fully valid without approximations. All other components stay the same, yielding:

$$\begin{cases} x_f &= 0 \\ y_f &= y_i \\ x'_f &= \cos kx'_i - \sin ky'_i \\ y'_f &= \sin kx'_i + \cos ky'_i \\ s_f &= s_i \\ E_f &= E_i \end{cases} \tag{4.58}$$

Function G: drift from correction magnet to right BPM
Drift from $x = 0$ to $x = D_2$. Again, no change except for y_f:

$$y_f = y_i + D_2\frac{y'_i}{x'_i}, \tag{4.59}$$

and s_i:

$$s_f = s_i + \frac{D_2}{x'_i} \tag{4.60}$$

Function H: drift from right BPM to right magnet edge
As in Function B the orbit and magnet edge are intersected. Parametric representation of the orbit:

$$(x, y) = (D_2, y_i) + S(x'_i\ ,\ y'_i). \tag{4.61}$$

and for the magnet edge:

$$(x, y) = (L_2, 0) \; + \; t(-\sin\tau_1 \; , \; \cos\tau_1) \tag{4.62}$$

This yields:

$$t = \frac{y_i + Sy'_i}{cos\tau_2}, \tag{4.63}$$

and

$$S = \frac{(L_2 - D_2) + y_i \tan\tau_2}{x'_i - y'_i \tan\tau_2} \tag{4.64}$$

The resulting final vector components:

$$\left\{ \begin{array}{rcl} x_f & = & D_2 \; + \; Sx'_i \\ y_f & = & y_i \; + \; Sy'_i \\ x'_f & = & x'_i \\ y'_f & = & y'_i \\ s_f & = & s_i \; + \; S \\ E_f & = & E_i \end{array} \right. \tag{4.65}$$

Function $\mathbf{I_1}$: first bend of right magnet

As the procedure is largely the same as in previous Functions C and D, the results will be reviewed briefly. A similar situation as in figure 4.4 is also valid here. The major difference is that the path through the magnet is traversed in opposite direction. So this first bend is through the high sector field. The method of parametric description of the orbits is the same: an initial and final angle,ϕ_i and ϕ_f are calculated with a similar scheme. With the radius this describes the orbit in the sector. The radius is given by:

$$\rho = \frac{\gamma_i \beta_i E_0}{eca B_2} \tag{4.66}$$

which yields for the centre-point co-ordinates:

$$\left\{ \begin{array}{rcl} p & = & x_i \; + \; \rho y'_i \\ q & = & y_i \; - \; \rho x'_i \end{array} \right. . \tag{4.67}$$

By the same procedure as in previous bends, the relative position of the particle is calculated and the particle distance to the centre point equalled to the radius ρ. This yields the equation for t, which gives the position along the sector edge:

$$t^2 \; + \; bt \; + \; c = 0 \tag{4.68}$$

with

$$\begin{array}{rcl} b & = & -2\{(p - L_2)\sin(\theta_2 + \tau_2) + q\cos(\theta_2 + \tau_2)\} \\ c & = & (p - L_2)^2 \; + \; q^2 \; - \; \rho^2 \end{array} . \tag{4.69}$$

This gives us the solution of t:

$$t = -\frac{1}{2}b + \frac{1}{2}\sqrt{b^2 - 4c}. \tag{4.70}$$

The initial angle is given by:

$$\phi_i = \frac{\pi}{2} + arctan(\frac{y'_i}{x'_i}), \tag{4.71}$$

and the final angle:

$$\phi_f = \arctan(\frac{y}{x}), \tag{4.72}$$

with:

$$\begin{array}{rcl} x & = & (L_2 + t\sin(\theta_2 + \tau_2)) - p \\ y & = & t\cos(\theta_2 + \tau_2) - q \end{array} \tag{4.73}$$

the final position relative to the centre-point (p, q). Final vector elements:

$$\left\{ \begin{array}{rcl} x_f & = & p + \rho\cos\phi_f \\ y_f & = & q + \rho\sin\phi_f \\ x'_f & = & \sin\phi_f \\ y'_f & = & -\cos\phi_f \\ s_f & = & s_i + \rho(\phi_i - \phi_f) \\ E_f & = & E_i \end{array} \right. \tag{4.74}$$

Function I_2: second bend in right magnet

As Function I_1 this calculation is a quite similar to the other bends. To calculate initial and final angles the orbit is intersected with the magnet edge. The parameter t, once more indicating the point of intersection as a co-ordinate along the magnet edge, must be calculated first. The steps are not explained as extensively compared to previous functions, as they are quite similar, and merely a change of parameters and a reverse of geometry is the main change. The equations needed for the calculation of the parameters are summarised. The radius:

$$\rho = \frac{\gamma_i\beta_i E_0}{ecB_2}. \tag{4.75}$$

The center point:

$$\begin{array}{rcl} p & = & x_i + \rho y'_i \\ q & = & y_i - \rho x'_i \end{array} \tag{4.76}$$

The equation,

$$t^2 + bt + c = 0 \tag{4.77}$$

with

$$\begin{array}{rcl} b & = & -2((p-L_2)\sin(\tau_2)+q\cos(\tau_2)) \\ c & = & (p-L_2)^2+q^2-\rho^2 \end{array} \tag{4.78}$$

yields the solution,

$$t=-\frac{1}{2}b-\frac{1}{2}\sqrt{b^2-4c}. \tag{4.79}$$

The equations for the initial angle:

$$\phi_i=\frac{\pi}{2}+\arctan(\frac{y'_i}{x'_i}), \tag{4.80}$$

and the final angle

$$\phi_f=\arctan(\frac{y}{x}), \tag{4.81}$$

with

$$\begin{array}{rcl} x & = & (L_2+t\sin(\tau_2))-p \\ y & = & t\cos(\tau_2)-q \end{array} \tag{4.82}$$

Altogether this yields:

$$\left\{\begin{array}{rcl} x_f & = & p+\rho\cos\phi_f \\ y_f & = & q+\rho\sin\phi_f \\ x'_f & = & \sin\phi_f \\ y'_f & = & -\cos\phi_f \\ s_f & = & s_i+\rho(\phi_f-\phi_i) \\ E_f & = & E_i \end{array}\right. \tag{4.83}$$

Function J: drift from right magnet to cavity
Drift to $x=0$. The horizontal drift distance is equal to x_i and here the vertical drift is taken in account for y_f and s_f:

$$y_f=y_i-x_i\frac{y'_i}{x'_i} \tag{4.84}$$

and

$$s_f=s_i-\frac{x_i}{x'_i} \tag{4.85}$$

4.4 Concluding remarks

The models described in this chapter used perfectly homogeneous magnets and no errors. The models were developed using a function as a basic unit. every function describing a basic element in the machine like a drift or a bend. Now that the models have been explained, the next step is to compare them to the numerical model. Chapter 5 will make this comparison on basis of parameter deviation response plots.

5 Assessment and Comparison of the Models

5.1 Comparing models

So far two kinds of models have been mentioned: A model based on the field-maps, to design the machine with corrections, and two simplified models, described in chapter 4. In the following we will indicate the first as 'numerical model', and the latter as 'simplified models' or by their names.

To compare the beam behaviour in the simplified models to that in the numerical model, the behaviour of the latter has to be described accurately. To get a view of what a single parameter variation does to the beam position at all 25 monitors, every parameter has been varied and the positions for each parameter value plotted. A set of 25 plots was displayed in one graph, showing the position relative to the ideal orbit, at all 25 BPM's for a specific range of parameter values which is characteristic for the magnitude of the error in that parameter.

First the numerical model is considered and its behaviour described. This will be followed by the comparison of the behaviour in the simplified models with the numerical model. Some additions to the models were made in an attempt to improve the similarities between numerical and simplified models. The adjusted models were also compared with the numerical model.
The description of beam behaviour of the beam has two aspects: a part that describes what the parameters do with respect to each other, and a general description which shows the behaviour of the parameters by themselves. Both aspects will be looked at.

5.2 Scaling of response plots

To show the behaviour of the beam position under influence of a deviated parameter, for all models the position was calculated with a known deviation of one parameter. The range over which each parameter was deviated is specific for the device to which the parameters are connected. For M and D this deviation range is chosen to be 1% because this is the characteristic size of errors in the magnet settings. It should be noted that this is not the inaccuracy of the homogeneity or the errors in machining

and construction that caused both magnets to have a different field strength. The latter has already been corrected for in the model, and is no longer present, and the first can not be corrected without going outside the scope of the design which does not include extra measures to decrease the errors beyond the magnitude of standard machining and construction. The error for M and for D is purely the setting of the current through the magnet coils after correction for their differences. For the simplified models there was no field strength difference. The maximum 1% deviation is indicated as 0.01 which therefore means 1.01 times the ideal setting. For P the variation range has been chosen from -20° to 20°. Though the exact number is arbitrary, the range of errors in P is some tens of degrees. For E a 1% deviation, indicated with 0.01 on the scale, has been chosen as estimate for the error range. The correction dipoles $Dip1$ to $Dip12$ were deviated with a maximum of 100 Gauss up and down from the calculated settings. This is an estimated range in which the dipoles will have to operate, rather than a error-range estimate. The plots of position against parameter deviation all use a vertical position axis that is limited to 1 cm up and down from the ideal orbit.

5.3 Beam behaviour in the numerical model

For a complete overview of responses for the numerical model see internal report VDF/NK 99-06 [12]. A sample is shown in appendix B. Example plots shown in this chapter use the same axes format. The vertical axis always displays the relative position with respect to the orbit of a perfectly aligned and tuned microtron but with inhomogeneities: the ideal orbit. This axis has been limited to a maximal deviation of 0.01m because this is the the dimension of the BPM radius. Any beam with a position deviation greater than this would be lost. The horizontal axis shows the parameter deviation. For M, D and E, a relative deviation is displayed. A value of 0.01 gives the position for a deviation of 1.01 times the ideal setting or a 1% deviation. For P the axis gives the value of the injection phase in degrees, and for the dipole variations it shows the setting in Gauss. A selection of the 25 measured positions has been made for each parameter.

Looking at the response plots, a strong similarity can be noted between the first few monitor plots of variable M and P (figure 5.1). The third plot of M corresponds with the first from P, and it seems that the positive M deviations corresponds with negative P. This behaviour can be explained by looking at what happens to the position at the first few monitors. When M is increased, the radius of the orbits within the magnets becomes smaller. This makes the beam have a negative position deviation on monitor 1, because the beam ends up lower on the vertical axis. Because of this smaller radius however, the orbit length decreases and the particle arrives too early, making the phase smaller. From this point it appears that the behaviour is temporarily governed by this P deviation, caused by the initial M deviation. The effect of the M deviation is apparently not strong enough to show through the P

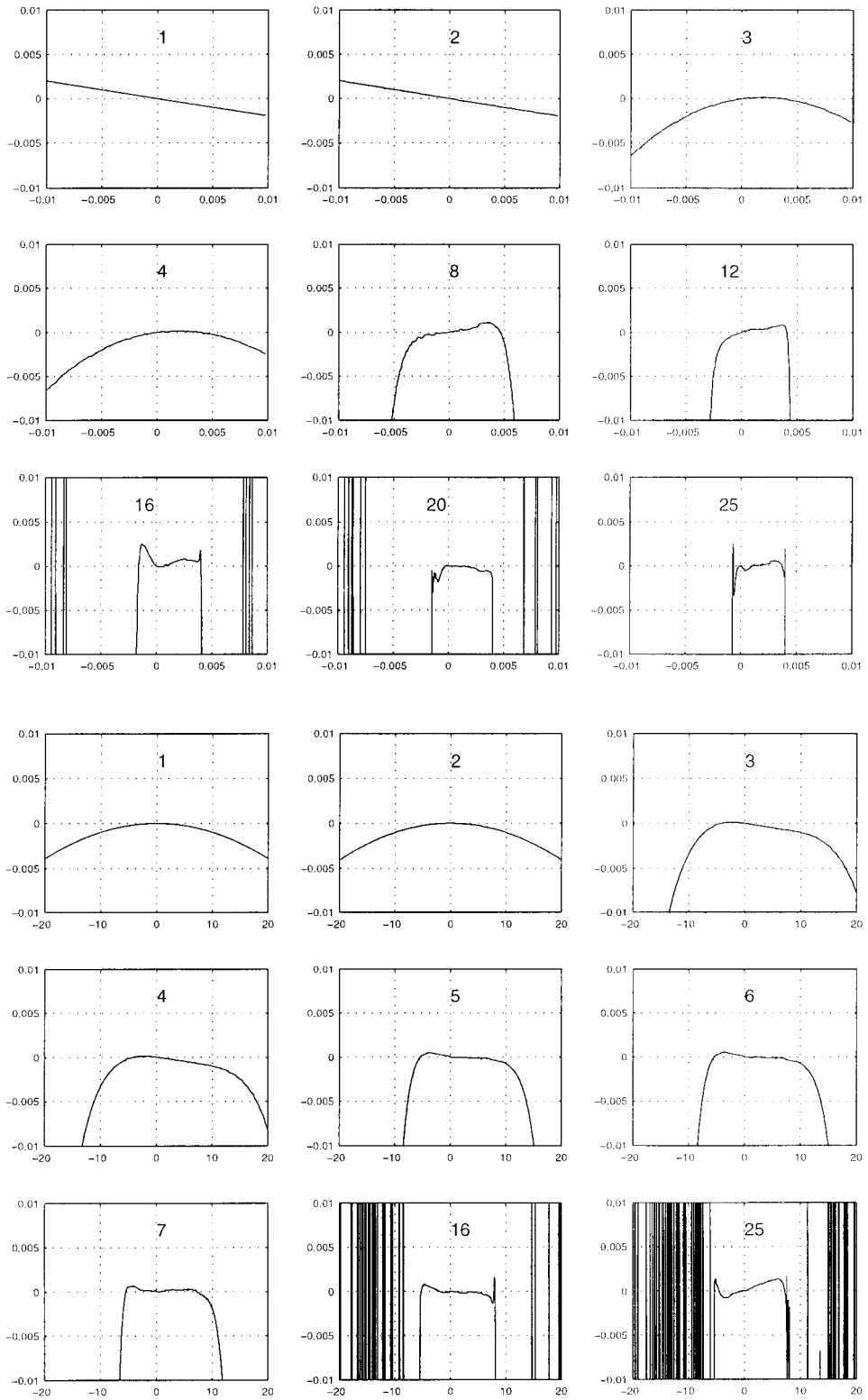

Figure 5.1: Characteristic plots M (top) and P (bottom) for numerical model

deviation effects. After a few orbits the behaviour changes however, and the M effects push through the P behaviour displayed in the first few orbits. The form of the plots stays similar, showing a 'plateau' structure, that is equal to the stabile area, within which the parameters M and P cause relatively small position deviations.

There is also a similarity between D and $Dip1$, displayed in figure 5.2. Both show a limited linear behaviour, though the dipole variation clearly has a much more narrow stability region. The similarity is also understandable here. D causes the position on the first monitor to shift, similar to M. It also will deviate the beam direction in a different way since the length and position of the trajectory through the magnet determines the exit angle. If therefore the D deviation changes the exit angle will move through a range of values as if being a correction magnet. This scanning however is not linearly dependent on the value of D, so though the semi-linear plots can be understood for low monitors, the linearity will disappear for higher monitors. Dip shows steep edges, which indicate beam loss for values around 20 Gauss at the last monitor. Apparently, the steering magnets change the direction so strongly it is lost quickly.

It is also apparent that the correction dipoles change the direction of the beam much stronger, which can be deduced from the fact that the beam is lost easily for higher dipole fields.

D has no 'plateau' structures. This can be understood if one looks at the fact that the orbit length is much lesser disturbed than for M. The latter changes the orbit length in both magnets, while D increases it in one and decreases it in the other, compensating the errors partially. The area within which the beam still reaches extraction will therefore be much broader for D than for M, or P. E, shown in figure 5.3 does have a plateau structure up to a degree, but only has the steep edge at the negative E axis. For high monitors the originally flat plateau has strong peaks. At extraction these peaks sometimes are larger than the BPM radius, indicating that this effect can cause beam loss in the last orbit.

The rest of the correction magnets give a similar response as the first one. As they have obviously no influence on the positions before them, it seems that the plots of $Dip1$ have shifted two places and are now displayed on an other monitor, though there are differences in the magnitude of positions, the width of the stability area and occasionally the shape of the plots. In the following paragraphs $Dip1$ will be examined primarily.

5.4 Homogeneous magnet model

M and P (figure 5.4) have similarities alike to those seen between these parameters in the numeric model. The position plot shape, matches for several monitors, but then differs. The plateau shape remains however. This indicates that the same physical process that causes this behaviour is present in the simplified homogeneous magnet model. This is consistent with the fact that the same cavity model has been

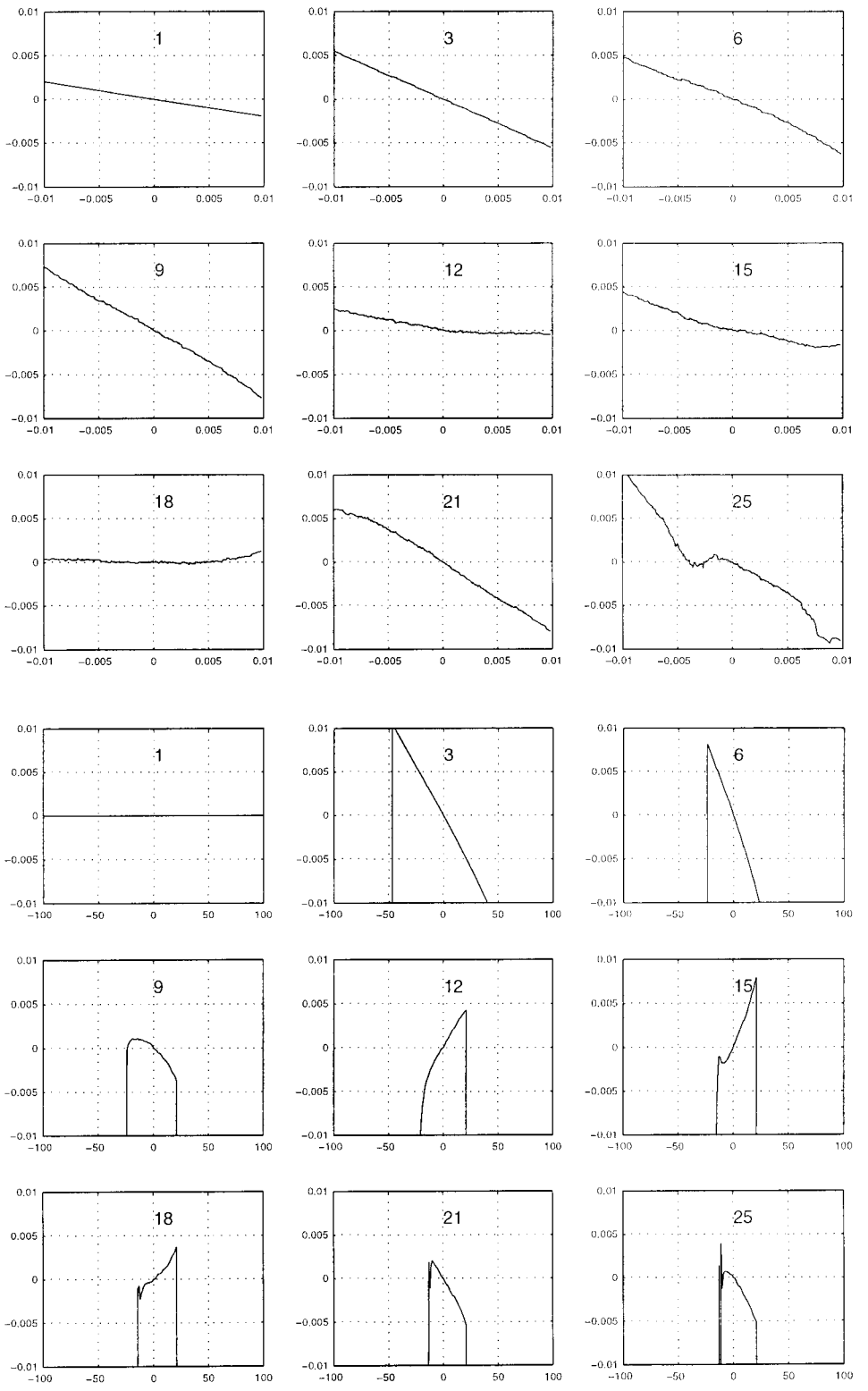

Figure 5.2: Characteristic plots D (top) and $Dip1$ (bottom) for numerical model

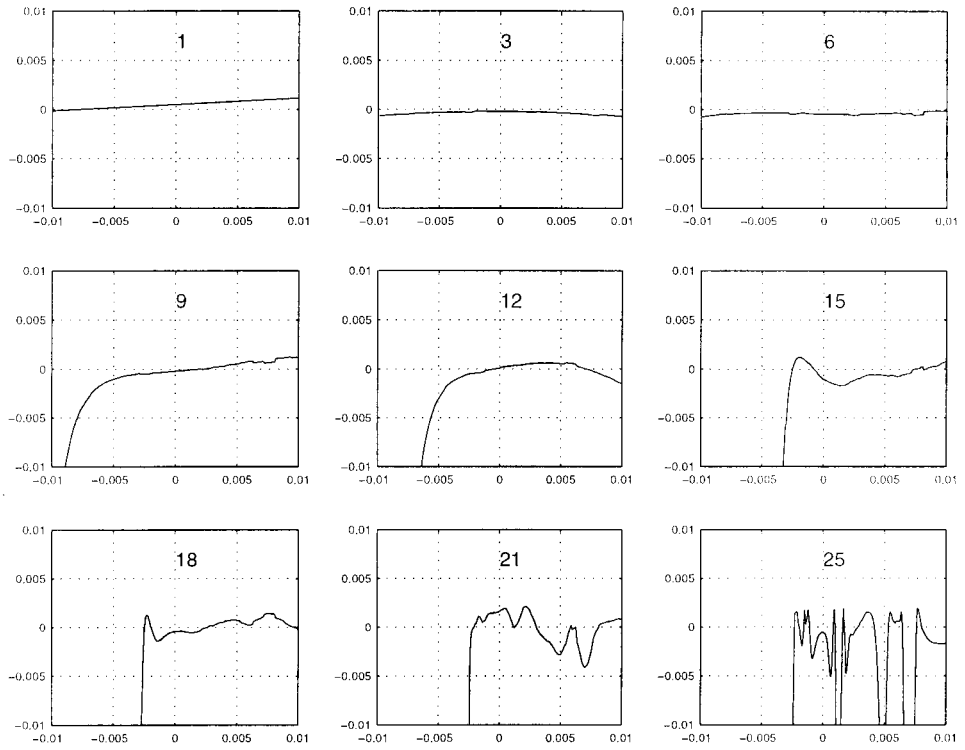

Figure 5.3: Characteristic plots E for numerical model

used as for the numerical model, and the orbit length and isochronism, is influenced strongly by changing the mean bending field.

When compared with the numerical model, M has similarities only up to monitor 6. This can be explained by the fact that the mean field deviation does not change any change in direction in the drift space between the magnets in this model, unlike the M deviations in the numerical model.

P has less similarities, though the shape of the plots resembles those of the numerical model. An explanation could be that the behaviour of beams injected at a different phase, is so much different from the behaviour in the numerical model, that this shows immediately. If this happens, the identical cavity model will not matter in comparing the behaviour. Especially if orbit length depends on P much differently than for the numerical model the behaviour shown at the measured positions will be different also.

D and $Dip1$(figure 5.5) are also similar. Both have a very narrow area within which the parameter value has to stay to get a position deviation within the monitor at all locations. Especially at monitor numbers above 12 this can be seen.

D is strongly linear, which can be expected because in this case it only causes

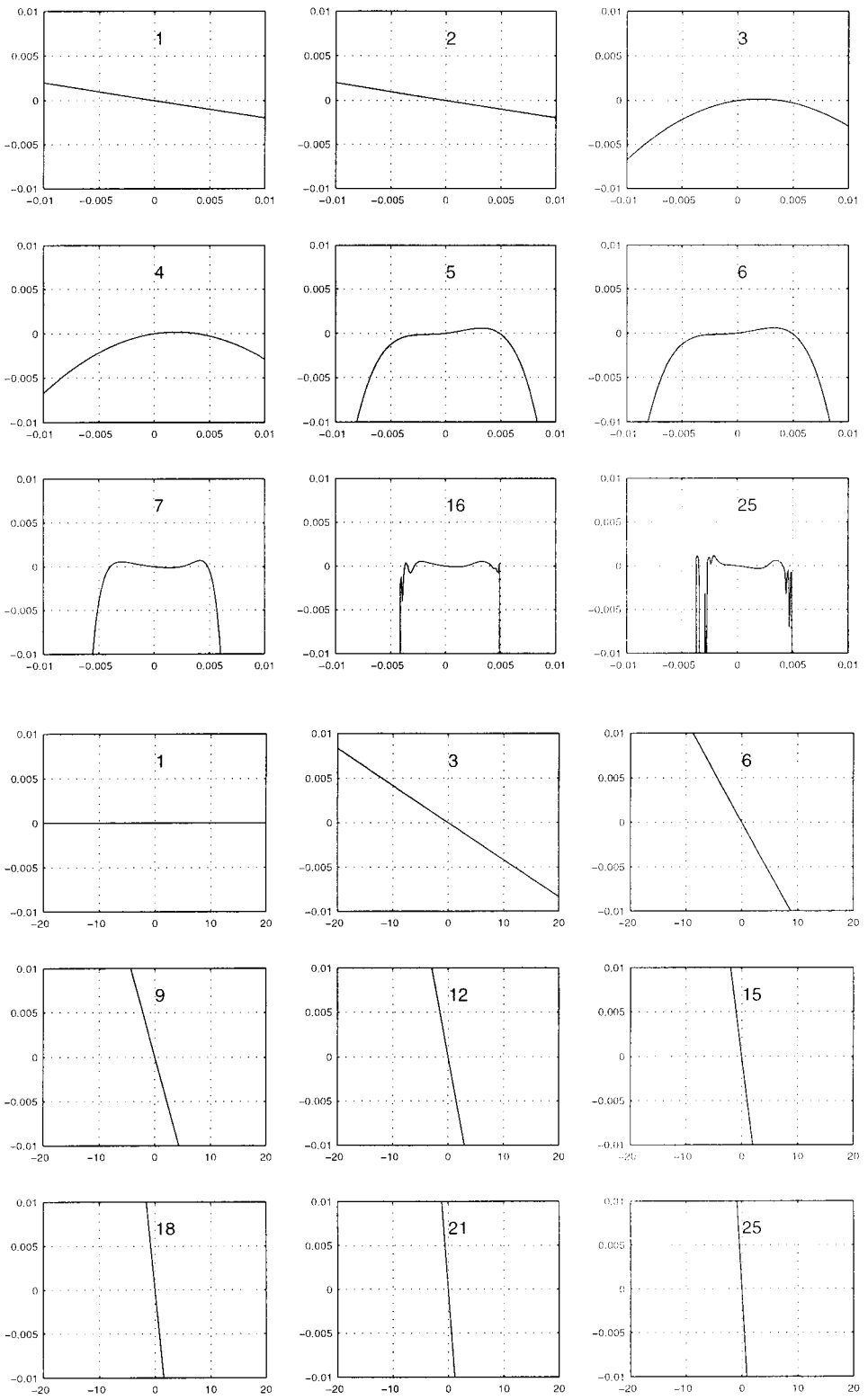

Figure 5.4: Characteristic plots M (top) and P (bottom) for simplified homogeneous magnet model

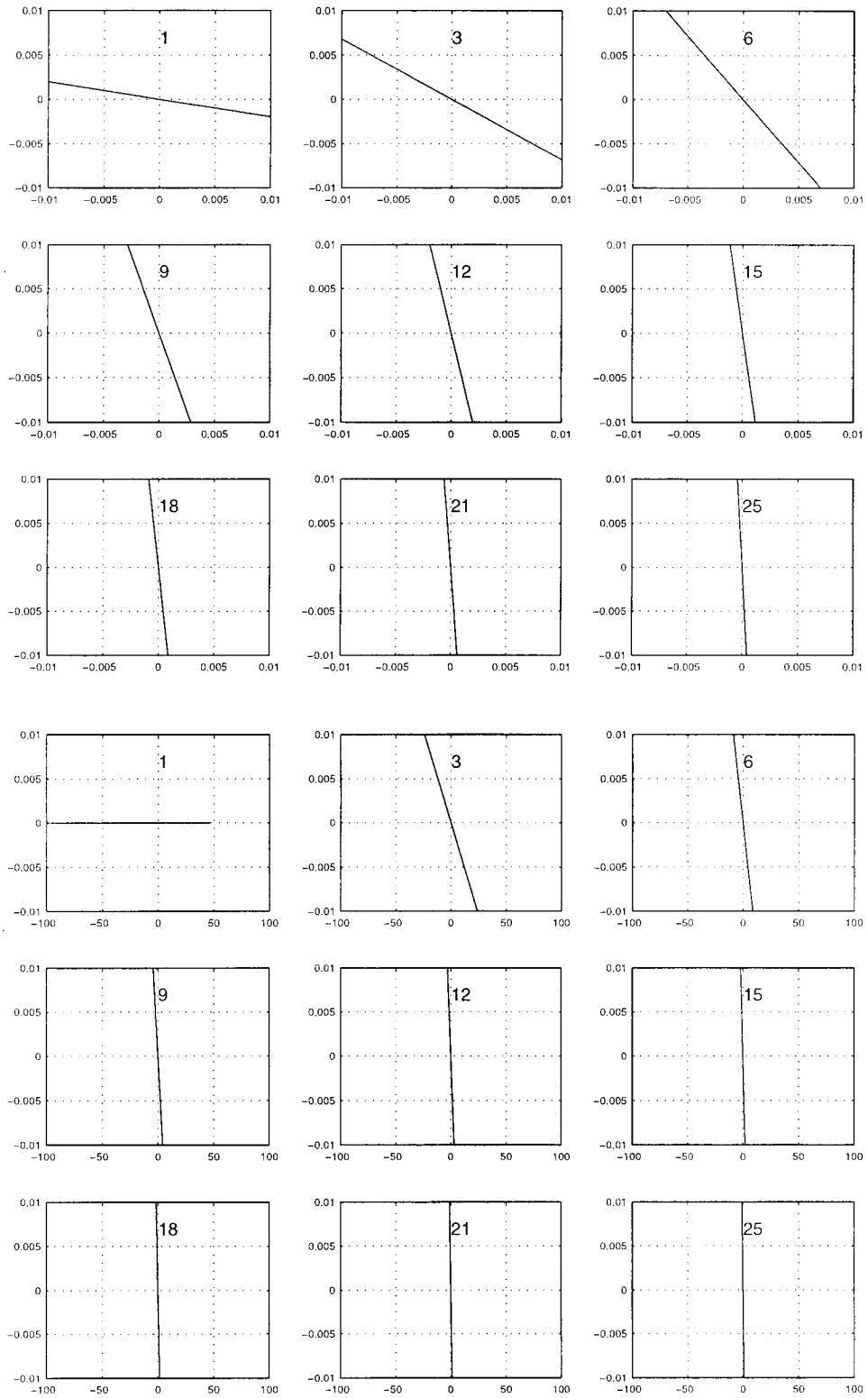

Figure 5.5: Characteristic plots D and $Dip1$ for simplified homogeneous magnet model

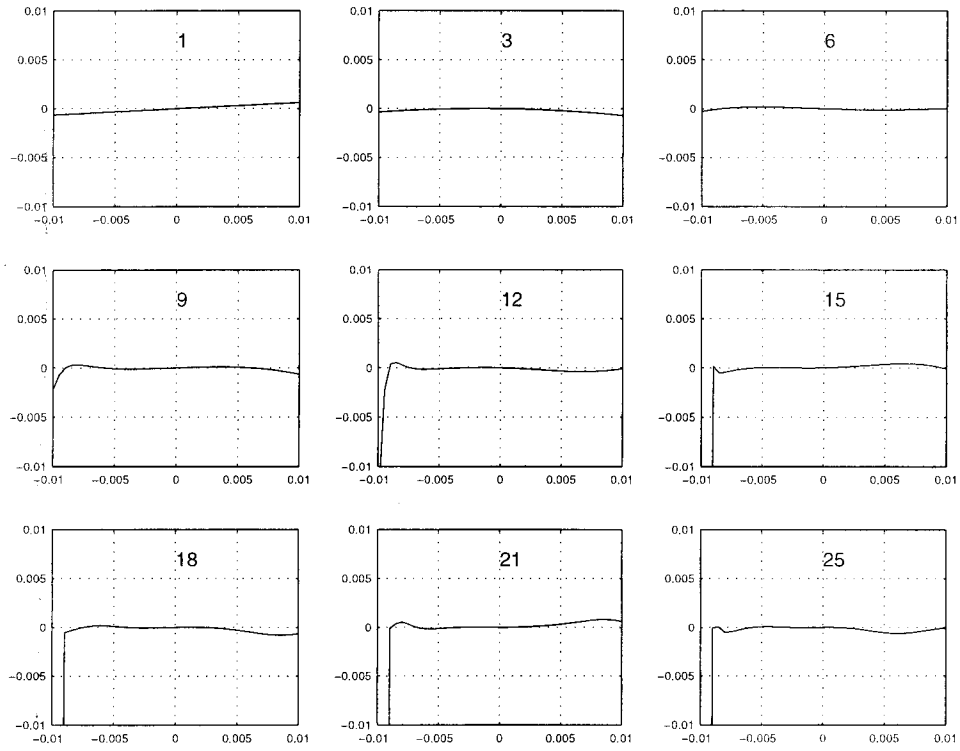

Figure 5.6: Characteristic plots E for simplified homogeneous magnet model

a displacement dependent on the magnetic field difference. Therefore non linear behaviour is not seen in this parameter. *Dip*1 does not show the behaviour that is seen in the numerical model. Especially the narrow band of values that gives a position deviation within the set limit of the BPM radius, is not consistent with the numerical model. E, as seen in figure 5.6 has no edge, but does show some undulations on the plateau. It is possible that increasing the energy does not cause the serious disturbances in beam behaviour because phase stability stays intact. The increased energy gain might not be large enough to cause an orbit length error needed to cause beam loss.

5.5 Additions to the homogeneous magnet model

In the numerical model some effects of inhomogeneities and geometry cause specific behaviour. As mentioned, the orbits are influenced differently by the inhomogeneities, and therefore each have different exit angles when leaving the magnet. Because of this the particles are not entering the drift with directions parallel with the cavity axis. The dipoles have to be used to correct the direction of the beam to close the orbits, but the orbit length is no longer exactly an integer number of

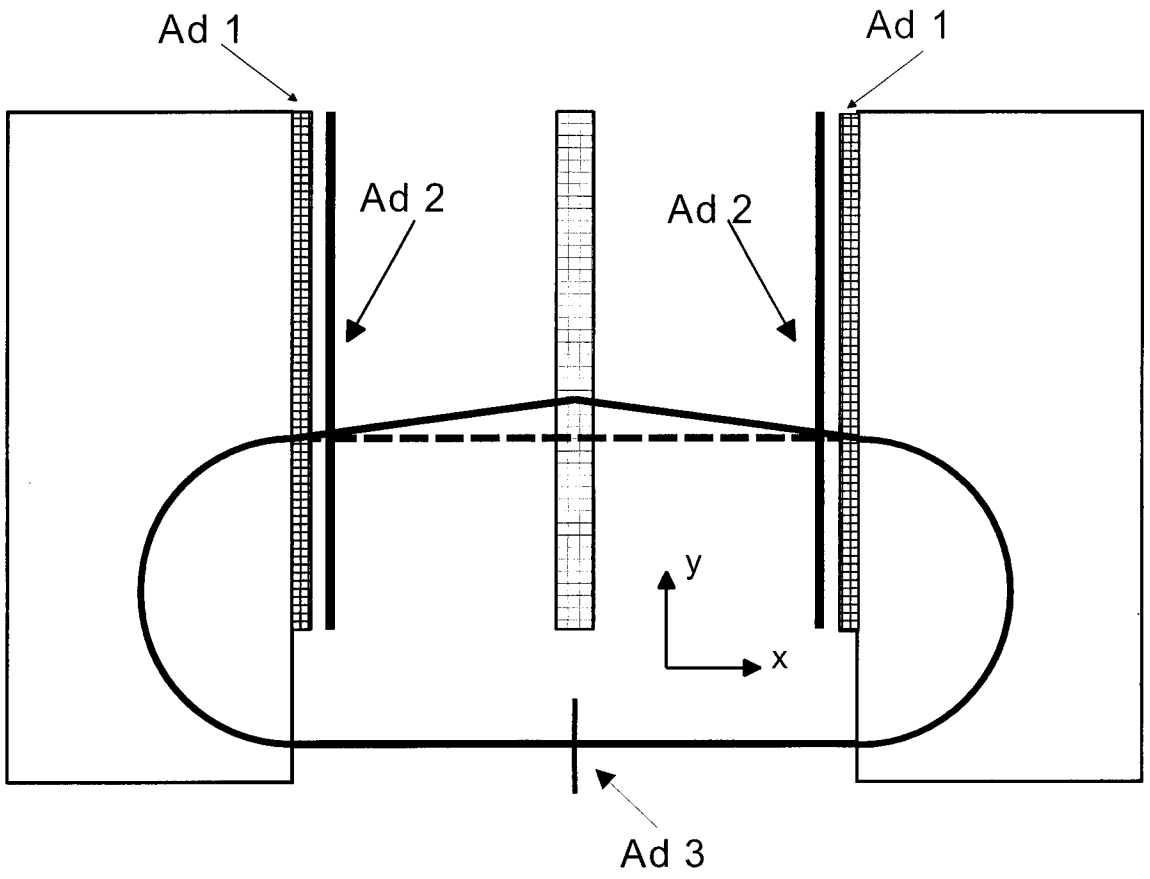

Figure 5.7: Adjustments to the homogeneous magnet model

wavelengths.

To simulate part of these effects, the Homogeneous magnet model has been added with some functions that try and adjust the beam to make it behave like it would in the RTME.

Ad 1: exit angle

First of all, the exit angles, were simulated by placing steering magnet functions at the exit of the magnet. These could be adjusted for every orbit, steering it to fit the right angle. In figure 5.7 the steering magnets are indicated with *Ad1*.

Ad1 is an infinitely thin bending magnet which bends over angle k. This function is similar to the correction magnet as described in the Two-field-sector magnet model (section 4.3). No small angle approximation is made, and therefore the direction vector (x'_i, y'_i), is rotated over the angle k. All other components stay the same and

therefore:

$$\begin{cases} x_f &= x_i \\ y_f &= y_i \\ x'_f &= \cos(k)x'_i - \sin(k)x'_i \\ y'_f &= \sin(k)x'_i + \cos(k)x'_i \\ s_f &= s_i \\ E_f &= E_i \end{cases} . \tag{5.1}$$

yields the components for the final vector.

Ad 2: focussing

Because the strong focussing of the sector edge is absent in the model, thin lenses were added to compensate for this. These were positioned after the steering magnets. These lenses, in the figure indicated with *Ad*2, have the following functional form:

*Ad*2 Is a thin lens, focussing strength P. y_0 is the vertical position of the ideal orbit. First calculate:

$$q = -P(y_i - y_0) + \frac{y'_i}{x'_i} \tag{5.2}$$

Then this gives the following final vector elements:

$$\begin{cases} x_f &= x_i \\ y_f &= y_i \\ x'_f &= \frac{1}{q^2+1} \\ y'_f &= \begin{cases} \frac{q^2}{q^2+1} & q > 0 \\ -\frac{q^2}{q^2+1} & q < 0 \end{cases} \\ s_f &= s_i \\ E_f &= E_i \end{cases} \tag{5.3}$$

In the original model, beam direction deviations have not been taken in account, when calculating the orbit in the magnets. Because these angles are small, only the orbit length has been corrected for this, since this particle property is important for isochronism. Equations 4.9 and 4.18 are corrected with:

$$s_f = s_i + (\pi + 2\arctan(\frac{y'_i}{x'_i}))\rho \tag{5.4}$$

Ad 3: orbit length

The numerical model has small differences in orbit length, from the ideal situation, with perfectly homogeneous magnets. These differences are not equal to those occurring in the Homogeneous magnet model. The main orbit length difference in the latter is the longer orbit length caused by the exit angle adjustment. Since the correction magnets are set to close the orbits, and both magnets are identical, in the drift between the magnets the beam will follow an orbit that is a symmetrical

equilateral triangle around the vertical axis. The length difference with respect to the ideal orbit, parallel to the cavity axis is equal to:

$$dS_h = \frac{L_1 + L_2}{\cos(\phi_e)} - (L_1 + L_2) = (L_1 + L_2)(\frac{1}{cos(\phi_e)} - 1), \tag{5.5}$$

with dS_h the length difference of the Homogeneous magnet model and phi_e the exit angle that the steering magnets have given the beam. If this orbit length difference is compared with the numerical model, the difference between the two can be compensated. This is done just before the cavity, because there the orbit length influences the energy gain in the cavity. The compensation now takes this form:

$$s_x = s_i + (dS_n - dS_h) = s_i + (dS_n - (L_1 + L_2)(\frac{1}{cos(\phi_e)} - 1) \tag{5.6}$$

with dS_n the numerical orbit length difference, and s_x the value for the orbit length s that is taken as input value for the cavity, function 1. In figure 5.7 this is indicated with $Ad3$.

This concludes the model description of the Homogeneous magnet model.

5.6 Homogeneous magnet model with adjustments

M and P are quite different both in shape and width, which can be seen in figure 5.8. Though at high number monitors both M and P show the plateau shape, their comparison with the numerical model is not successful. D and $Dip1$, shown in figure 5.9, are slightly similar, and linear as expected. Very different E plots, shown in figure 5.10, with two edges instead of one, and a very strange behaviour on the plateau. Strong peaks upward.

The individual parameters are not much alike the numerical responses. This difference could be caused by absence of the dependence of the exit angle on the path length and orbit position in the magnet of the beam.

5.7 Two-field-sector magnet model

There are strong similarities between M and P(figure 5.11) and obvious plateau shaped plots, for higher BPM numbers. The individual comparison of the plots gives similarities between M and the numerical plot for low BPM's. P shows less similarity here, though the shape of the plots resembles that of the plots in the numerical model. The plateau's are wider for this model than for the numerical one except for P in the high number monitors.

D and $Dip1$ (figure 5.12) are more similar than in the numerical model, D shows a narrow stability area. A difference in focussing can cause a displacement of the

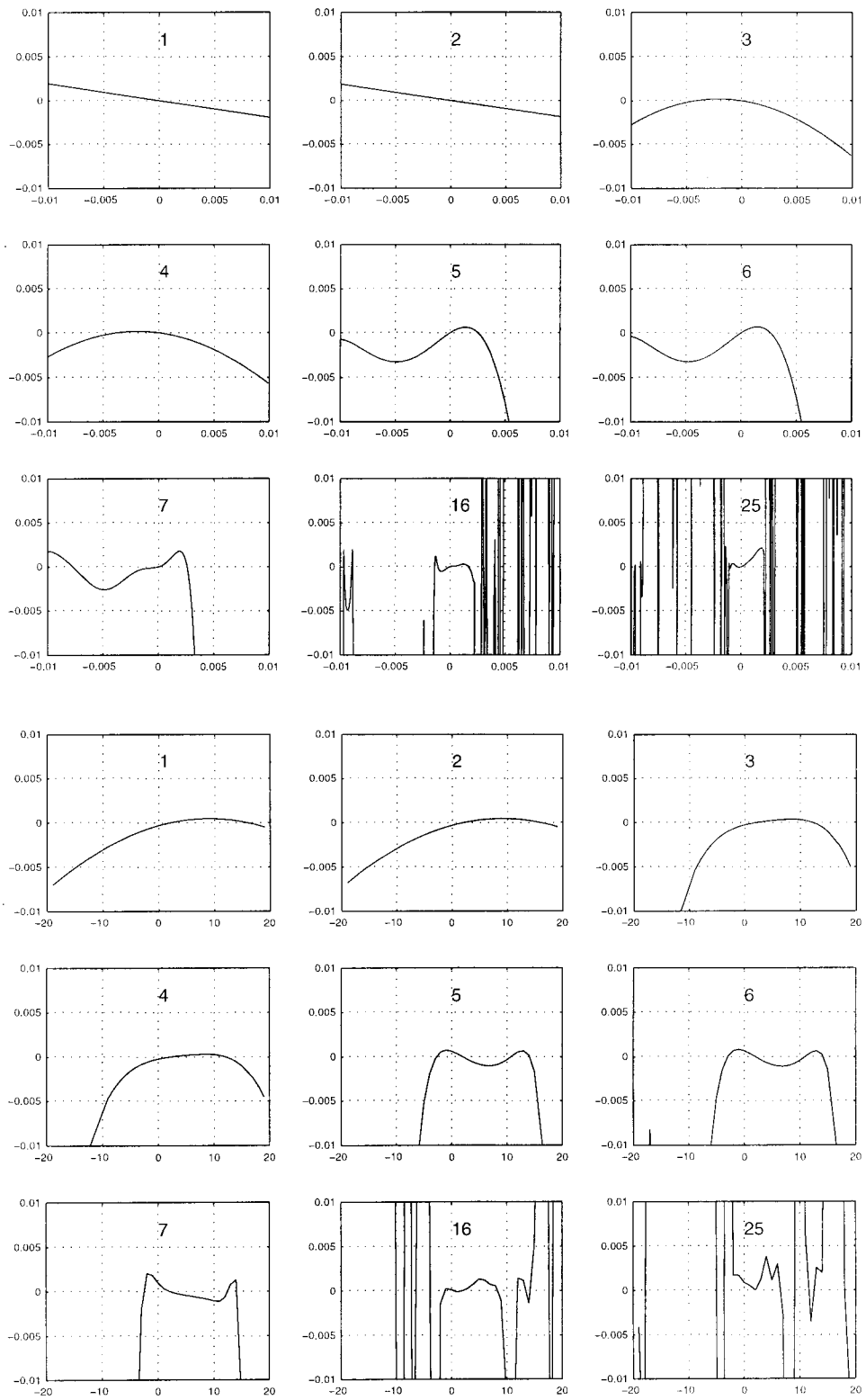

Figure 5.8: Characteristic plots M and P for adjusted homogeneous magnet model

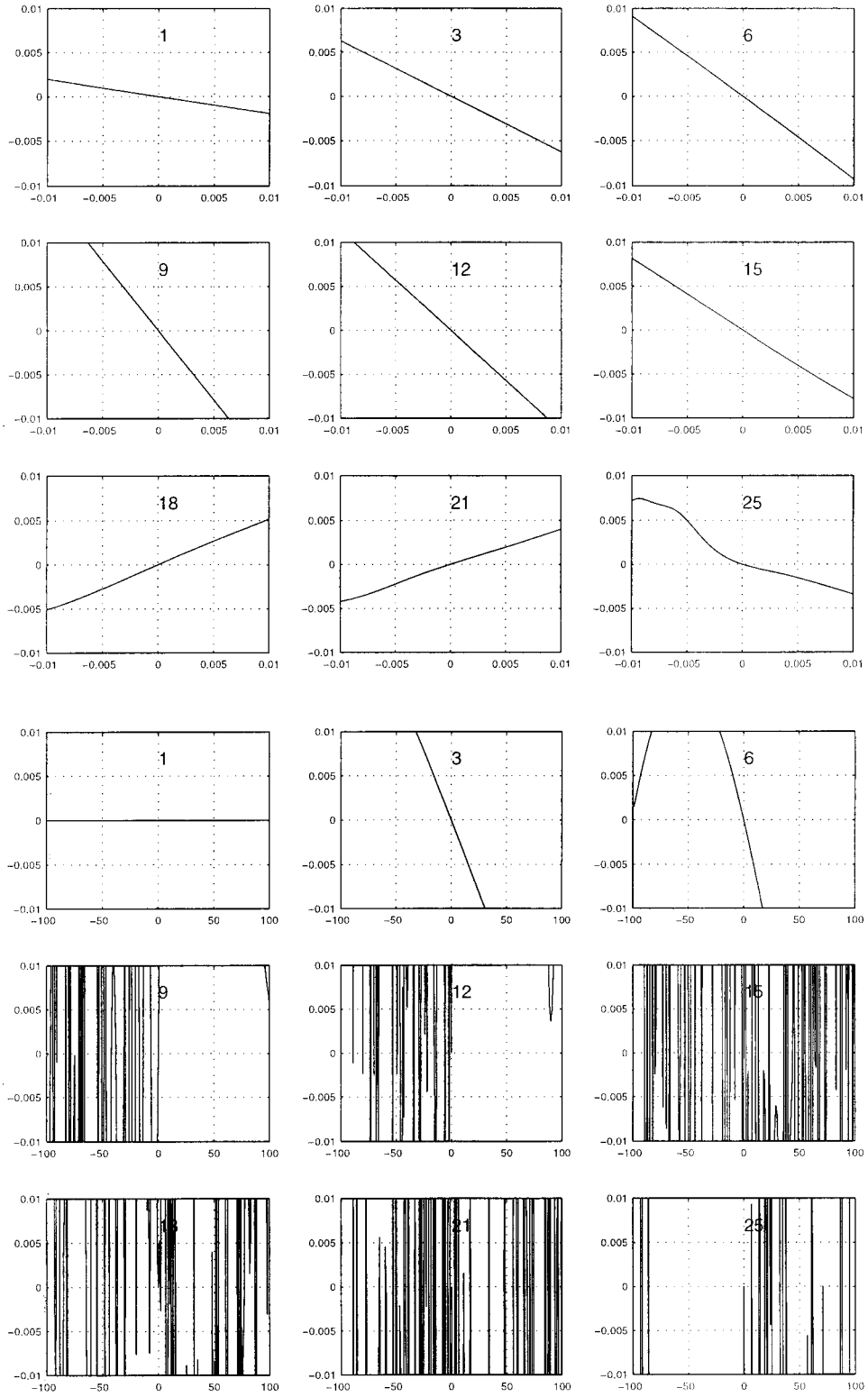

Figure 5.9: Characteristic plots D and $Dip1$ for adjusted homogeneous magnet model

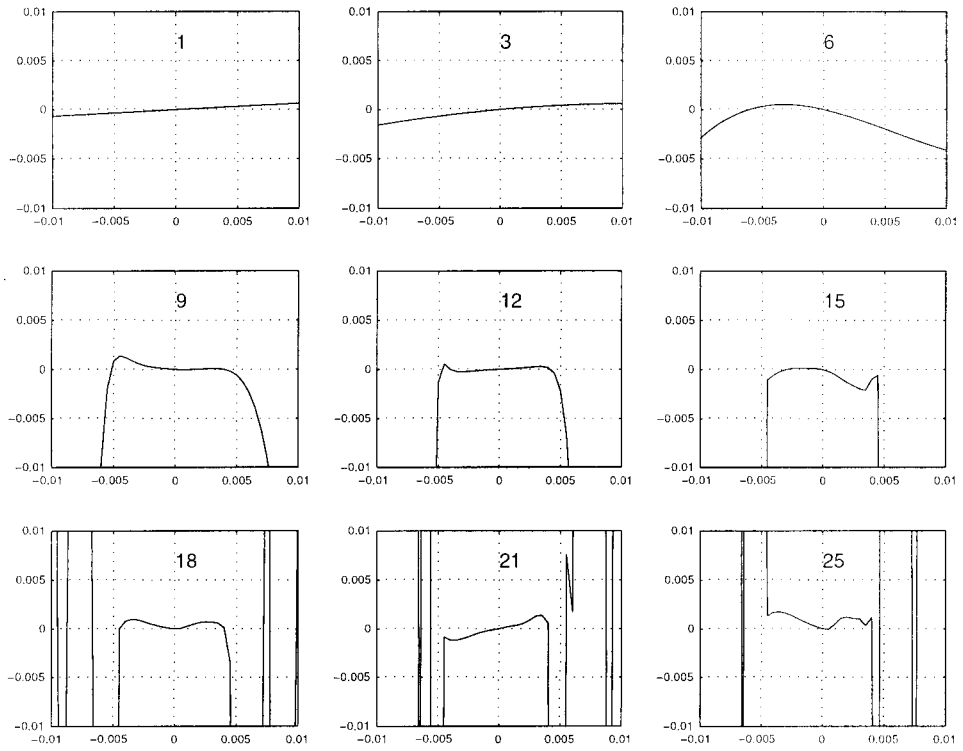

Figure 5.10: Characteristic plots E for adjusted homogeneous magnet model

beam due to D deviations to have a more severe effect. D is also more linear, and therefore alike $Dip1$ because it does not show any directional deviation which are solely caused by inhomogeneities. $Dip1$ seems a lot more alike the numerical model here. E shows a plateau but it seems wider or it is displaced in the direction of the negative deviations when compared to the numerical model.

5.8 Additions to the Two-sector magnet model

As mentioned in subsection 5.5 the use of field-maps in the numerical model results in different exit angles for each orbit, and an orbit length difference with respect to the ideal orbit.

Ad 1: exit angle

To be able to simulate the exit angles in the magnets, that are caused by magnet inhomogeneities, an adjustment was made to the constant field factor a. For every orbit a factor was found that, for the exact ideal settings, gave a deviating angle that was equal to that of the numerical model. These factors were then plotted against the vertical positions and a parabolic function was fitted through them. The factor

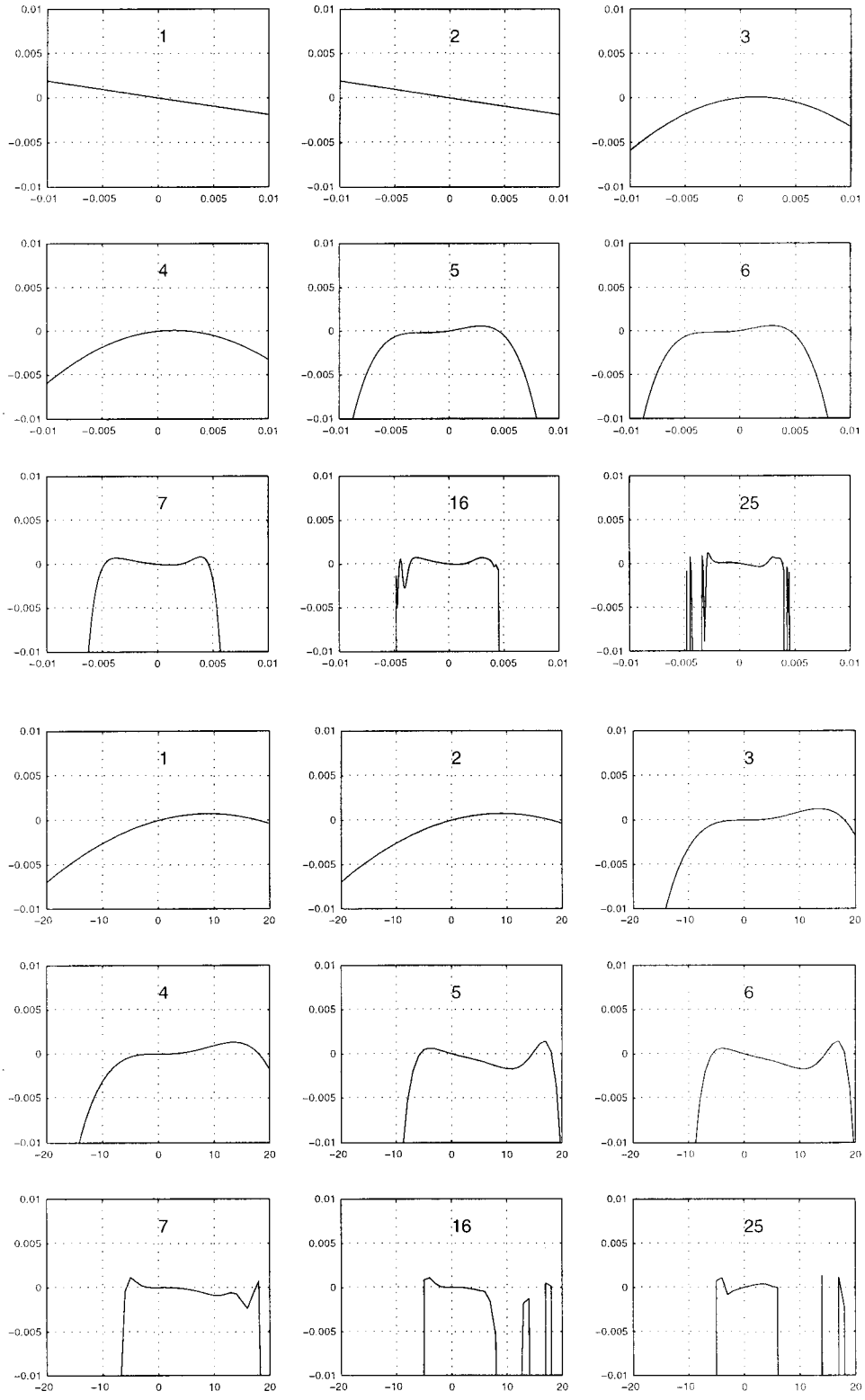

Figure 5.11: Characteristic plots M and P for two-field-sector magnet model

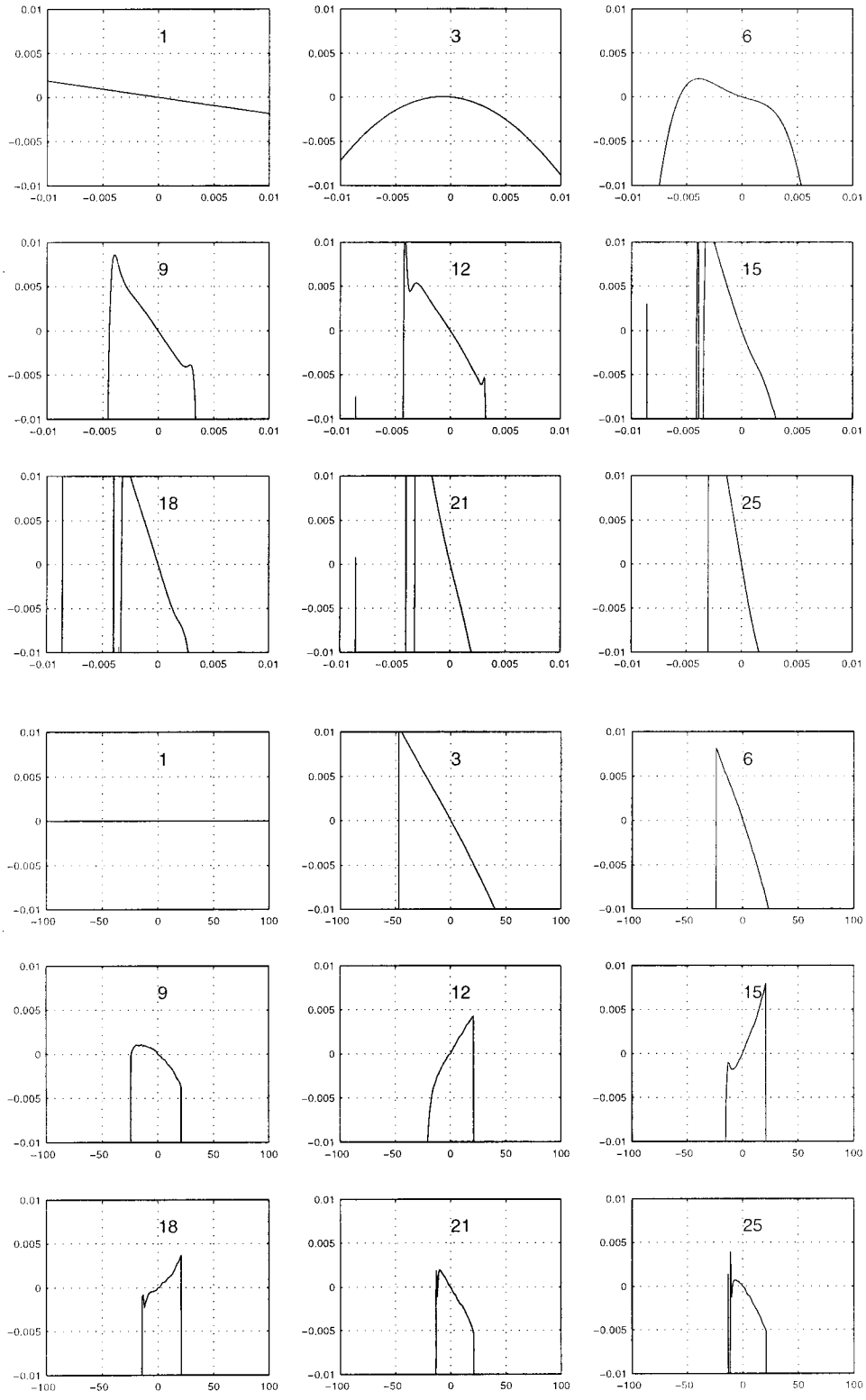

Figure 5.12: Characteristic plots D and $Dip1$ for two-field-sector magnet model

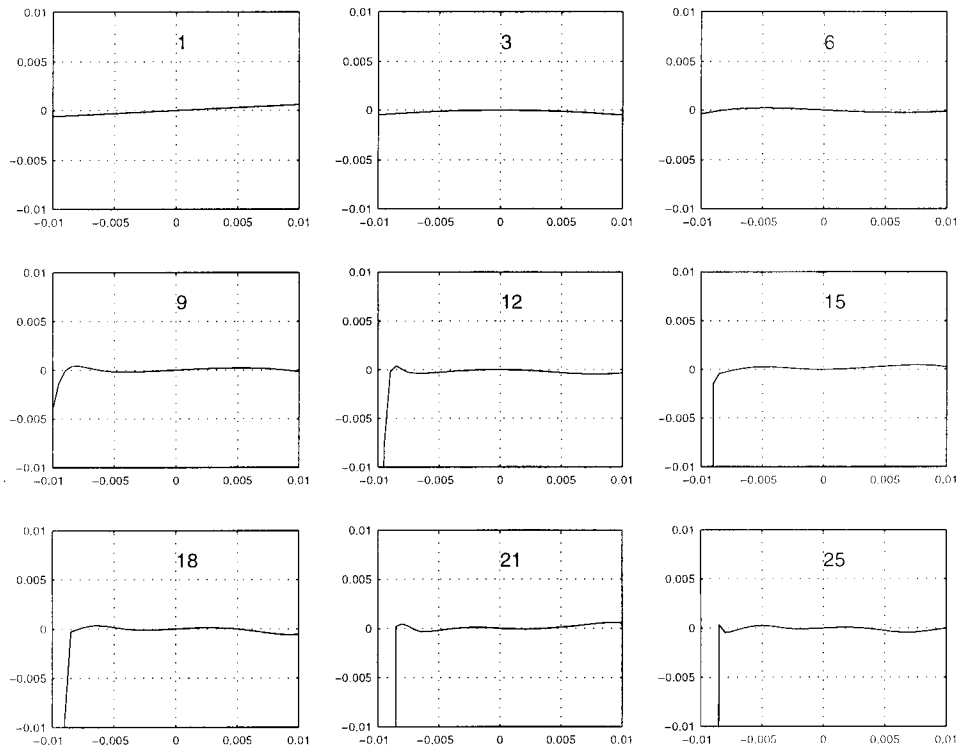

Figure 5.13: Characteristic plots E for two-field-sector magnet model

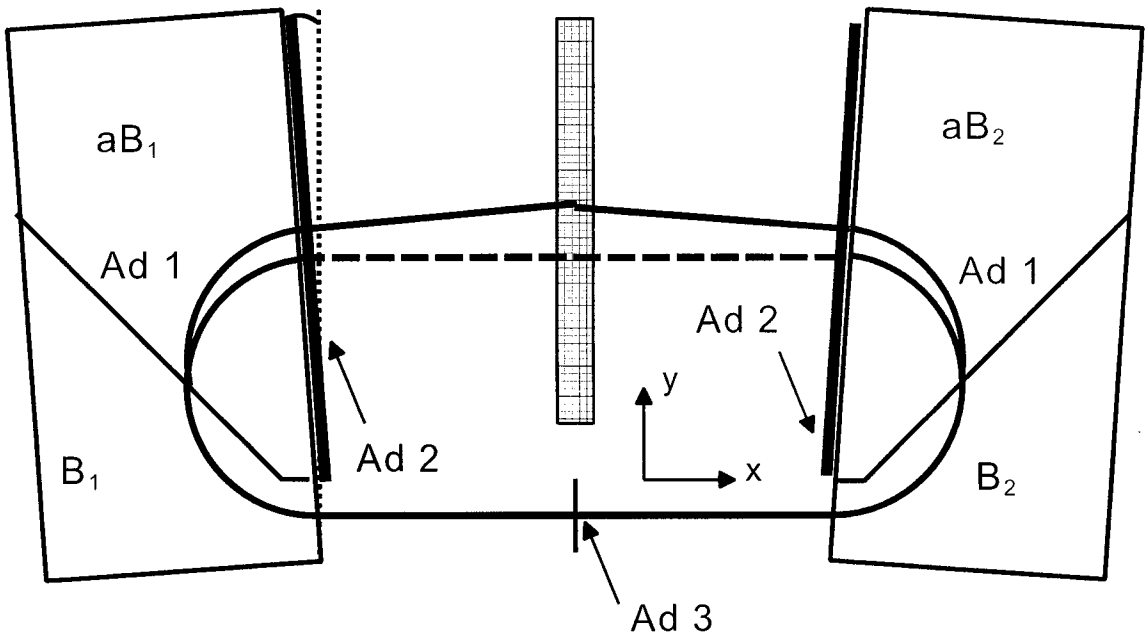

Figure 5.14: Additions to the two-sector magnet model

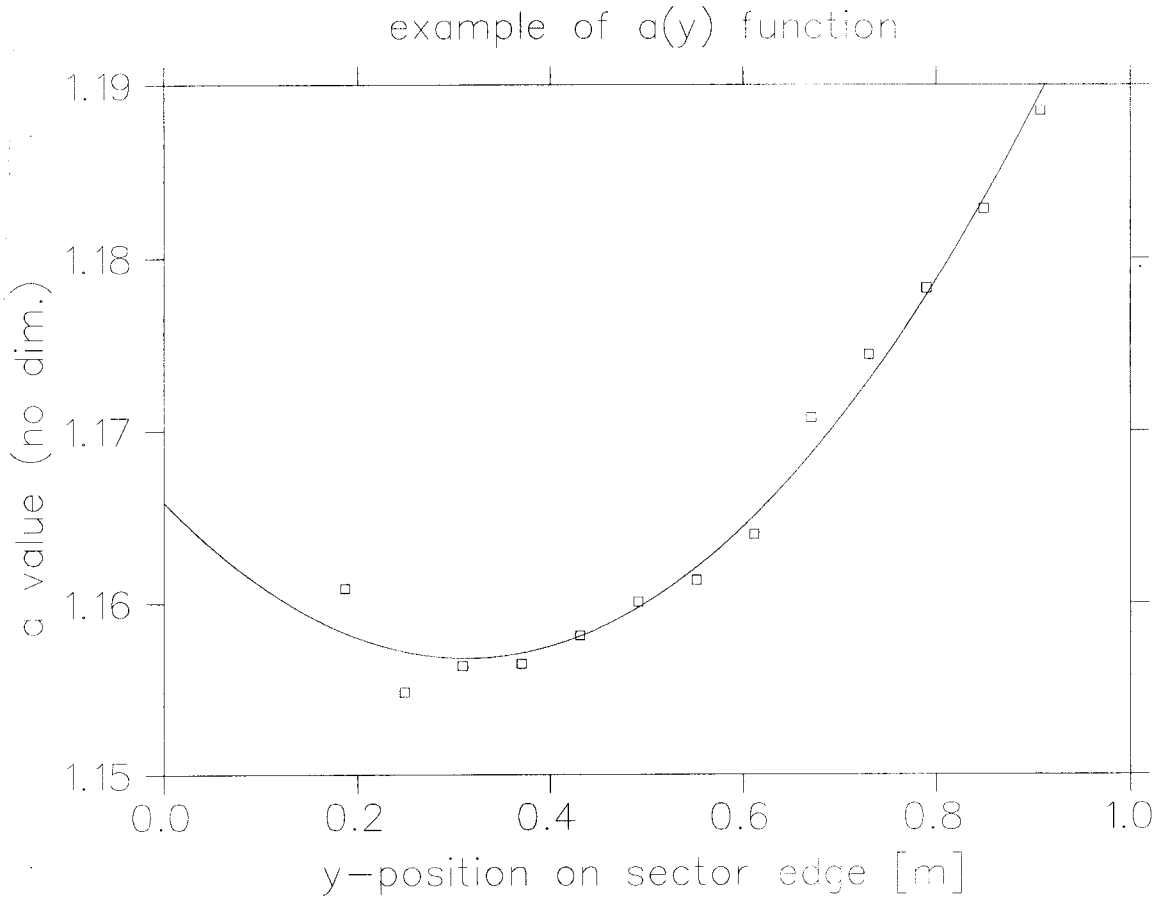

Figure 5.15: Example of fitted a-function

a now takes the form:

$$a = c_1 x^2 + c_2 x + c_3 \tag{5.7}$$

with typical values of c_1 are around 0.09, of c_2 between -0.06 and -0.05 and for c_3 around 1.165. This function was then implemented at the start of function C_2 and the resulting value was also taken in function I_1. This addition is indicated in figure 5.14 as *Ad*1 An example of a fitted a-function is shown in figure 5.15

Ad 2: focussing

The second addition, indicated by *Ad*2, is thin lens, identical to the one in the Homogeneous magnet model. This was added to compensate the difference in focussing between numerical model and the Two-sector magnet model. Though both have a sector edge the field maps do not have the sharp edges in the field like the model has. This changes the amount of focussing at the edge which is compensated by the lens. The function of the lens is briefly recapitulated.

*Ad*2 is thin lens, focussing strength P. y_0 is the vertical position of the ideal

orbit. First calculate:

$$q = -P(y_i - y_0) + \frac{y'_i}{x'_i} \tag{5.8}$$

Then this gives the following final vector elements:

$$\begin{cases} x_f &= x_i \\ y_f &= y_i \\ x'_f &= \frac{1}{q^2+1} \\ y'_f &= \begin{cases} \frac{q^2}{q^2+1} & q > 0 \\ -\frac{q^2}{q^2+1} & q < 0 \end{cases} \\ s_f &= s_i \\ E_f &= E_i \end{cases} \tag{5.9}$$

Ad 3: orbit length

*Ad*3, the orbit length correction, is again identical to the one used in the Homogeneous magnet model, and therefore the adjusted orbit length for the cavity function becomes:

$$s_f = s_i + (\pi + 2\arctan(\frac{y'_i}{x'_i}))\rho \tag{5.10}$$

This is in fact an approximation, because, unlike the Homogeneous magnet model, the magnets in the Two-sector magnet model have been tilted. This affects the drift distance slightly, depending on the vertical position. Since this distance is not taken in account, the correction has an inaccuracy.

5.9 Two-sector magnet model with adjustments

Good similarity between M and P(figure 5.16), though a slight displacement of one of them can be noted. M shows a behaviour quite similar to that of the numeric model. Though the exact shape of the plots is not the same, the stability region is roughly the same. P also has a slightly larger stability area compared with the numerical model. Especially the strange behaviour shown in some high number monitors especially the 'inverted' plateau's at monitors 16 to 21 is doubtful.

D and $Dip1$ shown in figure 5.17, alike the original two-field-sector model, a much higher sensitivity for displacement. Both show behaviour not unlike M or P, with plateau shaped plots.

Both D and $Dip1$ show behaviour that is highly unlikely or inconsistent with what we see in the numerical model.

D shows a rather narrow stability area. This could be the result of some artefacts in the calculation, or a lack of focussing which causes the beam to be lost due to the position or direction deviation.

$Dip1$ is very strange in behaviour, and seems to be in contradiction with expectations. This could also be an artefact of the calculations. E Shows an edge on the

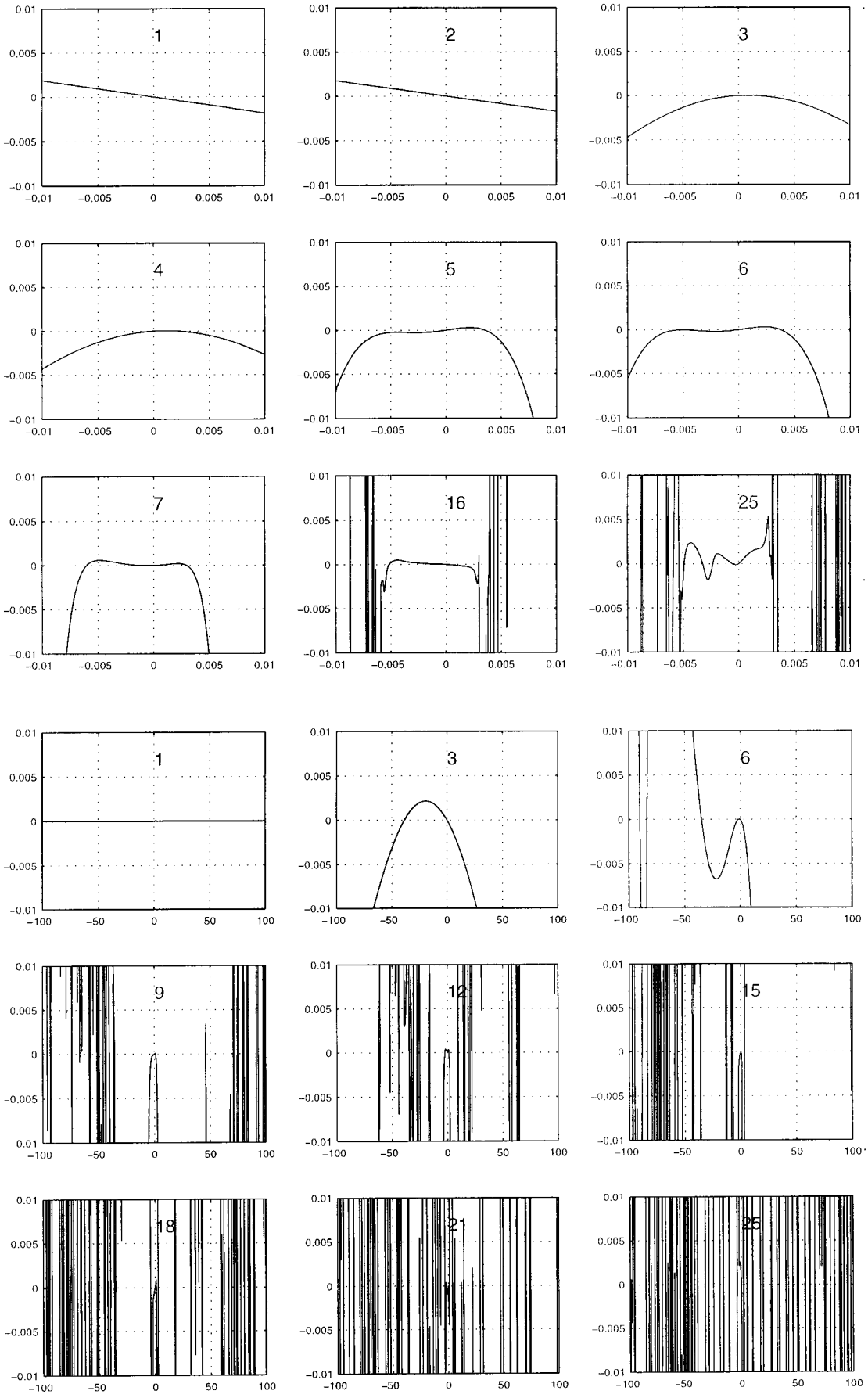
1
2
3
4
5
6
7
16
25
1
3
6
9
12
15
18
21
25

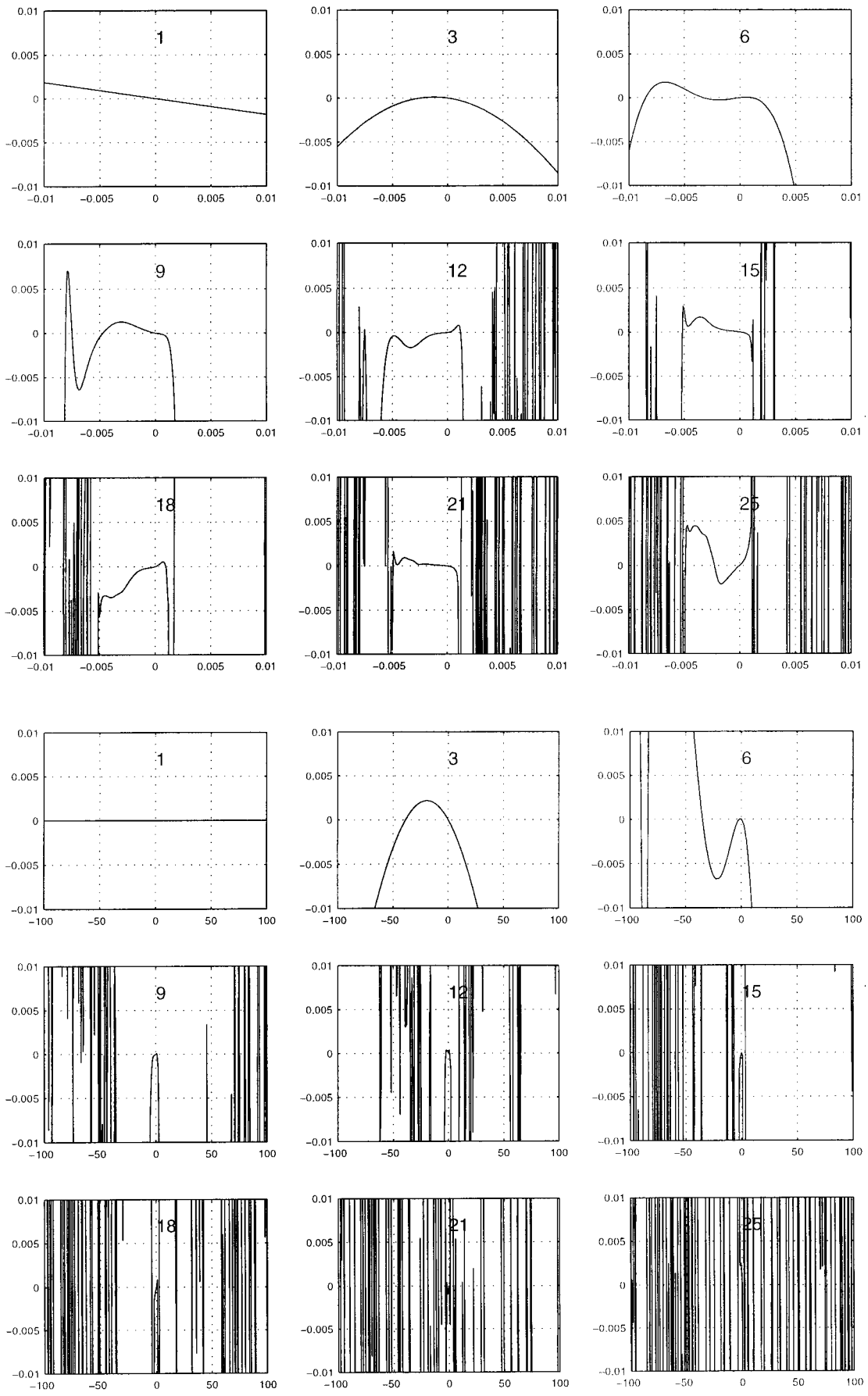
1
3
6
9
12
15
18
21
25
1
3
6
9
12
15
18
21
25

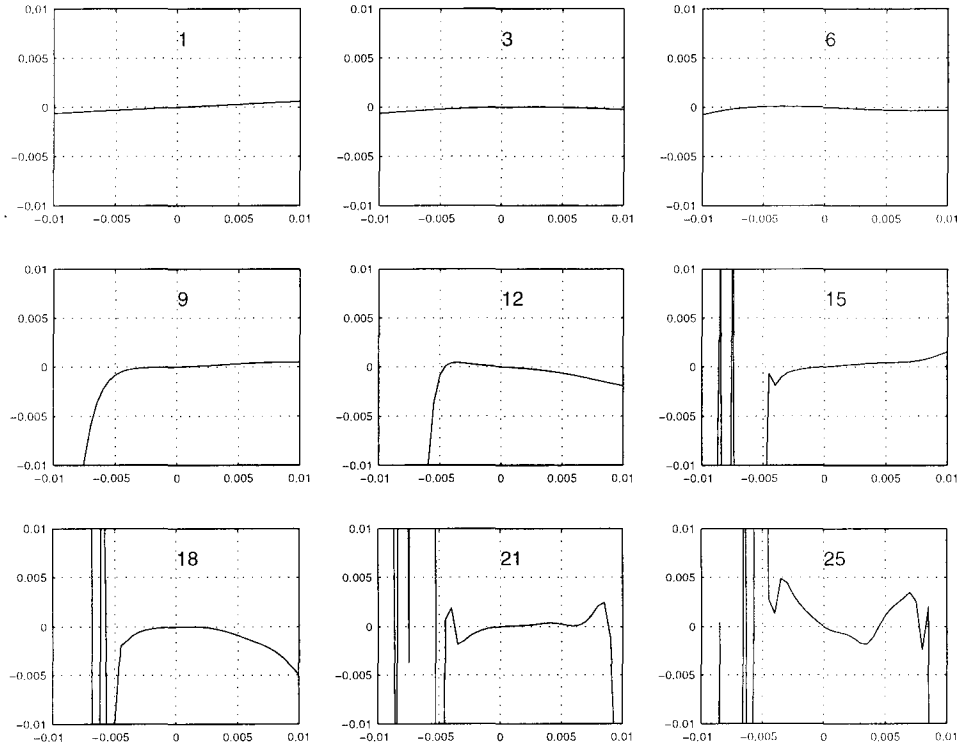

Figure 5.18: Characteristic plots E for adjusted two-field-sector magnet model

negative deviation side, but also shows strange peaks at that edge which were not there for any of the models.

5.10 Applicability of the models

Though there are similarities between the Homogeneous magnet model and the numerical model, the general picture is that the influence of inhomogeneities and the strong focussing of the sector edge, give significantly different behaviour. The additions to this model do not improve the similarities with the numerical model. This might be caused by the fixed exit angle per orbit, which is variable, depending on the orbit through the magnet in the numerical model.

The Two-sector magnet model shows a better match, but here the D variations are clearly not the same as in the numerical model. This is a fundamental difference due to the inhomogeneities, because they cause directional differences. As the inhomogeneities are not present in the simplified models as the hard-edge approximation eliminates that. After additions, the D variation still is not similar to the numerical plot. Also $Dip1$, has a strange behaviour in this model. The narrow peaks seem

to be contradictory to the behaviour seen in the numerical model and this is rather surprising in the light of the similar geometrical layout of the model.

Altogether, it is doubtful if either of these models can accurately predict the behaviour of the RTME when they would be applied in a feedback strategy. Some peculiar behaviour in the adjusted Two-sector model may be attributed to the adjustments themselves. These adjustments are mainly an attempt to simulate the inhomogeneities and focussing of the numerical model, and there may be other ways to incorporate these into a model of this structure.

The mixing of position and direction deviation in the numerical model, when M or D are varied, may also be a source of the dissimilarities between the simplified and numerical models. This mixing is a direct result of the inhomogeneities and even the representation implemented in the adjusted two-field-sector model was not sufficient to simulate the behaviour accurately. The influence of the inhomogeneities is present throughout the whole magnet, while the used representations either are implemented at the exiting edge, or at the sector edge. A representation that influences the shape of the orbit in both sectors might give a better result as it would be closer to the influence of inhomogeneities in the actual bending magnet. If this type of inhomogeneity representation is used, it is also possible that the focussing is more equal. The use of additional lenses is not preferable, because this has the same problems as for the exit angle representation using correction magnets: the lens can only be used for every orbit separately. This is dissimilar to the existing situation where the entire orbit focuses a set of particles, displaced vertically at the cavity axis. Though the lenses could do the same for each orbit, the existence of the direction deviation is not take in account while calculating the necessary lens strength and this may be a cause for dissimilarities between simplified and numerical model. As both models have lenses added, and exit angle corrections that are implemented before them, this effect is present in both models.

5.11 Suggested tuning algorithm

From the results of the parameter variations with the numerical model shown in appendix ??, a brute-force tuning algorithm can be derived for the parameters M, D, E and P. The method is based on a four dimensional scan of a grid that has been chosen on the basis that the plots in the above mentioned appendix, show variations of a magnitude typical for the errors that are expected to occur in the parameter settings. The parameters will be varied in steps, equally distributed over the intervals: -1% to 1% for M, D and E, and -10° to 10° for P. The interval for P is half of that shown but it is chosen rather arbitrarily. It has been decided on basis of the stability intervals on the plots that M will be varied over 5 steps, D over 3, E over 5 and P over 5. The step sizes reflect the relative size of the area where the position deviation is relatively small. Because D has no visible stability area here only 3 steps will be taken, to see if this parameter is also close to the appropriate

value. This gives $5 \times 3 \times 5 \times 5 = 375$ grid points. For every grid point in the four dimensional space of $M - D - P - E$, the dipoles are optimised, trying to guide the beam through the microtron using a linear feed-back mechanism. This mechanism uses the responses of the correction dipoles on odd numbered BPM's as calculated numerically and used in a matrix manipulation which yields the adjustments directly from the position measurements [11]. It is important to note that for every grid point these responses are different. For every grid point the amount of iterations of the dipole correction mechanism has been limited to 100. The mean total number of iterations for the entire grid scan appeared to be (2930 ± 40). The total percentage of the injected beam current that was extracted finally appeared to be $(73 \pm 3)\%$. Assuming that 3 seconds are needed between iteration steps an estimate of 2.5 hours for the entire procedure is estimated. This is acceptable. Further optimisation of the dipole correction, and the choice of a more convenient starting point from previous runs might shorten this time.

5.12 Concluding remarks

Though the models are direct 'translations' of an ideal racetrack microtron, they did not describe the behaviour of the microtron accurately. Adjustments were not sufficient to improve the behaviour satisfactory. Representation of the inhomogeneities in a simplified manner was not successful but could still prove possible since many methods have not been tested yet.

6 Conclusion

The purpose of the study presented in this report was the development of an automated tuning mechanism for the Racetrack Microtron Eindhoven (RTME). This mechanism should be able to adjust the adjustable parameters of the RTME to compensate alignment and machining errors and errors in the setting of the parameters to make successful acceleration of an electron beam, from 10 to 75 MeV possible.

The beam behaviour in the RTME has been examined by calculating the effect of parameter deviations using an existing numerical model called BANBA. A feedback strategy was chosen for the tuning, with the intent to develop a mechanism that would calculate the corrected settings or the adjustments needed for a correct beam position. The initially suggested linear matrix calculation, which would yield the settings directly, was rejected on basis of the beam behaviour calculations, because they showed a non-linear behaviour for nearly all parameters. A non-linear model based feedback strategy was further developed because that gave the opportunity to use the knowledge about the RTME's design into the tuning.

The models developed for this strategy, were simplified, because the existing numerical model had a calculation time in the range of hours, which would be too long for the tuning to be useful. To stay as close to the physical reality of the machine, the simplification was done in the method of calculation of the motion of the particle. While the numerical model used a numerical integration, the simplified models used a geometrical electron-optics method, which uses matrices for basic elements like bends and drifts. This method has been chosen to minimise the calculation time, but maintain the level of accurate description. As this method can be used in an analytical way, the model, also analytical, was possibly invertable.

The simplified models that were developed were found to be too complex to use as analytical models. They could not be inverted either. The beam behaviour shown by the models, showed some similarities, but was found to be too inaccurate to use in the feedback strategy. This dissimilar behaviour might arise from the simplified dynamics calculation, but is most probably the result of the absence of fieldmaps in these models. The magnet inhomogeneities cause a change in behaviour that is very hard to transform into a simplified representation. Especially the interlinking of both position and directional deviation by changing the mean field and field differences might well be a source of the differences. Attempts to implement this behaviour into a simplified model have proven unsuccessful.

The brute-force method presented finally, is expected to make successfull extraction possible in an acceptable time frame of approximately 2.5 hours.

References

References

[1] Theuws W.H.C., Botman J.I.M., Hagedoorn H.L. *Continuous Electron-energy Variation of the Eindhoven Racetrack Microtron*, Proc. Part. Acc. Conf. Vancouver (1997) 1036-1038

[2] Webers G.A. *Design of an electron-optical system for a 75 MeV racetrack microtron: Implications on pole shape design* Ph.D thesis, Eindhoven University of Technology, 25 May 1994.

[3] Rosenzweig J., Serafini L. *Transverse Particle Motion in Radio-frequency linear accelerators*, Phys. Rev. E vol.49, no.2 (1994) 1599-1602.

[4] Gerlowski M.M. *Correction scheme studies for the Racetrack Microtron Eindhoven and Longitudinal Motion in a Racetrack Microtron*, Report on technical training period, March - June 1996.

[5] Leeuw R.W. de, The Accelerator Injection Chain of the Electron Storage Ring EUTERPE, Ph.D Thesis, Einhoven University of Technology (1996).

[6] Pruiksma J.P., *Electromagnetic fields in a periodically disk loaded circular waveguide*, M.Sc. Thesis, Eindhoven University of Technology. 1996.

[7] Leeuw R.W. de, Wijs M.C.J. de, Webers G.A., Hagedoorn H.L.,Botman J.I.M., Timmermans C.J., *Matching the emittance of a linac to the acceptance of a racetrack microtron*, Proc. Part. Acc. Conf. Dallas (1995) 1882-1884.

[8] Gossens L.W.A.M. *Measurements and simulations of the beamline between LINAC10 and RTME*, M.Sc thesis, Eindhoven University of Technology ,0ctober 1995 - October 1996.

[9] Theuws W.H.C., *Personal Communications* (1998).

[10] Theuws W.H.C., *Beam Position Monitoring and Beam Positioning in the Racetrack Microtron Eindhoven*, M.Sc thesis, Eindhoven University of Technology, VDF/NK 94-36, October 1993 - October 1994.

[11] Theuws W.H.C., Ph.D thesis Eindhoven University of Technology.

[12] de Wit F.F., *Compilation of Response Plots from the RTME Tuning Parameters* Internal Report VDF/NK 99-06, February 1999.

Appendix A

List of Symbols

parameter	meaning [units]	first occurence
a	relative strength of high field against low field	1.4.1
β_n	particle velocity in units of c for orbit n (n = 1,2,3,..,12)	1.4
B_1	magnetic (low-)field left magnet [T]	4.2
B_2	magnetic (low-)field rigth magnet [T]	4.2
B_c, n	correction dipole field n (n = 1,2,3,..,12)[Gauss]	1.5
B_H	high field [T]	1.4.1
B_L	low field [T]	1.4.1
B_{left}	left magnetic (low-)field strength [T]	1.5
B_r	resonant magnetic field [T]	1.4
B_{right}	right magnetic field strength [T]	1.5
c	speed of light [m/s]	1.4
D	field difference variation	2.2
D_1	distance of beam profile monitors to vertical axis [m]	4.2
D_2	distance of beam profile monitors to vertical axis [m]	4.2
$Dip1..12$	correction dipole variation [Gauss]	2.2
e	elementairy charge [C]	1.4
E	microwave amplitude variation	2.2
E_0	rest energy of electron [J]	1.4
E_c	amplitude of acceleration wave in cavity [MeV]	4.2
E_{cav}	energy gain in cavity [J]	1.4
E_f	final particle energy [MeV]	4.2
E_i	initial particle energy [MeV]	4.2
E_{inj}	kinetic energy at injection [J]	1.4
E_r	energy gain in cavity [J]	1.4
δE	calculated energy gain in simplified models [MeV]	4.2

$\frac{1}{f}$	focussing factor cavity in simplified models[m^{-1}]	4.2
f	accelerating microwave frequency for linac and RTME [MHz]	1.4
γ	relativistic factor	4.2
γ_i	relativistic factor orbit i (i = 1,2,..12)	4.2
k	bending angle of correction magnet [°]	4.2
λ	wavelength accelerating microwave [m]	1.4
L	drift length between the magnets [m]	1.4
L_1	distance from cavity to left magnet [m]	4.2
L_2	distance from cavity to right magnet [m]	4.2
μ	initial mode number	1.4
M	mean magnetic (low-)field variation	2.2
M_1, M_2, M_3, M_4	bending magnets beam transport system	1.3
ν	incremental mode number	1.4
N	number of orbits	1.4
ϕ_{exit}	exit angle from bending magnet [°]	1.4.3
ϕ_f	final angle of parametric orbit representation	4.3
ϕ_i	initial angle of parametric orbit representation	4.3
p	horizontal position of centre-point of a circular orbit	4.3
P	injection phase variation [°]	2.2
$Q_1, Q_2, Q_3, Q_4, Q_5, Q_6$	quadrupole magnets beam transport system	1.3
ρ	orbit radius in magnetic field [m]	4.2
s	distance travelled [m]	4.1
S	effective drift distance [m]	4.3
s_i	initial distance travelled [m]	sec:model1
s_f	final distance travelled [m]	4.2
τ	tilt angle [°]	1.4.1
τ_1	tilt angle left magnet two-field-sector magnet model	4.3
τ_L	tilt angle left magnet homogeneous magnet model	4.2
τ_R	tilt angle right magent homogeneous magnet model	4.2
θ	angle between sector edge and cavity axis [°]	1.4.1
θ_1	angle between sector edge and magnet edge [°]	4.3
θ_2	angle between sector edge and magnet edge [°]	4.3
x_f	final horizontal position [m]	4.2
x_i	initial horizontal position [m]	4.2
y_f	final vertical position [m]	4.2
y_i	initial vertical position [m]	4.2
x'_f	final horizontal direction component	4.2
x'_i	initial horizontal direction component	4.2
x_{in}	incomming particle propperty vector	4.1
x_{out}	outgoing particle propperty vector	4.1
y'_f	final vertical direction component	4.2
y'_i	initial vertical direction component	4.2

Appendix B
Sample of Response Plot

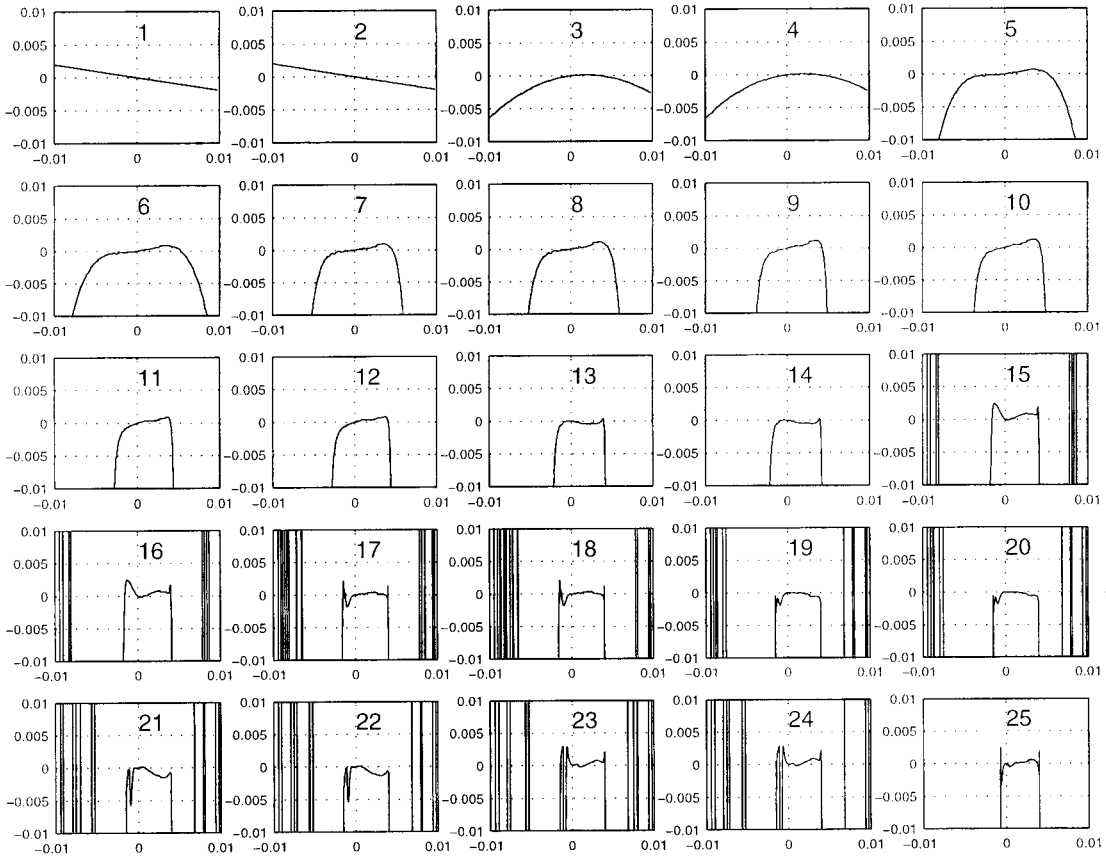

Figure B.1: Numerical model: M deviation

All response plots can be found in internal report VDF/NK 99-06 [12] which appears as a separate appendix with this M.Sc Thesis.

Eindhoven University of Technology
Department of Applied Physics
Physics and Applications of Accelerators

Complilation of Response Plots for the RTME Tuning Parameters

F.F. de Wit
VDF/NK 99-06

Appendix to M.Sc Thesis February 1998 - February 1999

Supervision and guidance: Ir. W.H.C. Theuws
dr. J.I.M. Botman
Ir. S.R. Weijers
dr.Ir. M. Weiss

Introductory remarks

This separate appendix accompanies internal report VDF/NK 99-05. It contains an overview of all response plots from the 16 tuning parameters of the RTME. The scaling of these plots is explained in the next section, after which section 1 shows the response plots of the numerical model BANBA. The subsequent sections 2, 3, 4, and 5 give the same tuning parameter variations for the two simplified models and the adjusted versions of those.

Scaling of the plots

Every graph contains a matrix of 5×25 plots that give the response on the BPM whose number is given on top of each plot. Numbering of the monitors is by the order the beam passes them. For parameters M, D and E the scaling on the parameter axis is indicated in fractions of the ideal setting. Therefore a '0.01' label means a 1% deviation from the ideal setting. For parameter P, the scale indicates the phase at injection in degrees, and for the dipole variations ($Dip1$ to $Dip12$), the parameter axis gives the field strength in Gauss. For all plots the vertical axis shows the position relative to the ideal orbit, and limited to deviations of 0.01m.

1 Response plots of the numerical model

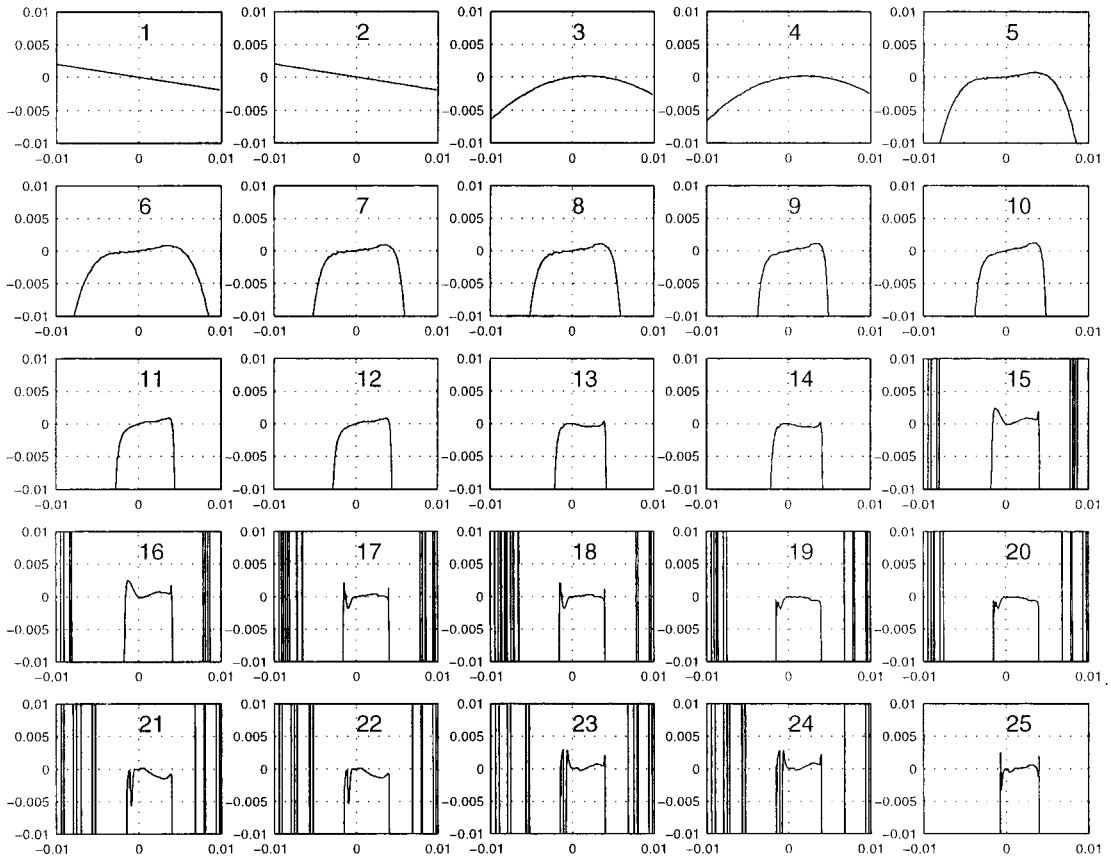

Figure 1.1: Numerical model: M deviation

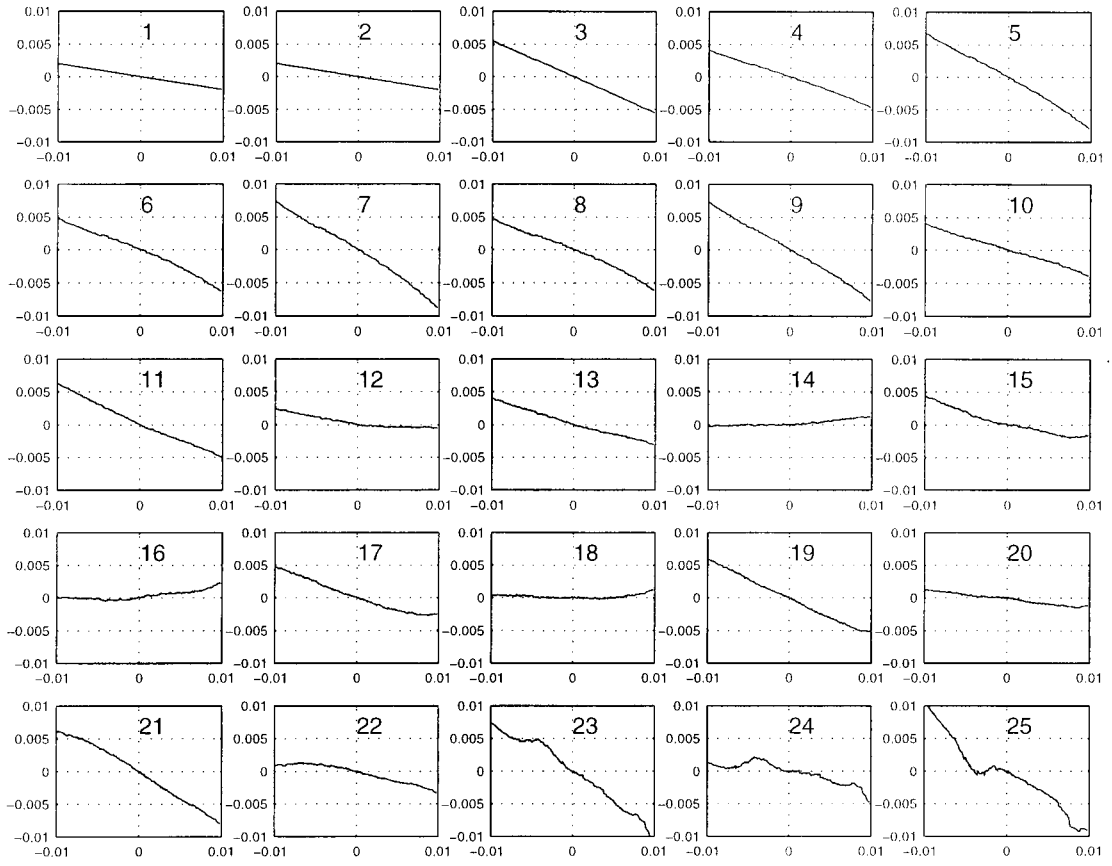

Figure 1.2: Numerical model: D deviation

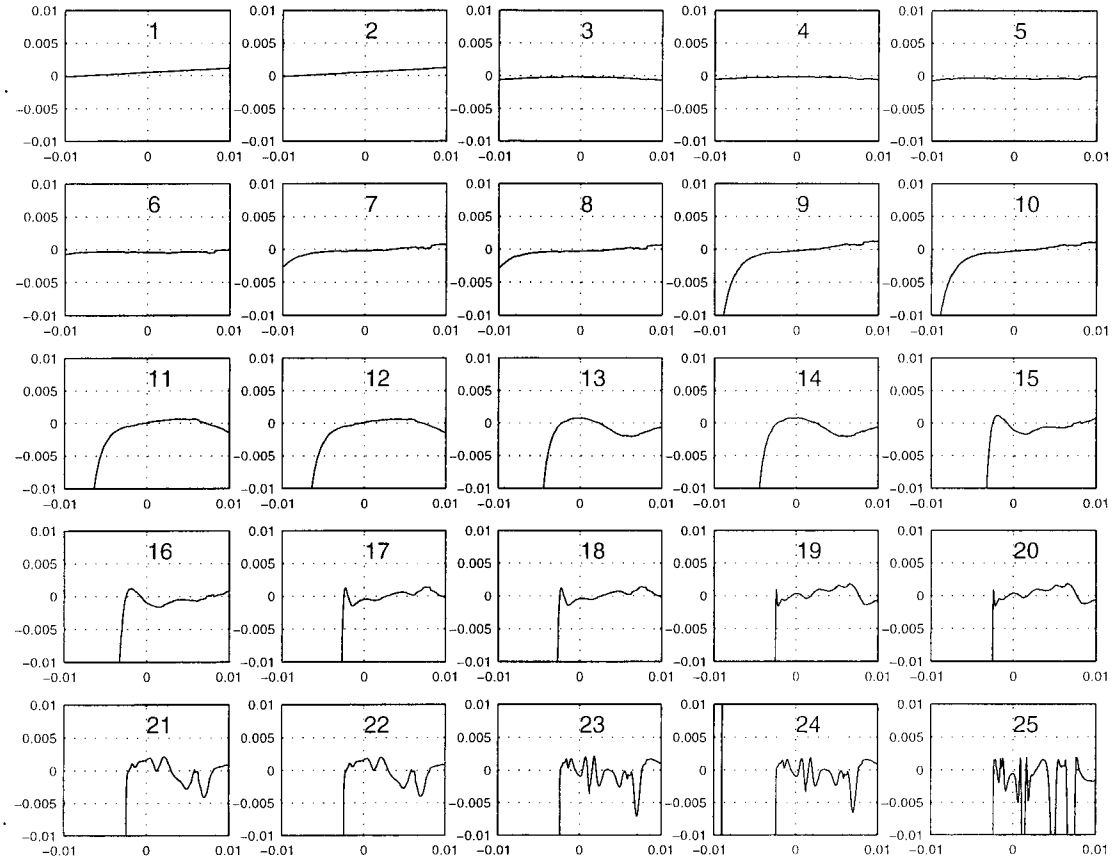

Figure 1.3: Numerical model: E deviation

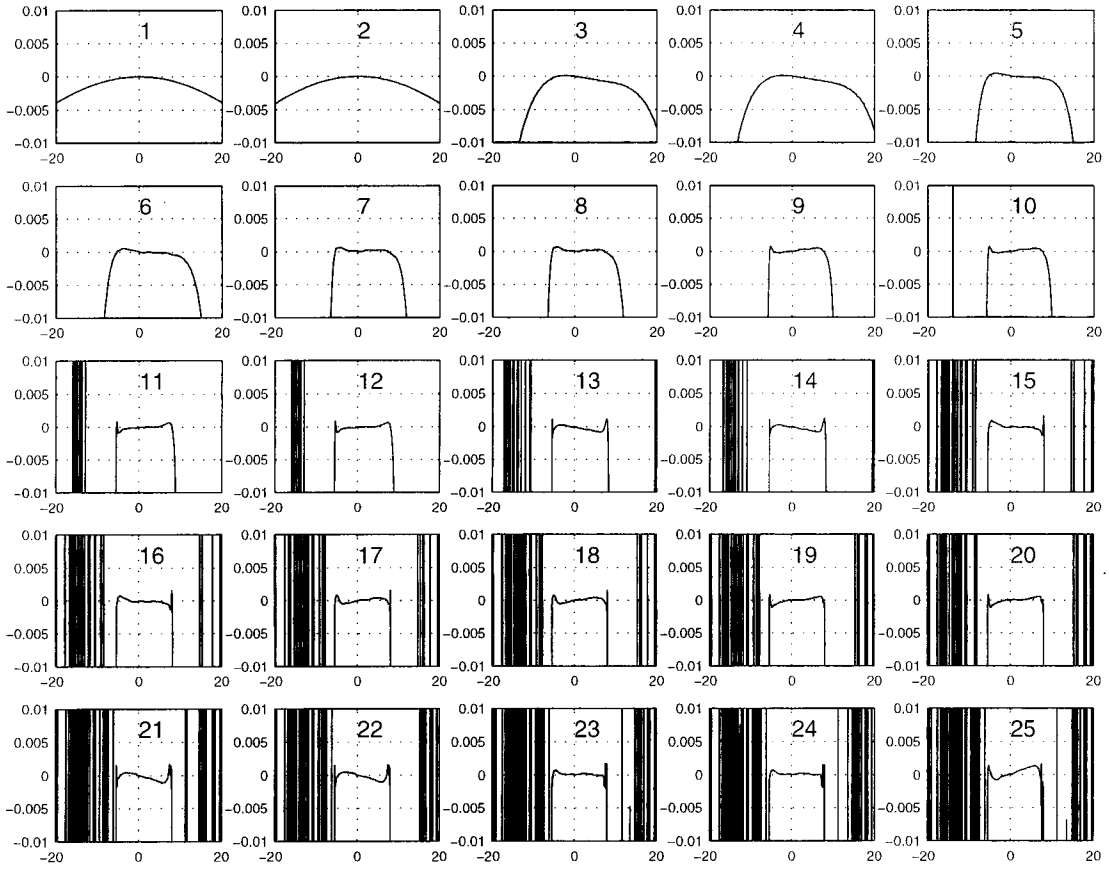

Figure 1.4: Numerical model: P deviation

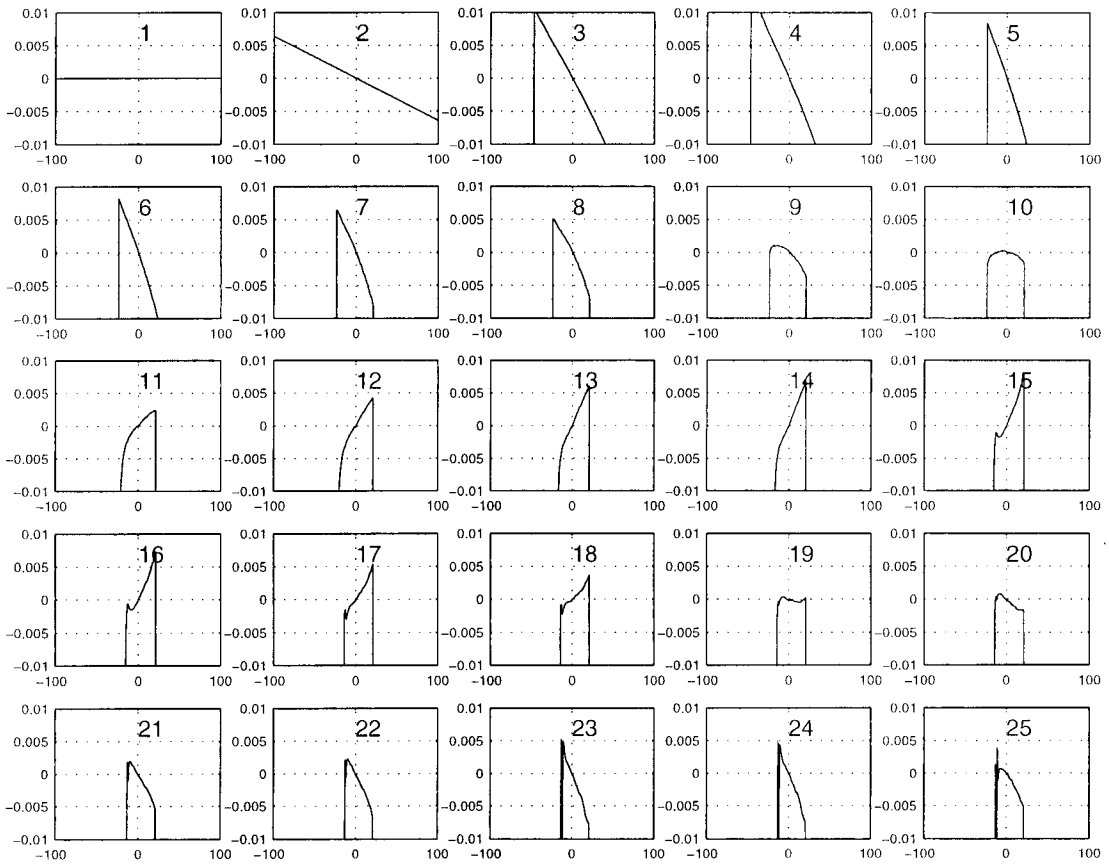

Figure 1.5: Numerical model: Dip1 deviation

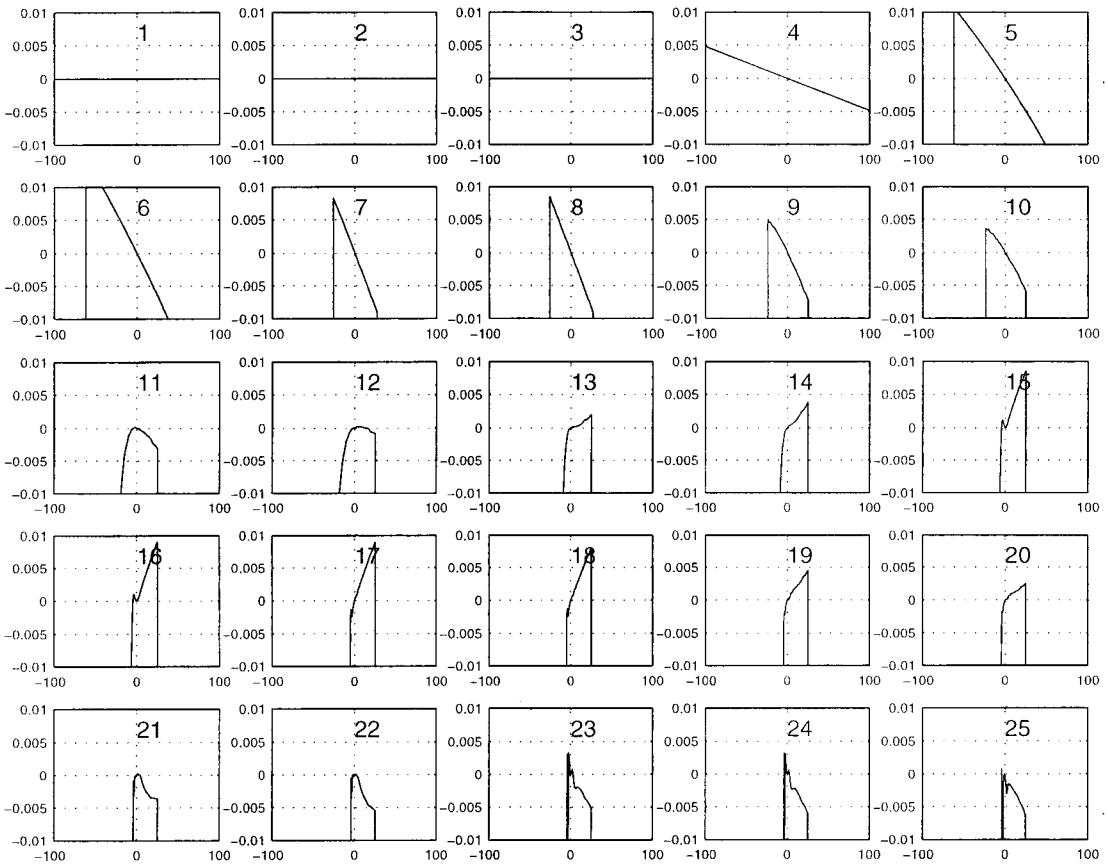

Figure 1.6: Numerical model: Dip2 deviation

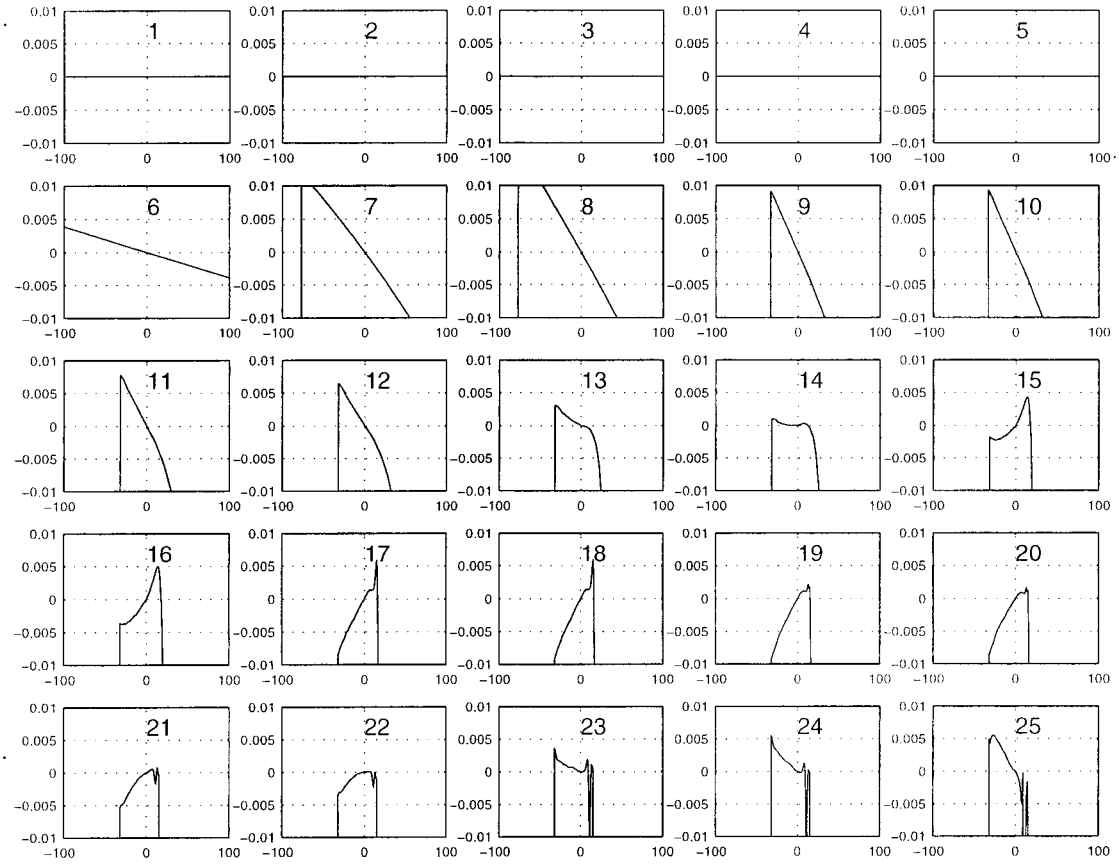

Figure 1.7: Numerical model: Dip3 deviation

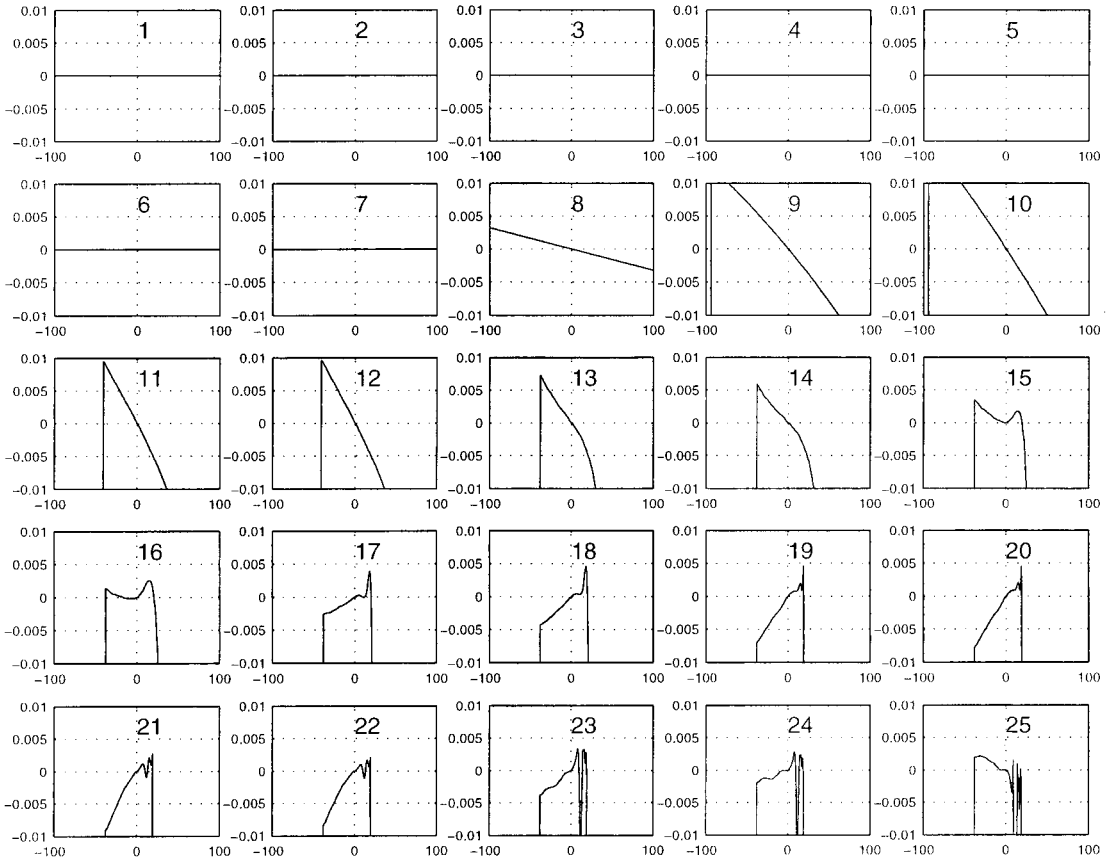

Figure 1.8: Numerical model: Dip4 deviation

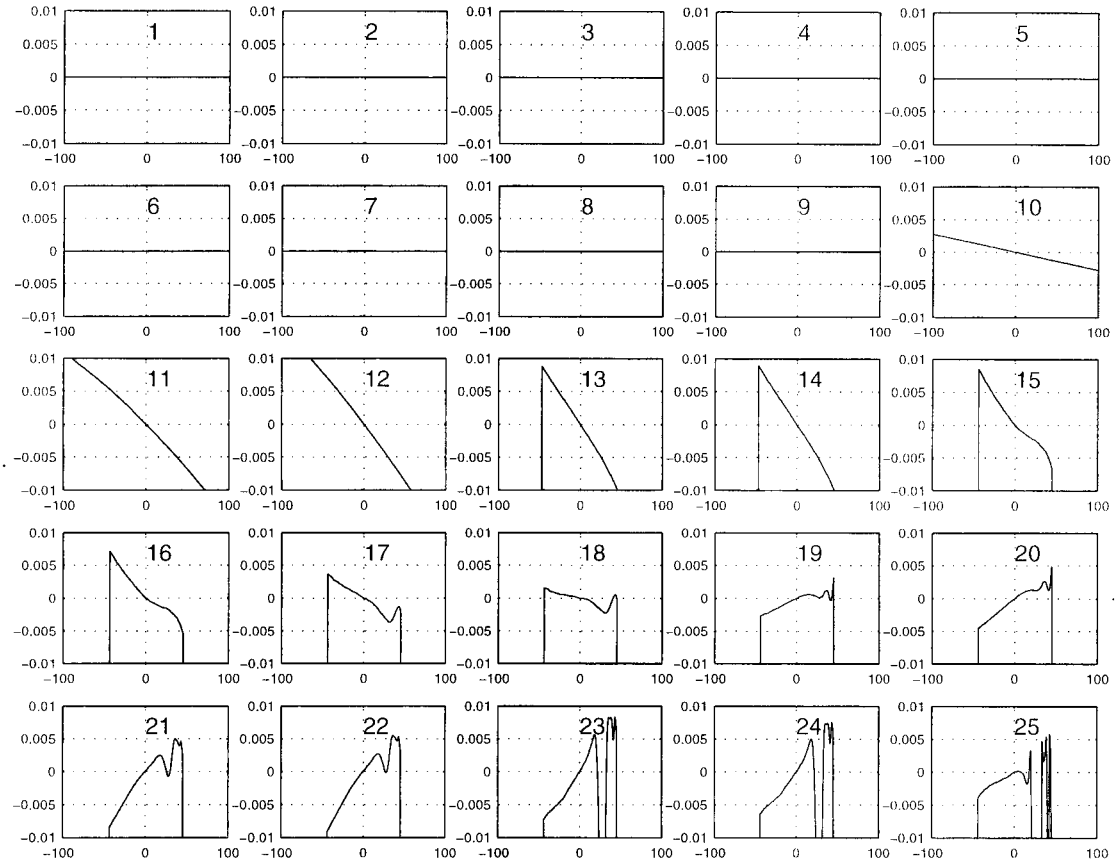

Figure 1.9: Numerical model: Dip5 deviation

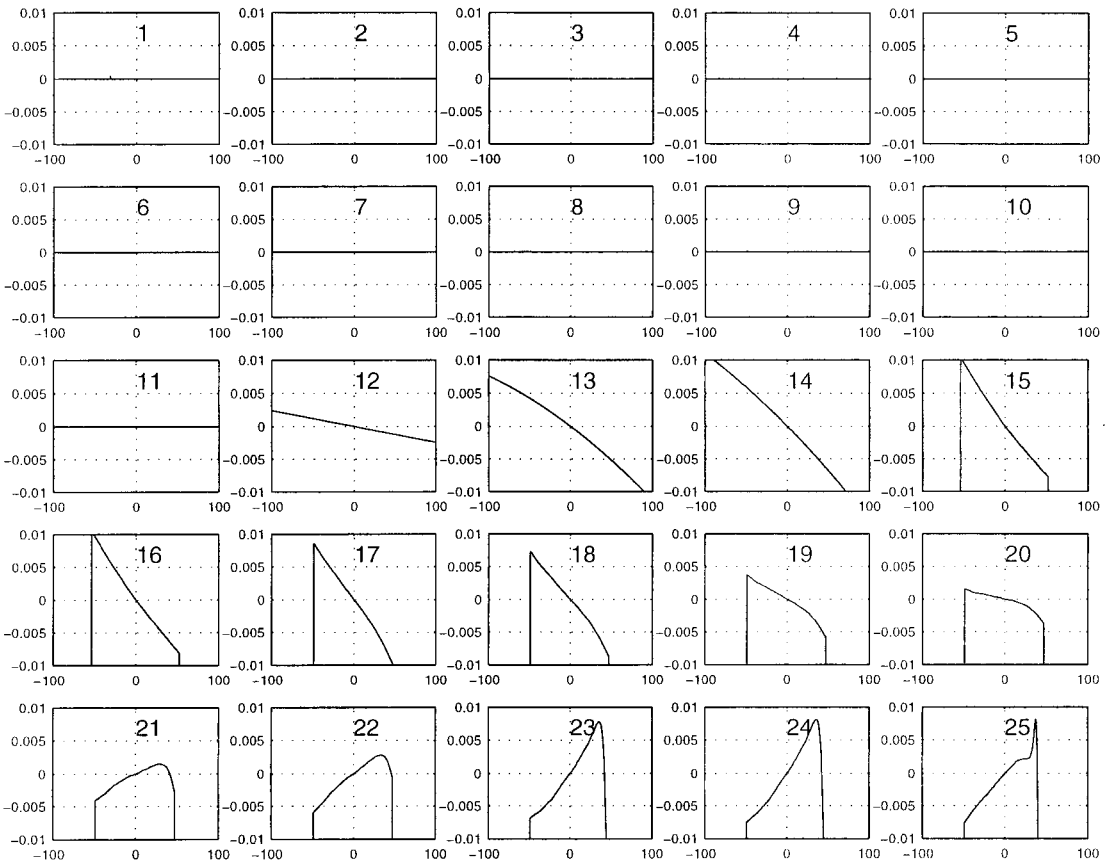

Figure 1.10: Numerical model: Dip6 deviation

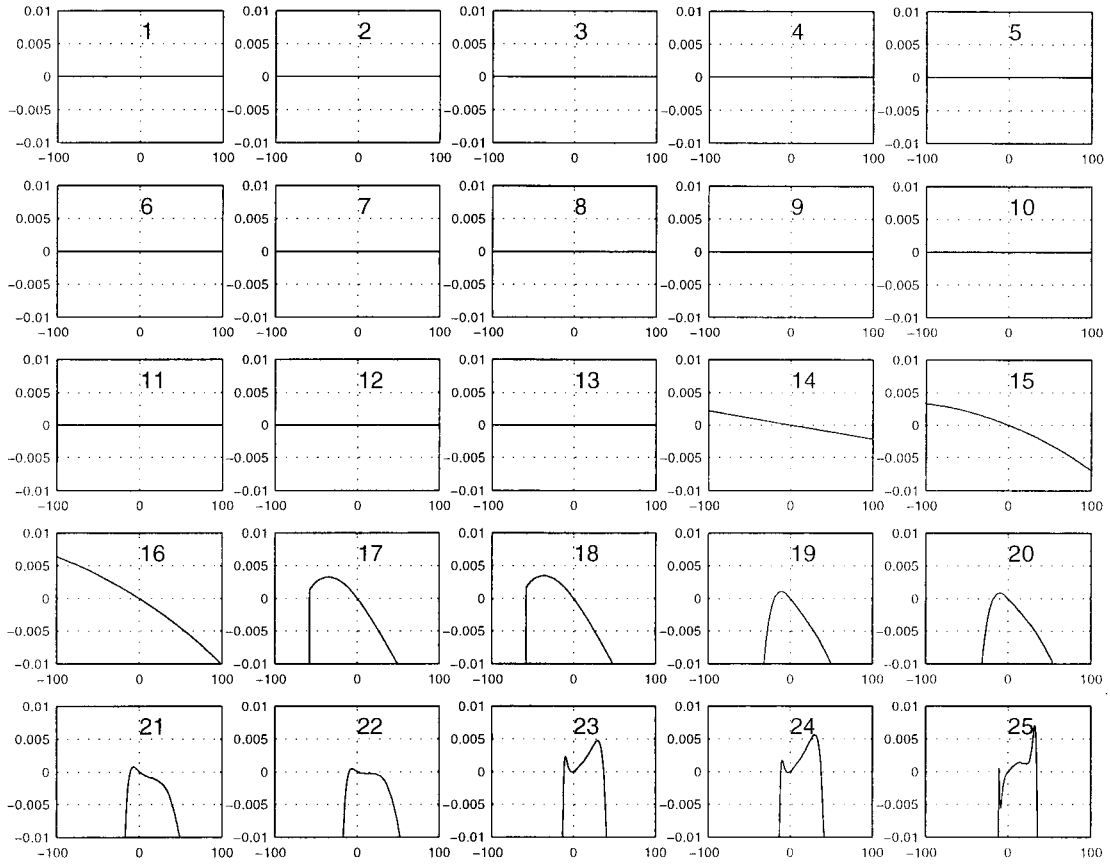

Figure 1.11: Numerical model: Dip7 deviation

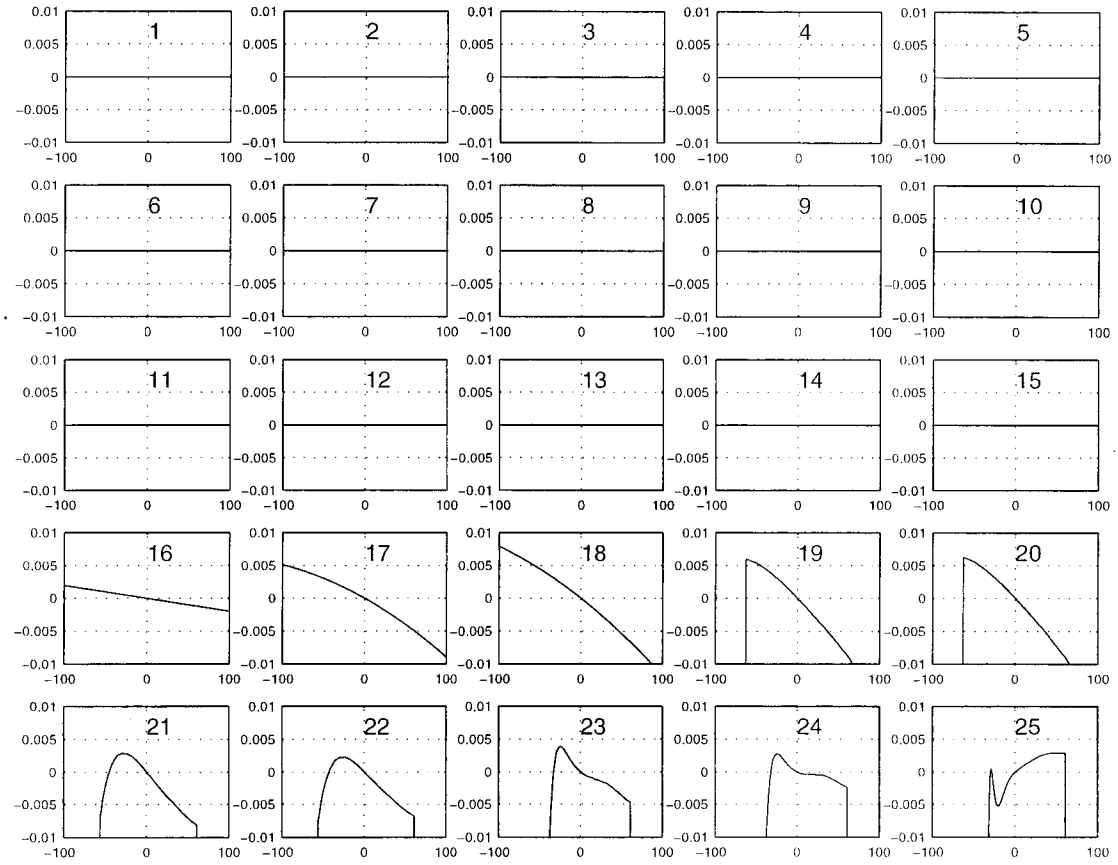

Figure 1.12: Numerical model: Dip8 deviation

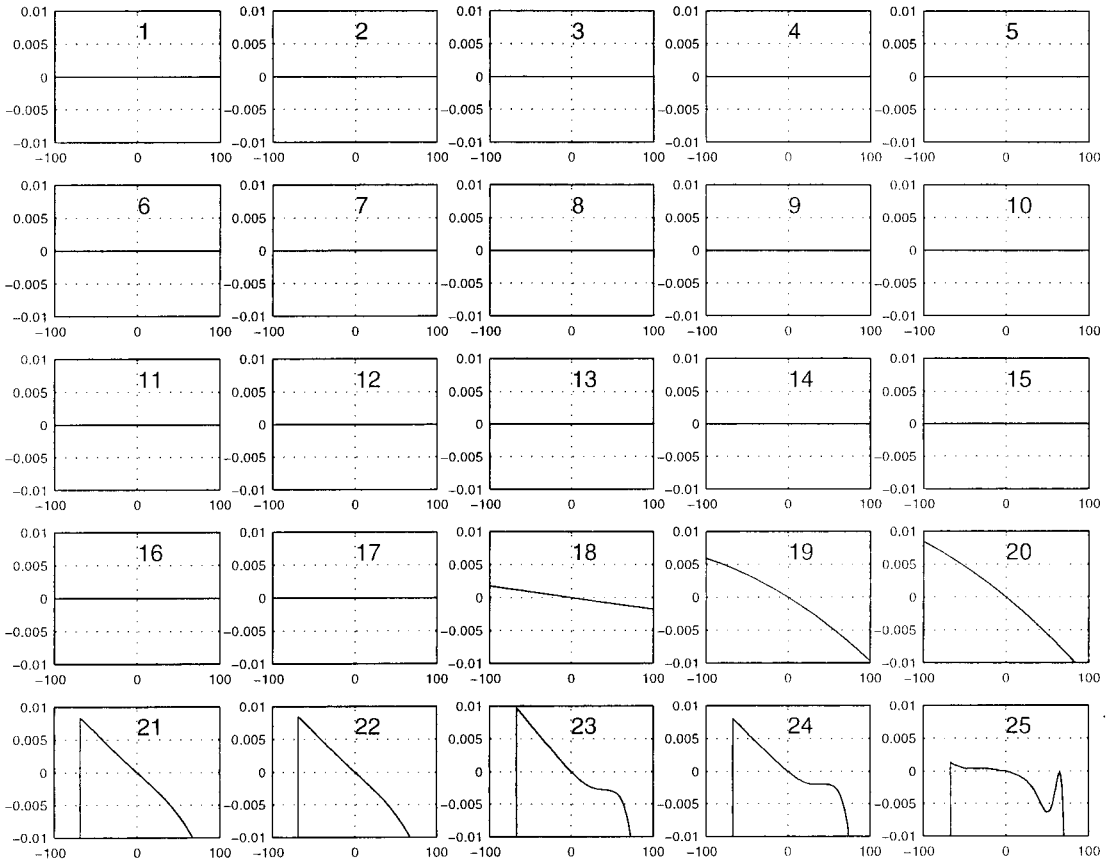

Figure 1.13: Numerical model: Dip9 deviation

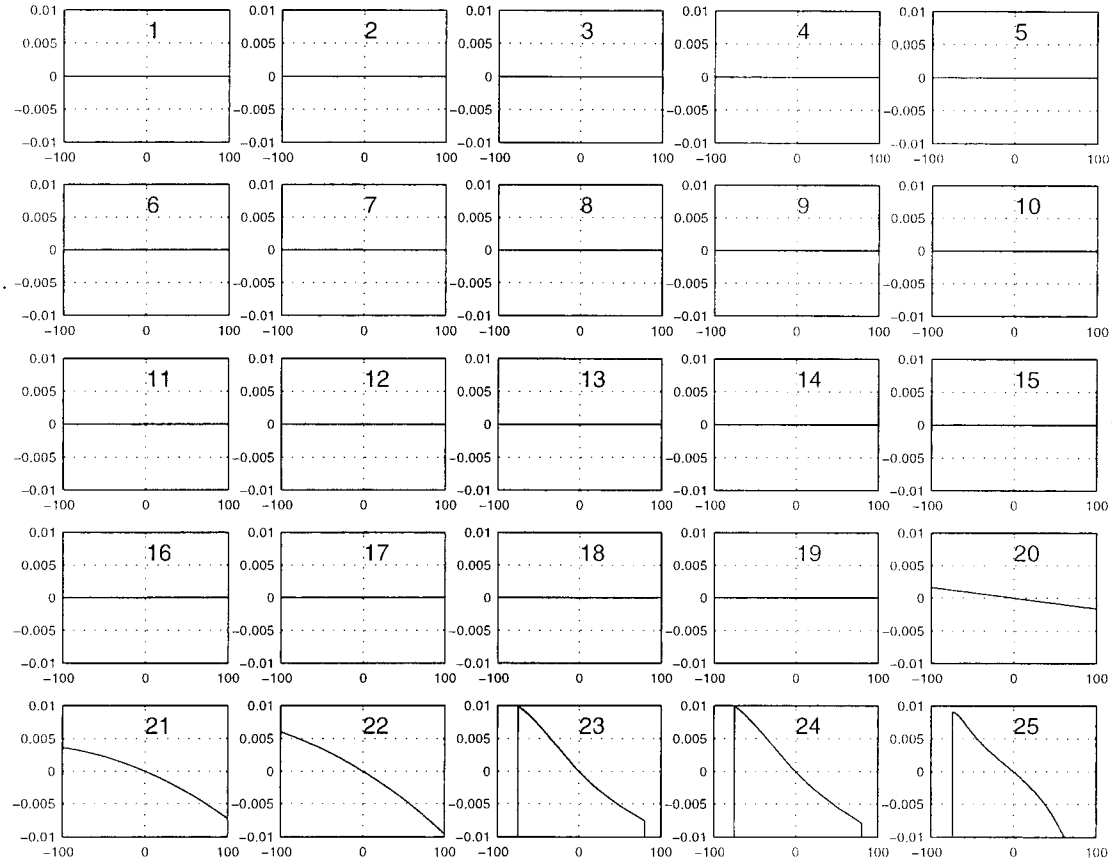

Figure 1.14: Numerical model: Dip10 deviation

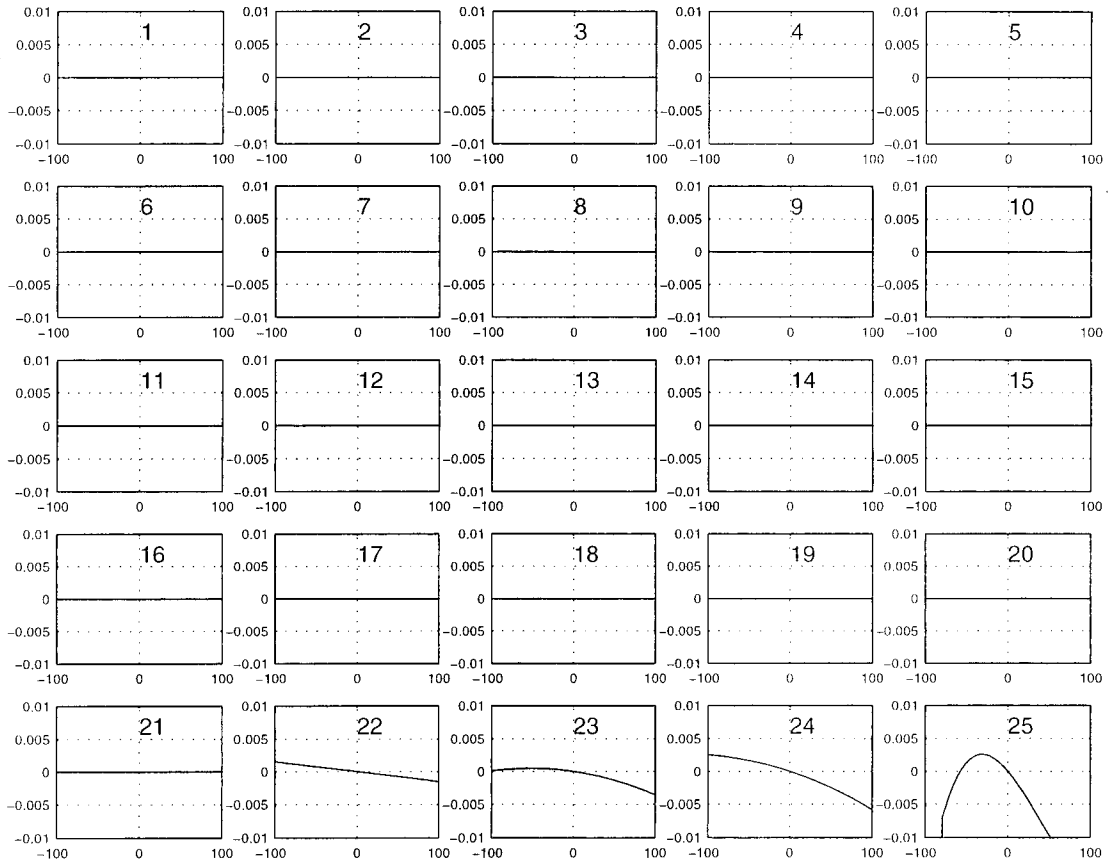

Figure 1.15: Numerical model: Dip11 deviation

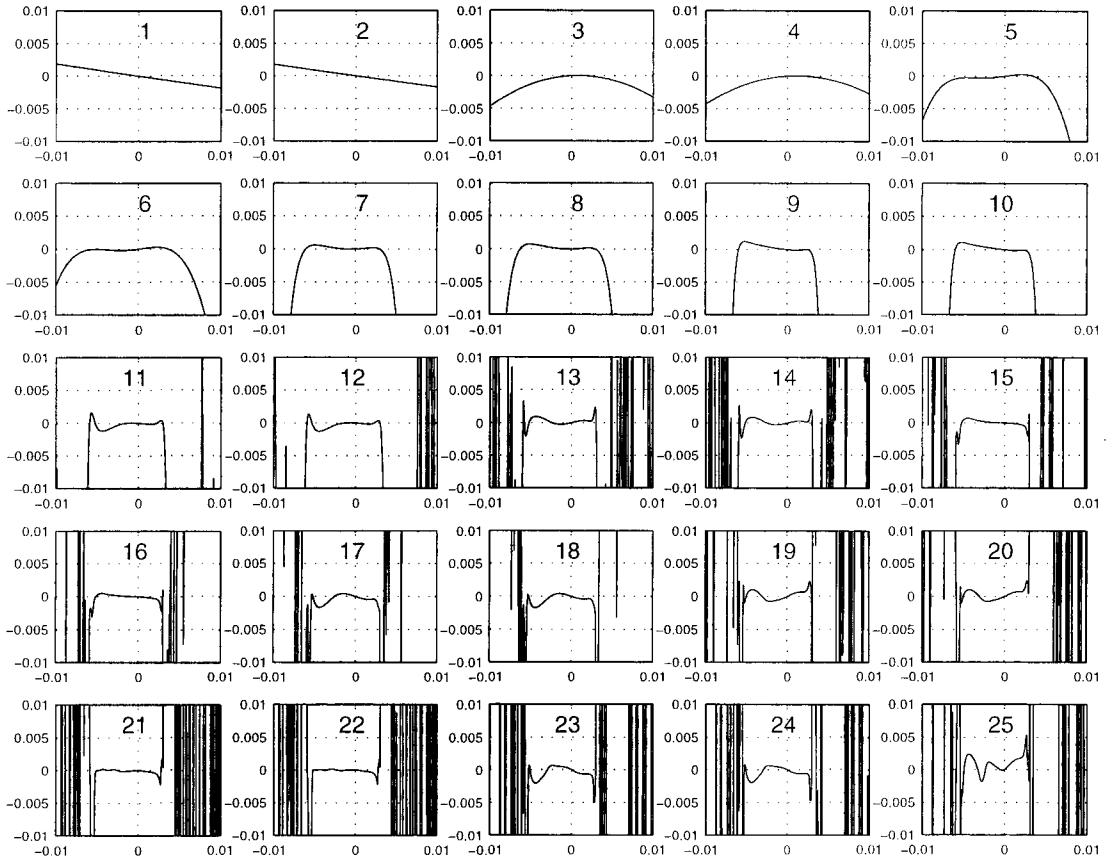

Figure 1.16: Numerical model: Dip12 deviation

2 Response Plots of Homogeneous Magnet Model

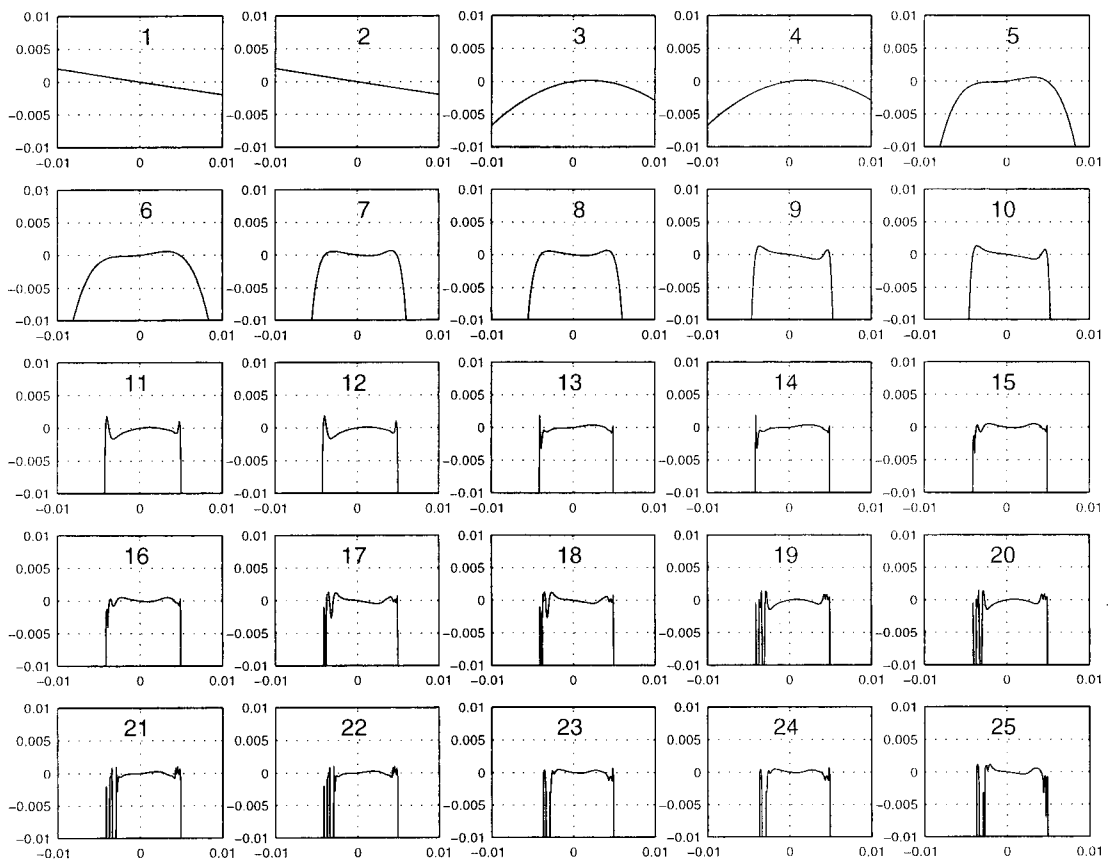

Figure 2.1: Homogeneous magnet model: M deviation

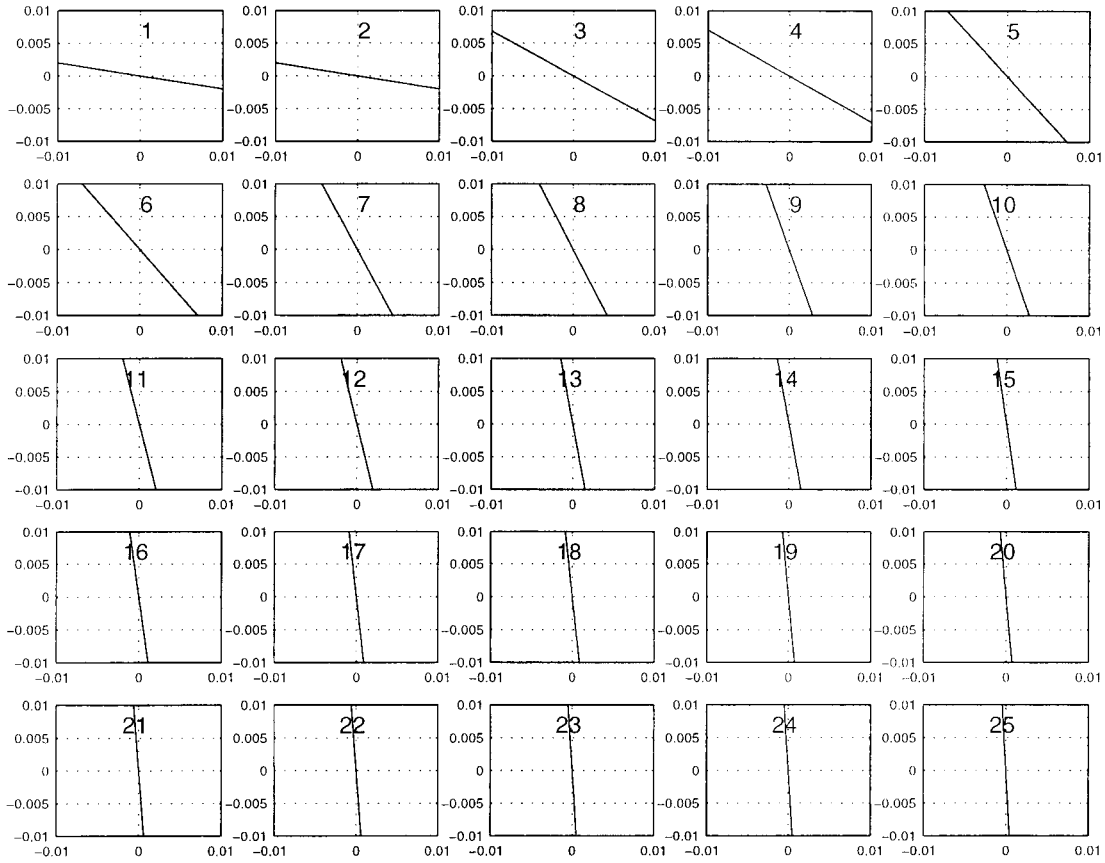

Figure 2.2: Homogeneous magnet model: D deviation

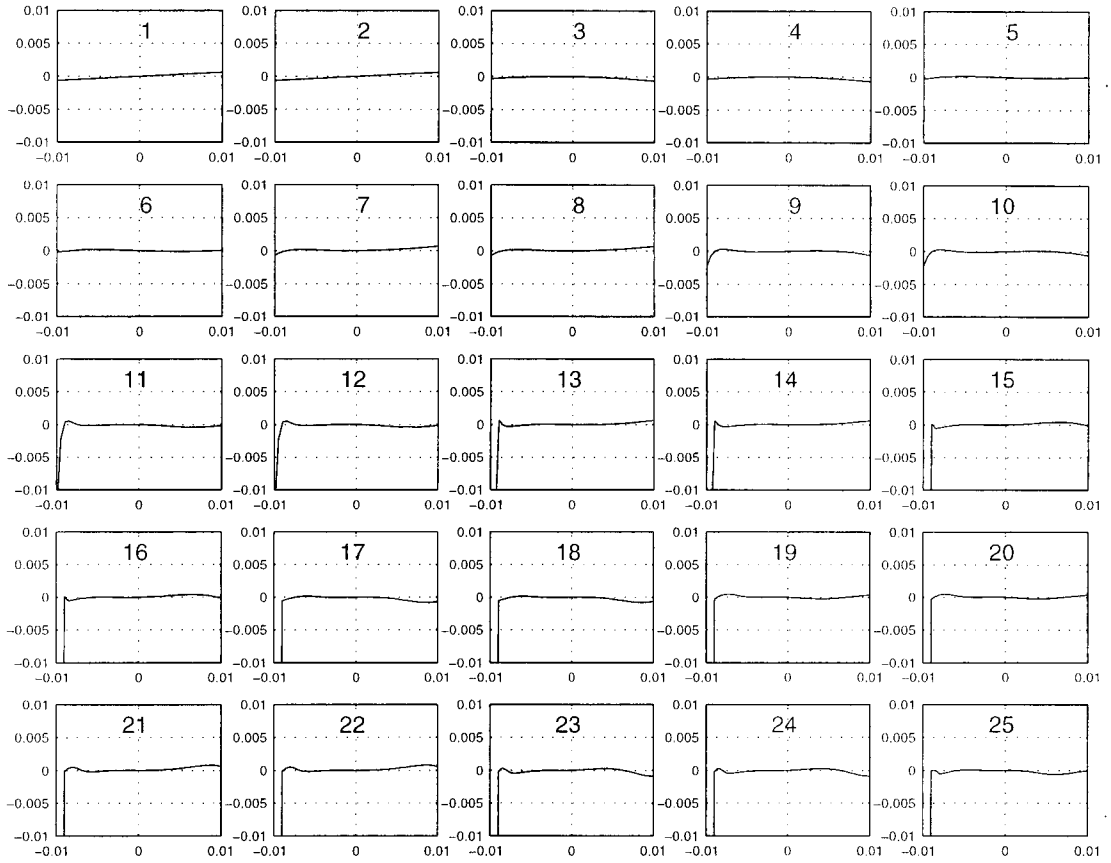

Figure 2.3: Homogeneous magnet model: E deviation

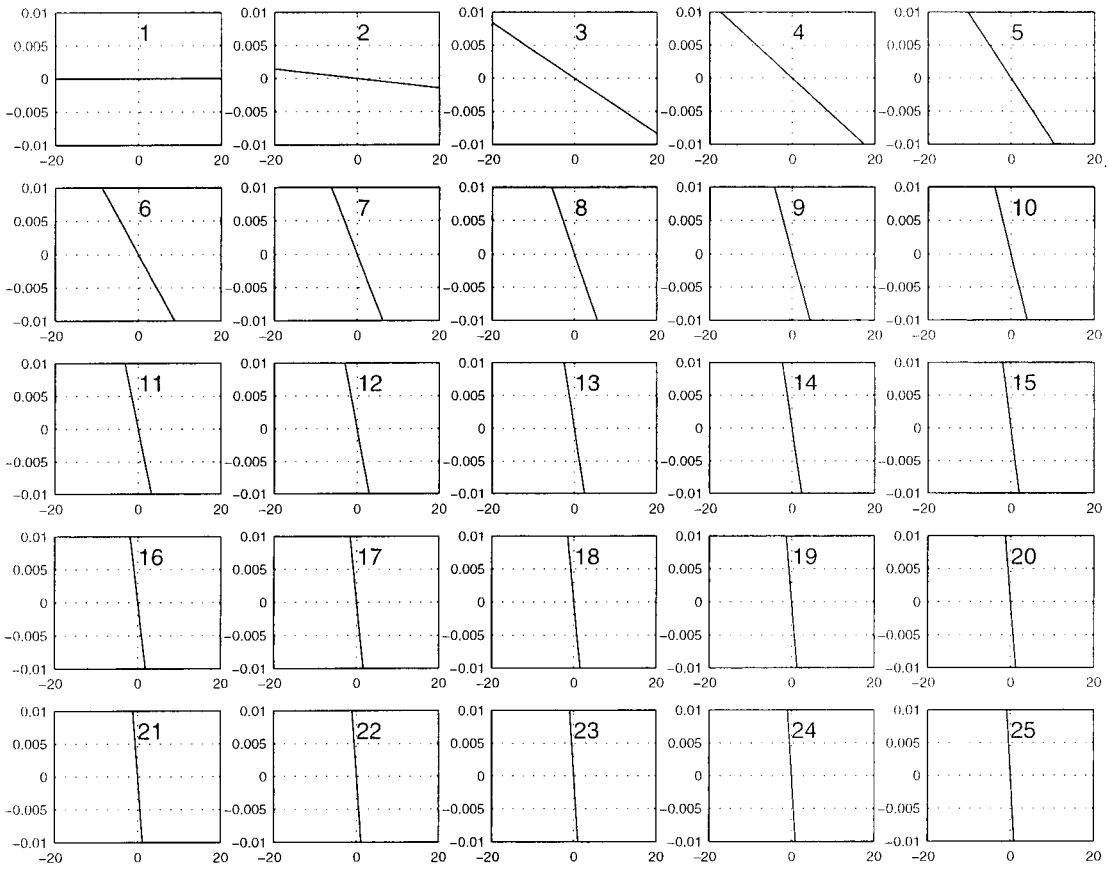

Figure 2.4: Homogeneous magnet model: P deviation

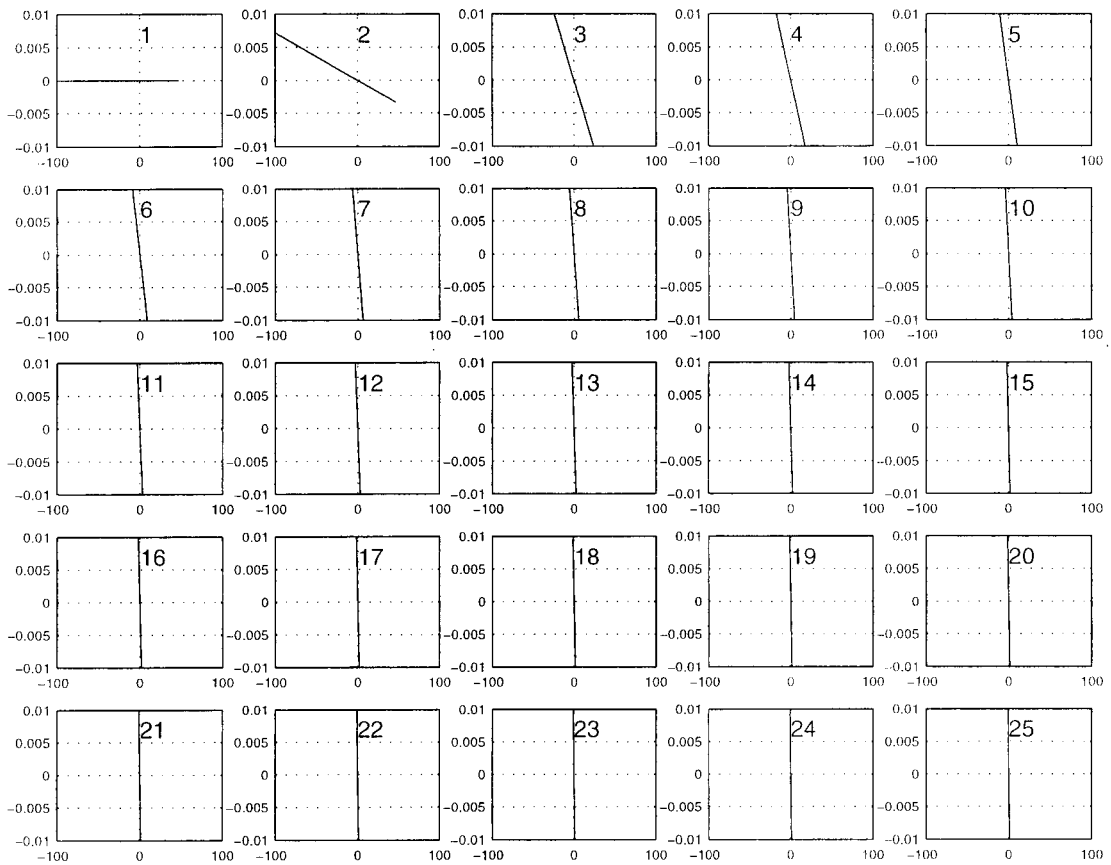

Figure 2.5: Homogeneous magnet model: Dip1 deviation

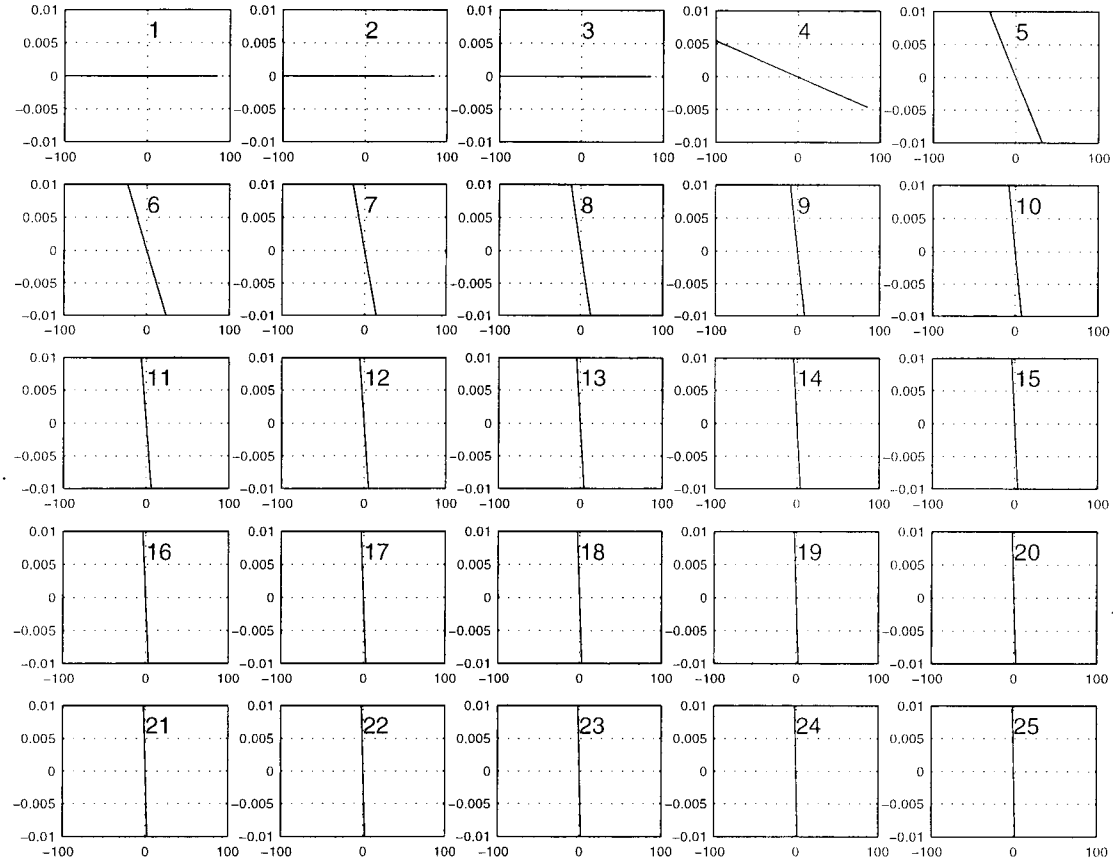

Figure 2.6: Homogeneous magnet model: Dip2 deviation

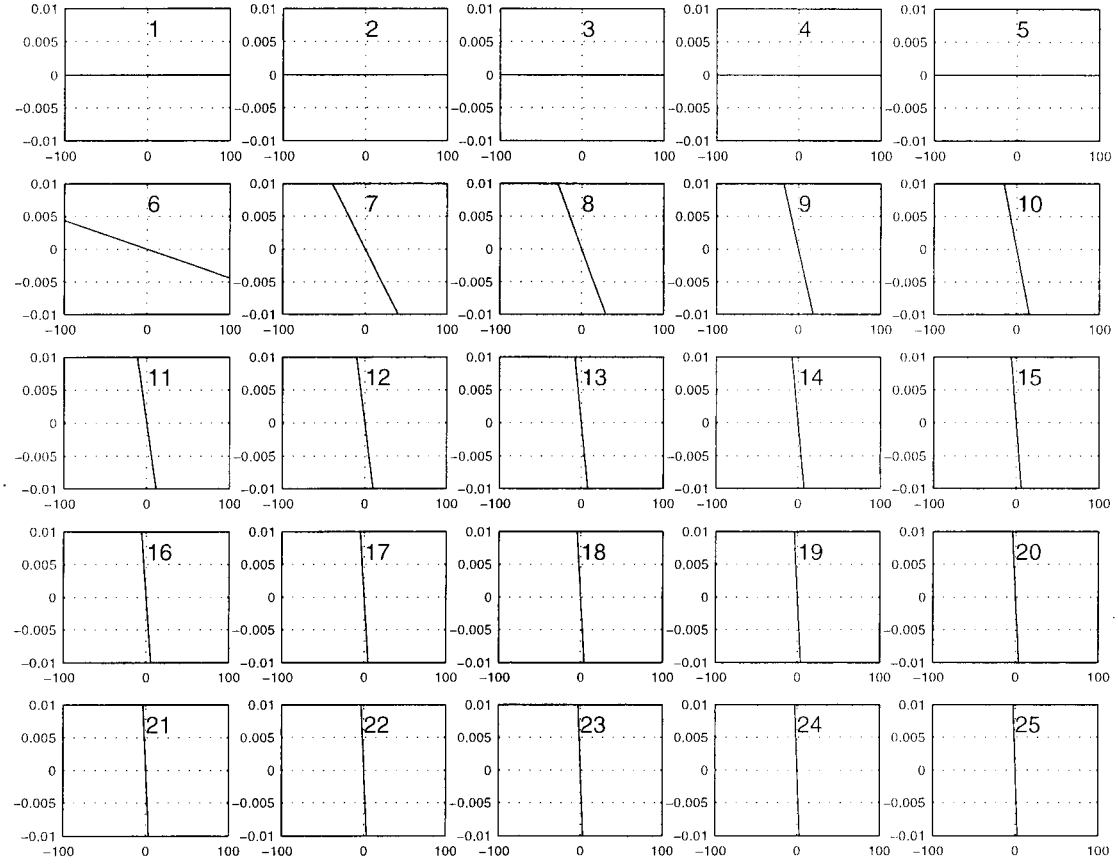

Figure 2.7: Homogeneous magnet model: Dip3 deviation

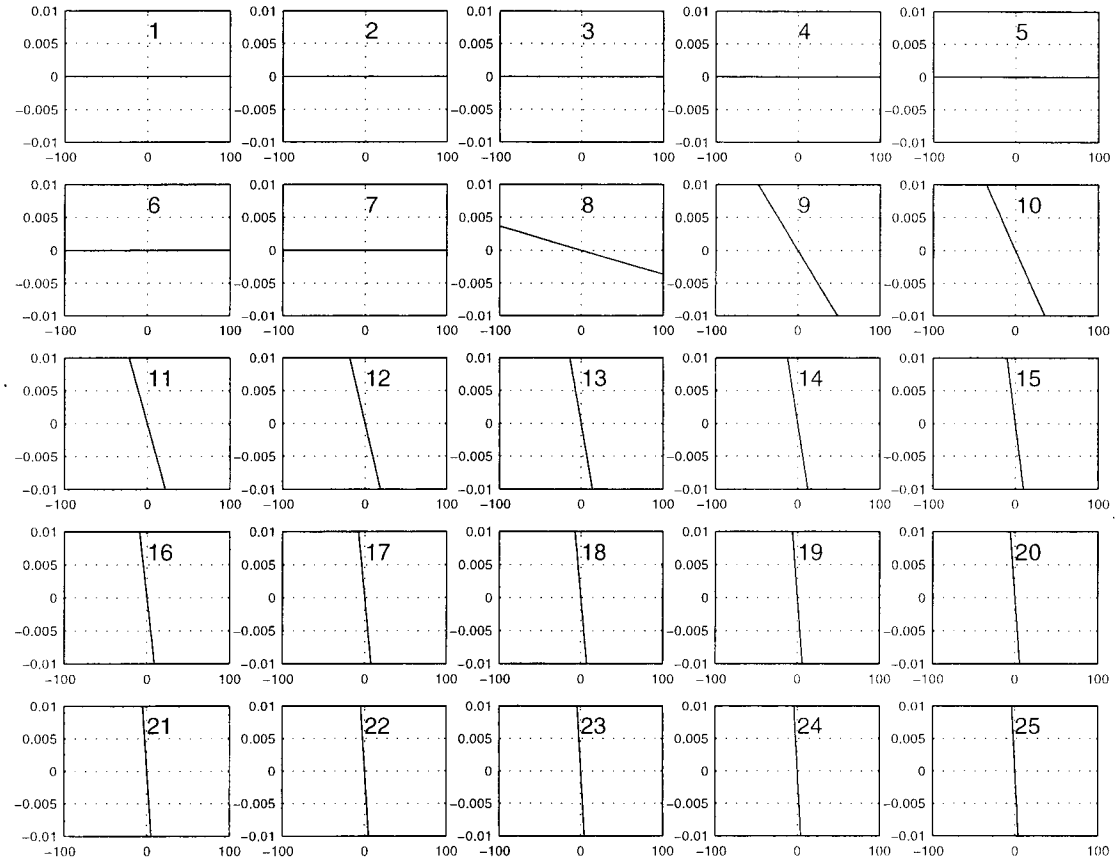

Figure 2.8: Homogeneous magnet model: Dip4 deviation

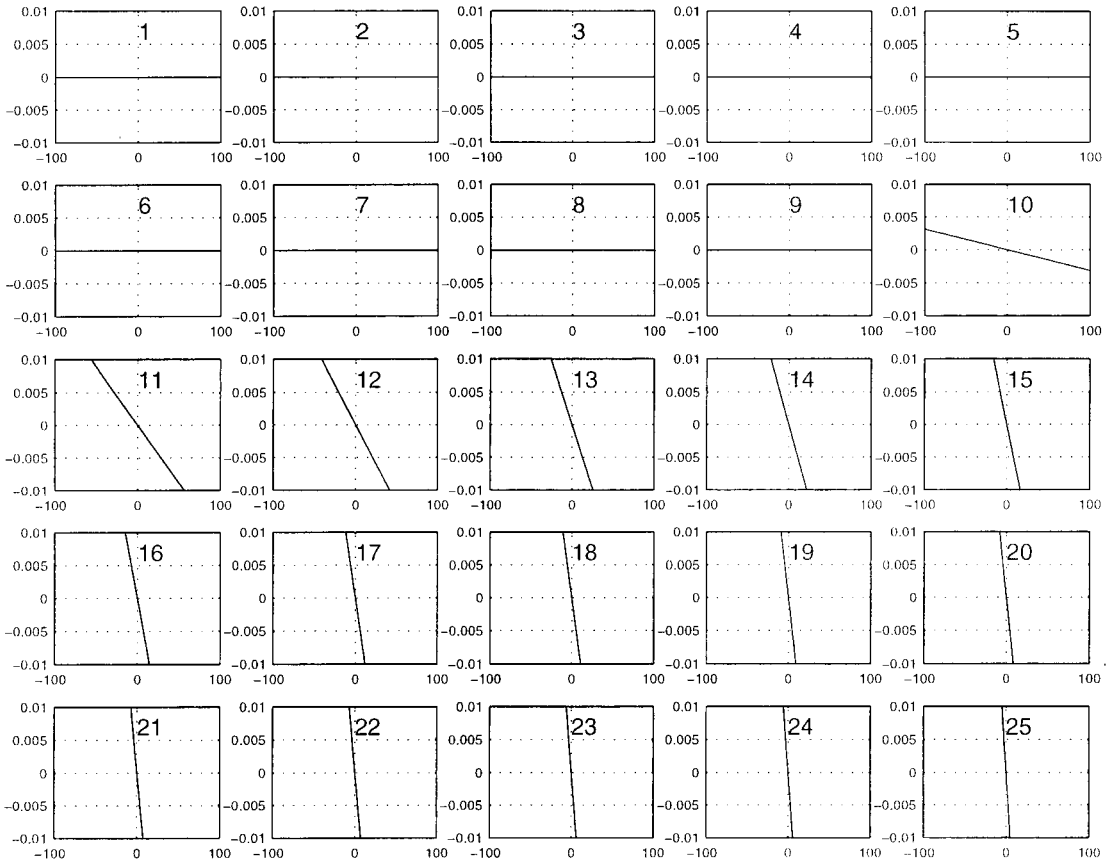

Figure 2.9: Homogeneous magnet model: Dip5 deviation

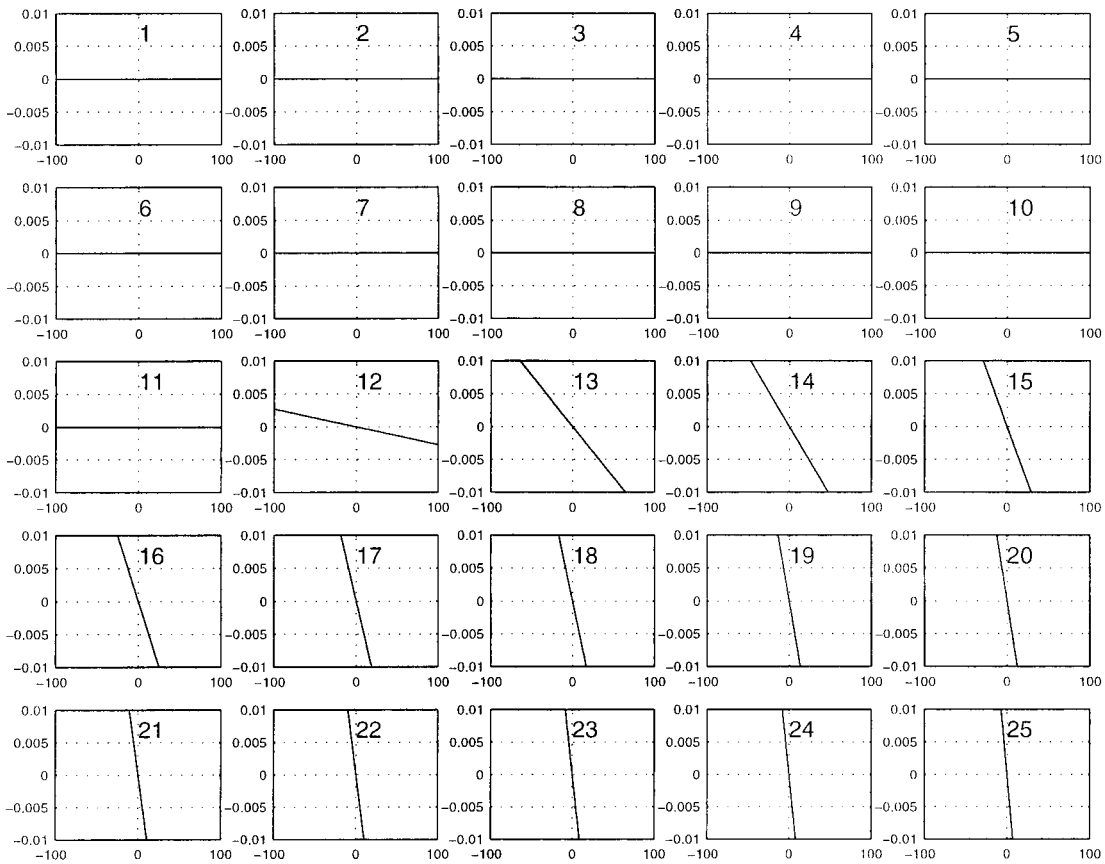

Figure 2.10: Homogeneous magnet model: Dip6 deviation

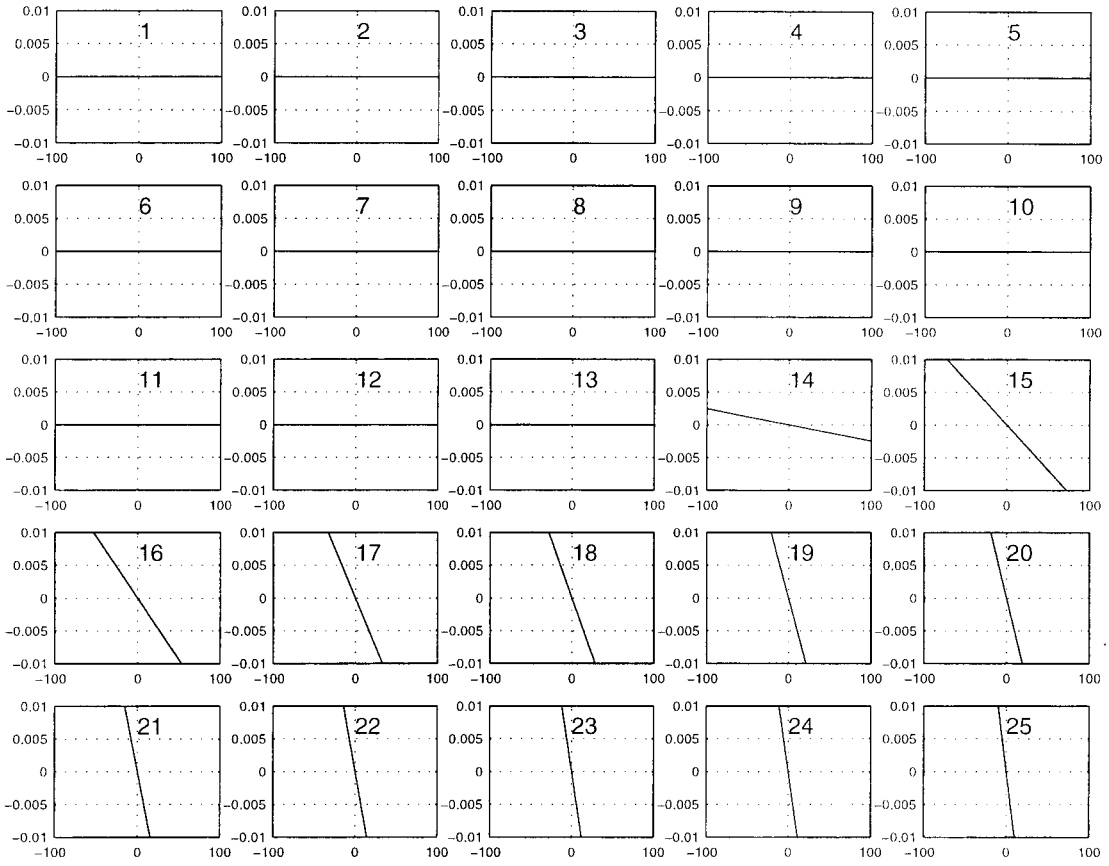

Figure 2.11: Homogeneous magnet model: Dip7 deviation

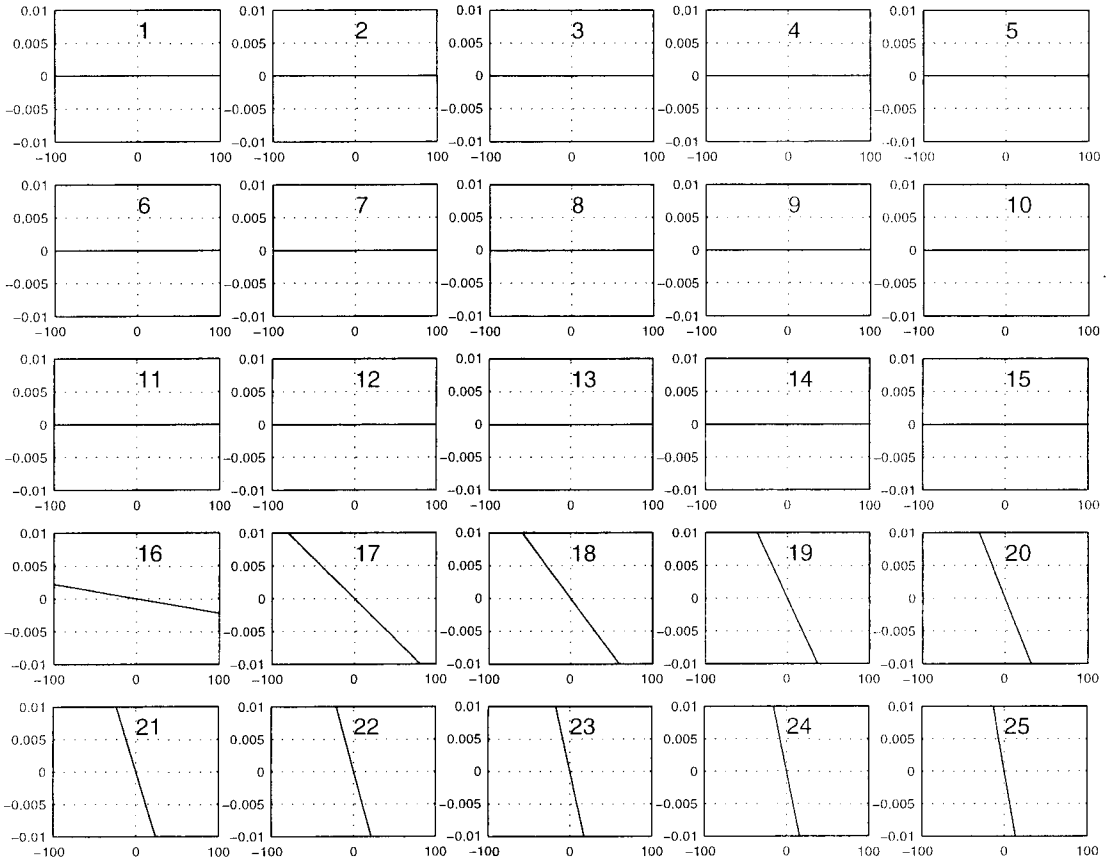

Figure 2.12: Homogeneous magnet model: Dip8 deviation

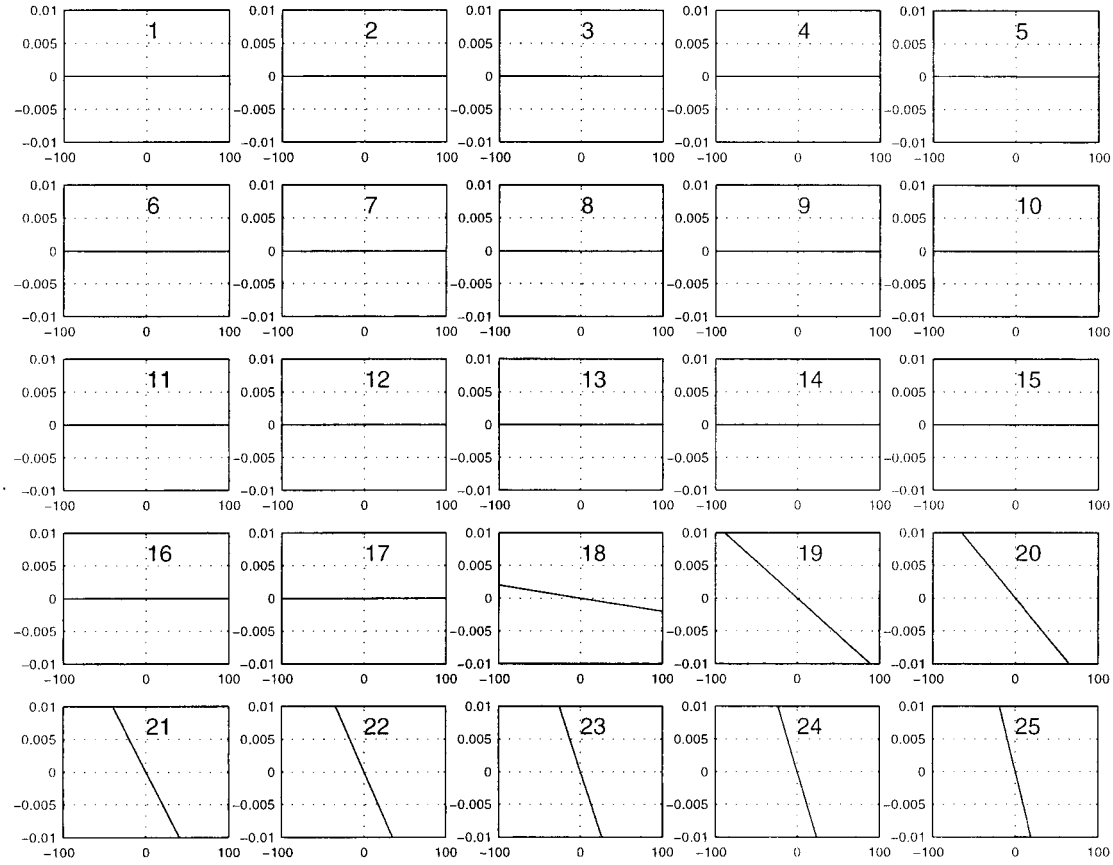

Figure 2.13: Homogeneous magnet model: Dip9 deviation

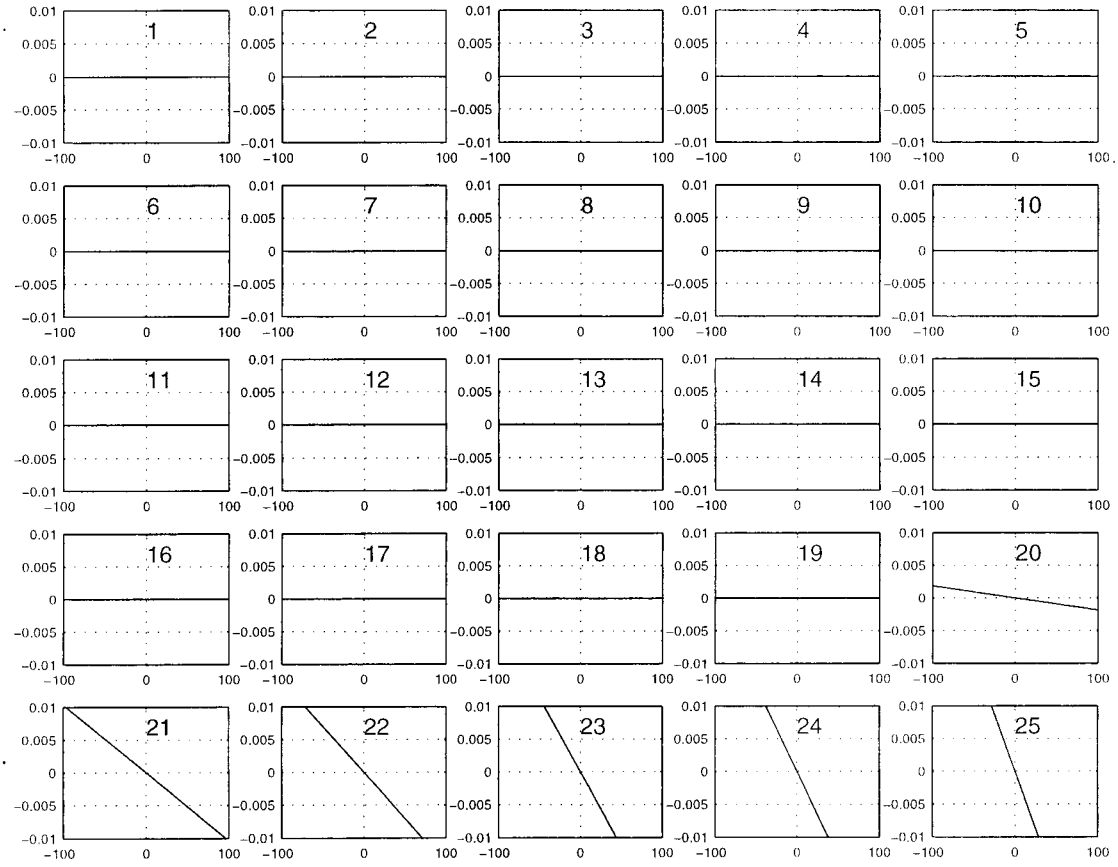

Figure 2.14: Homogeneous magnet model: Dip10 deviation

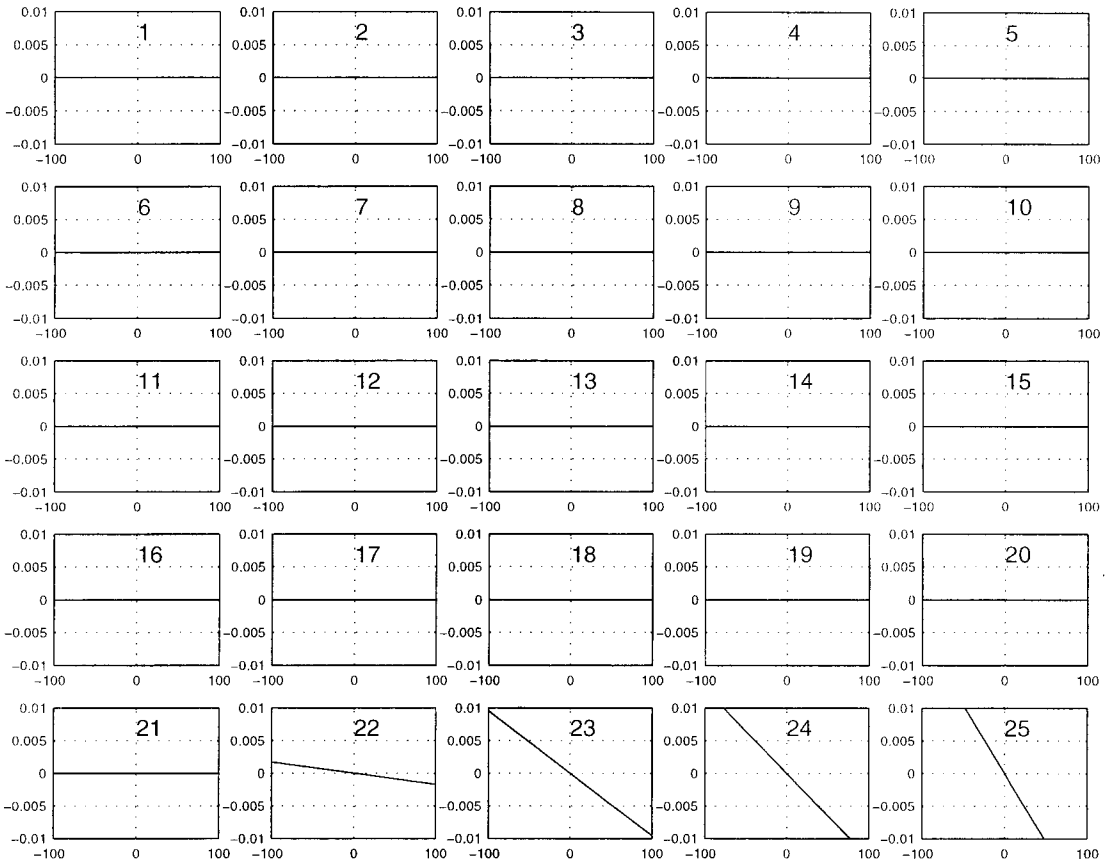

Figure 2.15: Homogeneous magnet model: Dip11 deviation

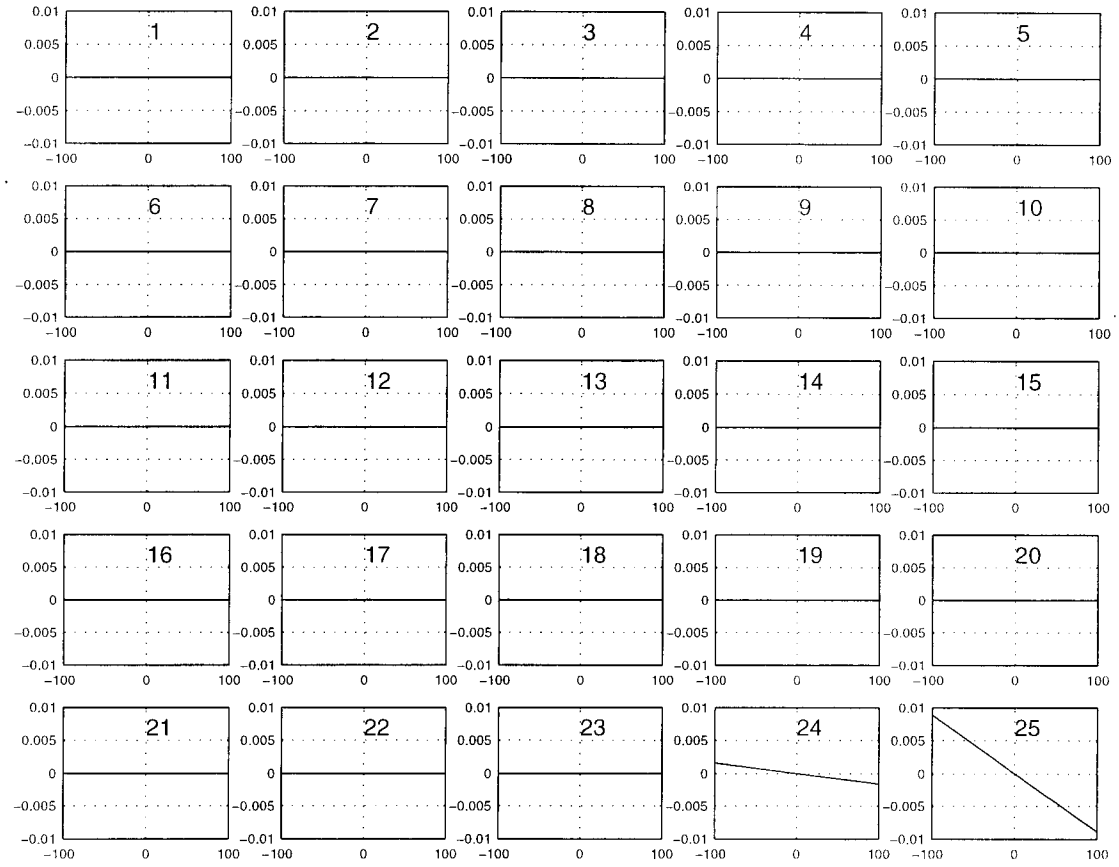

Figure 2.16: Homogeneous magnet model: Dip12 deviation

3 Response plots of two-field-sector magnet model

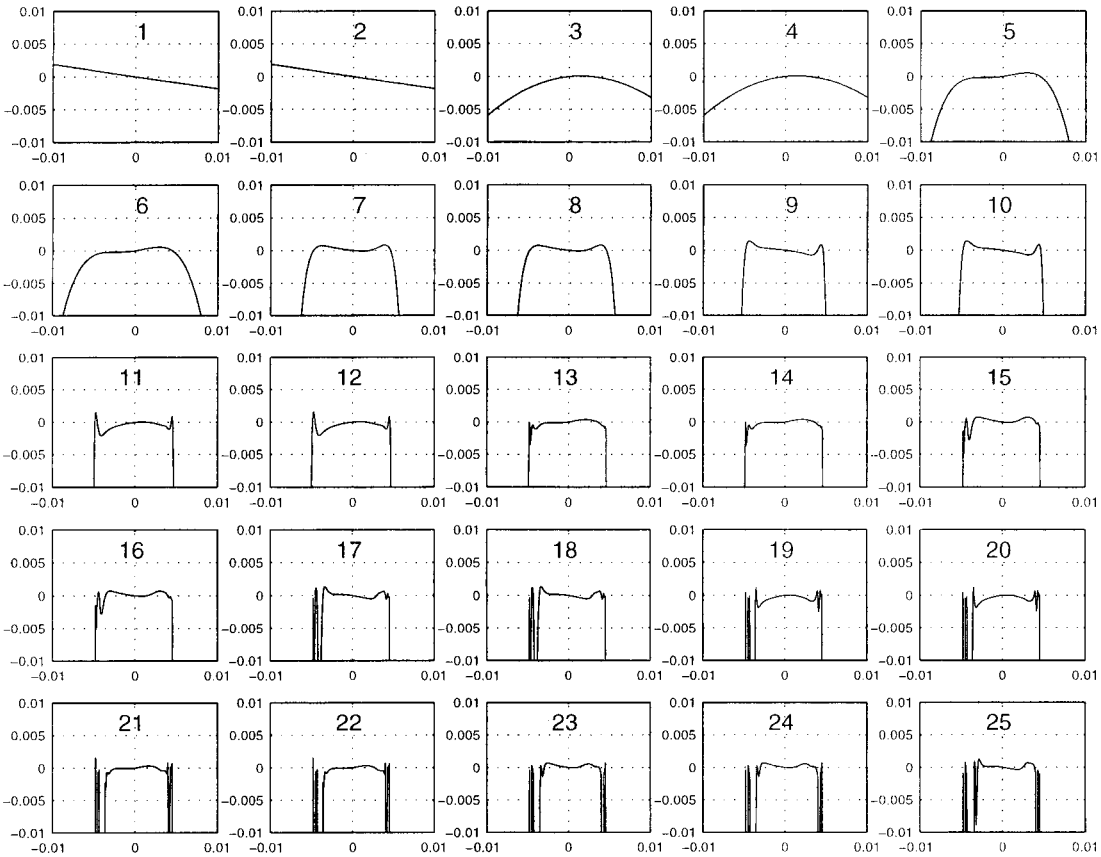

Figure 3.1: Two-Field-Sector magnet model: M deviation

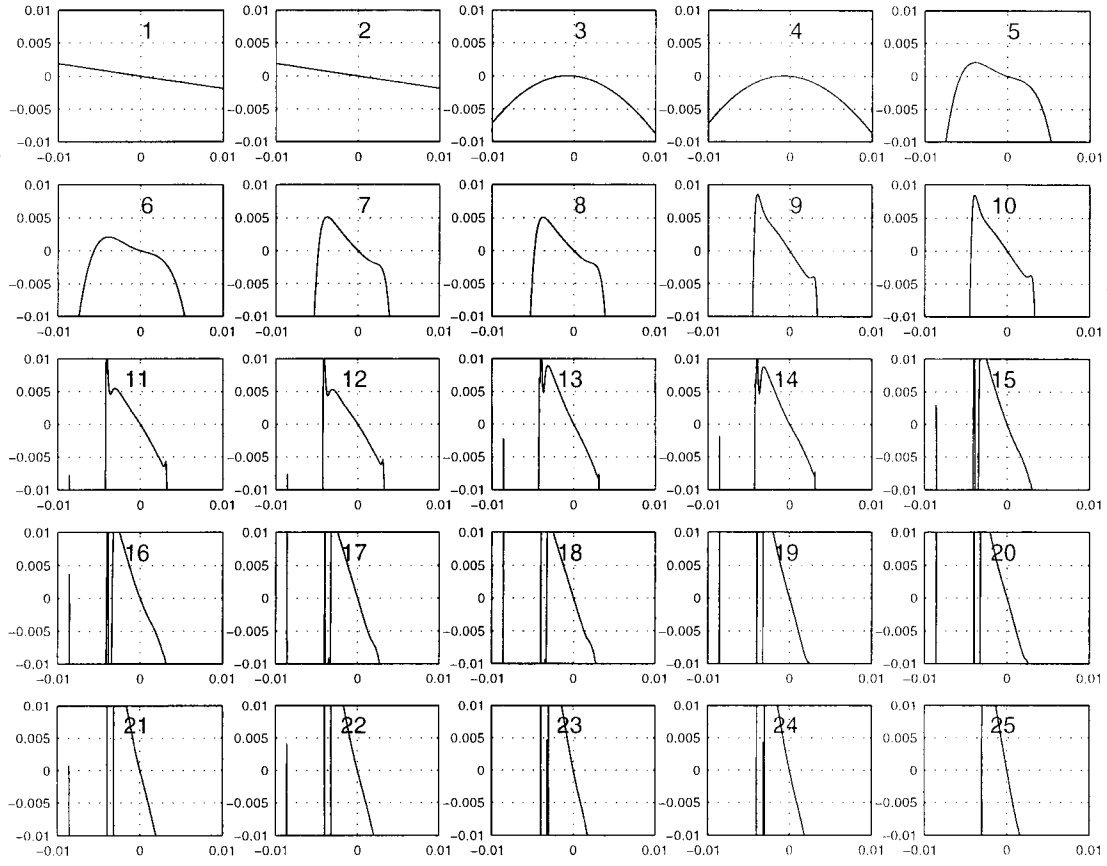

Figure 3.2: Two-Field-Sector magnet model: D deviation

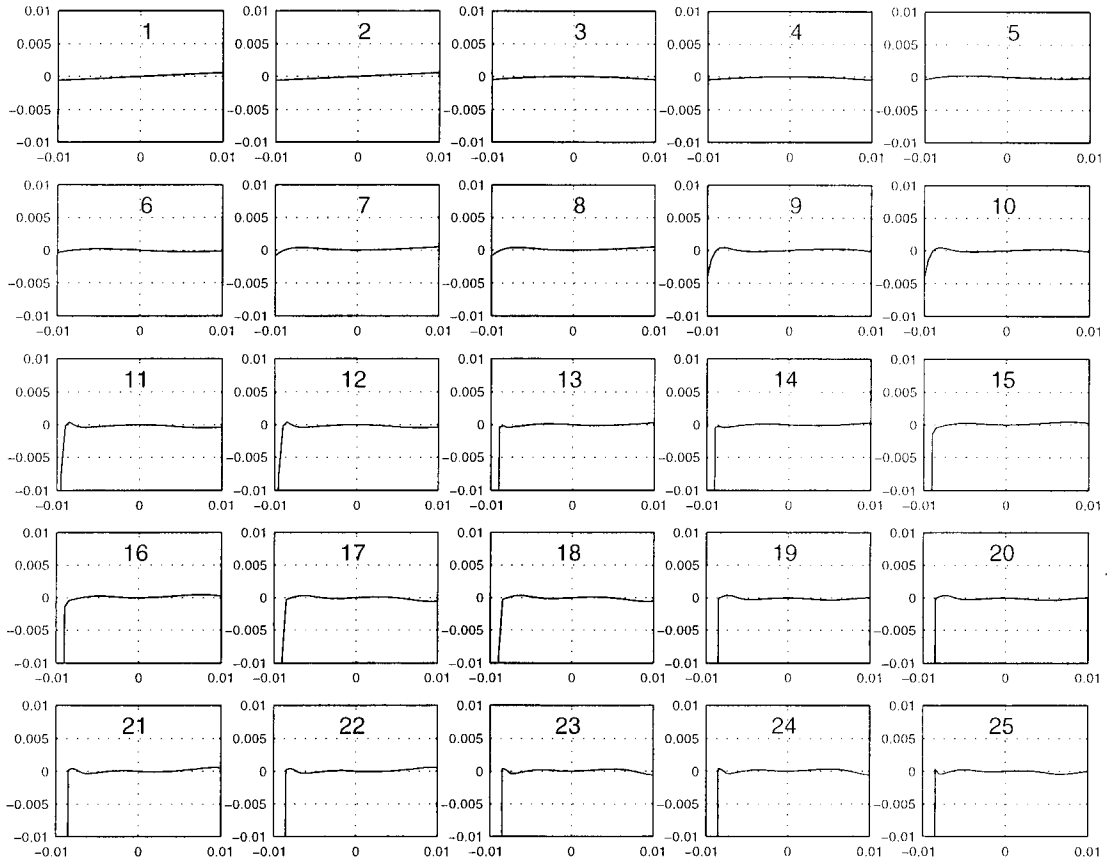

Figure 3.3: Two-Field-Sector magnet model: E deviation

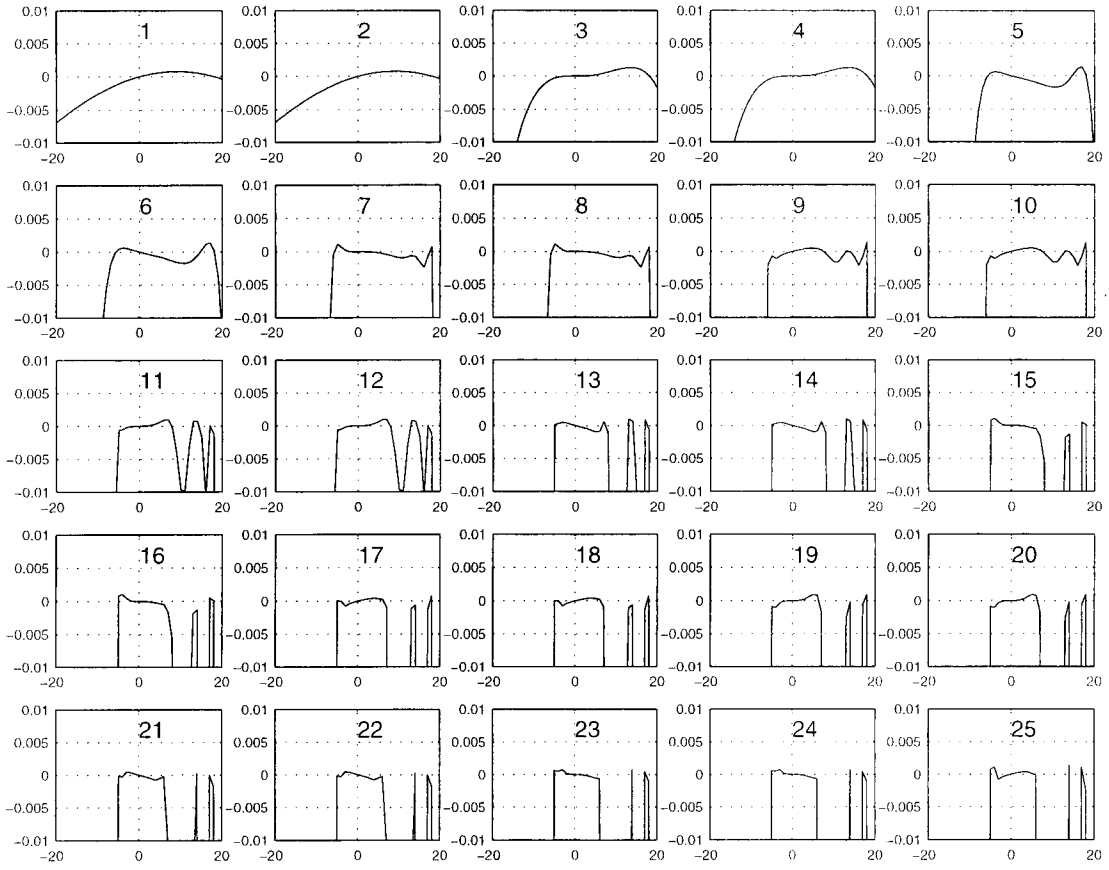

Figure 3.4: Two-Field-Sector magnet model: P deviation

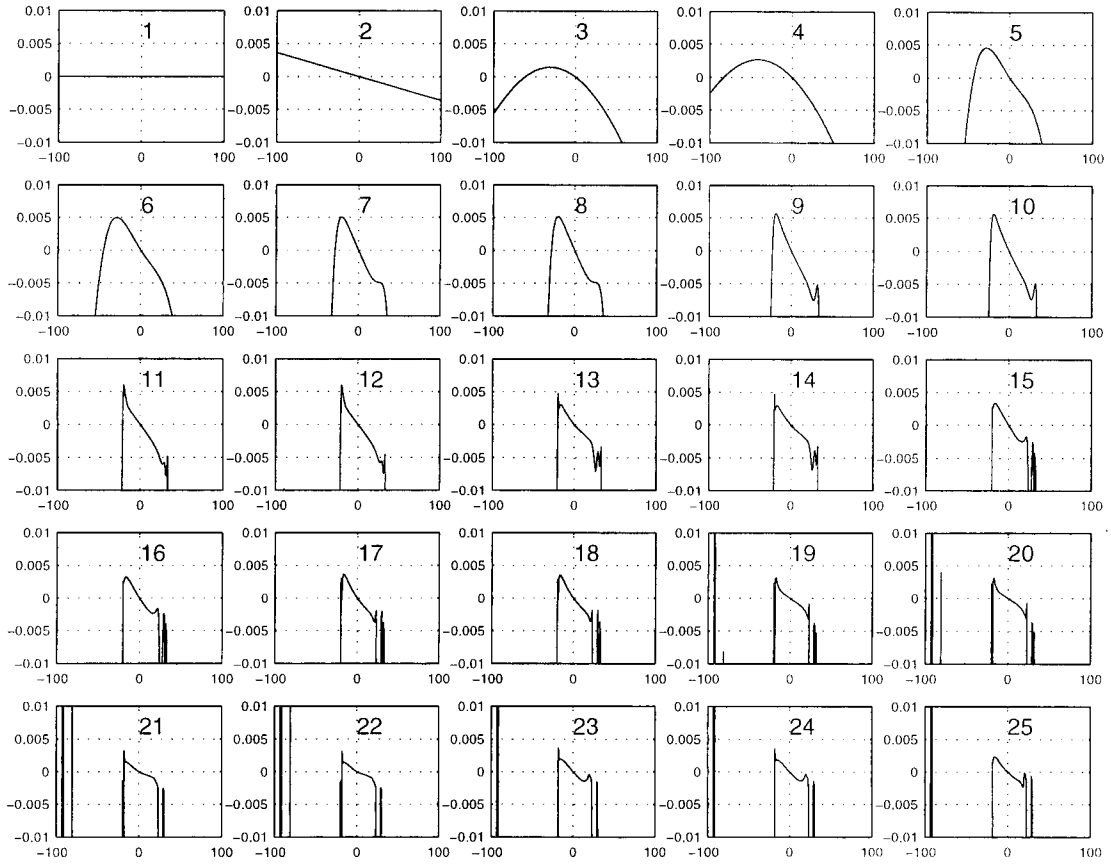

Figure 3.5: Two-Field-Sector magnet model: Dip1 deviation

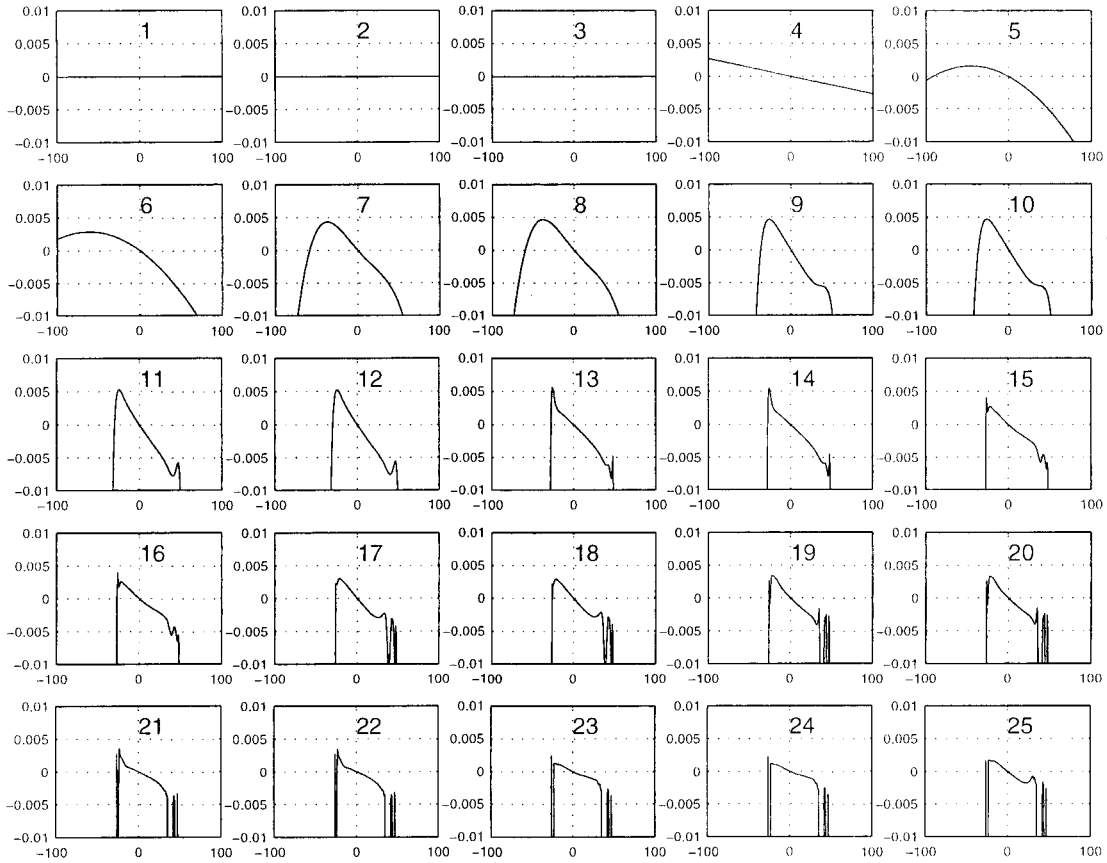

Figure 3.6: Two-Field-Sector magnet model: Dip2 deviation

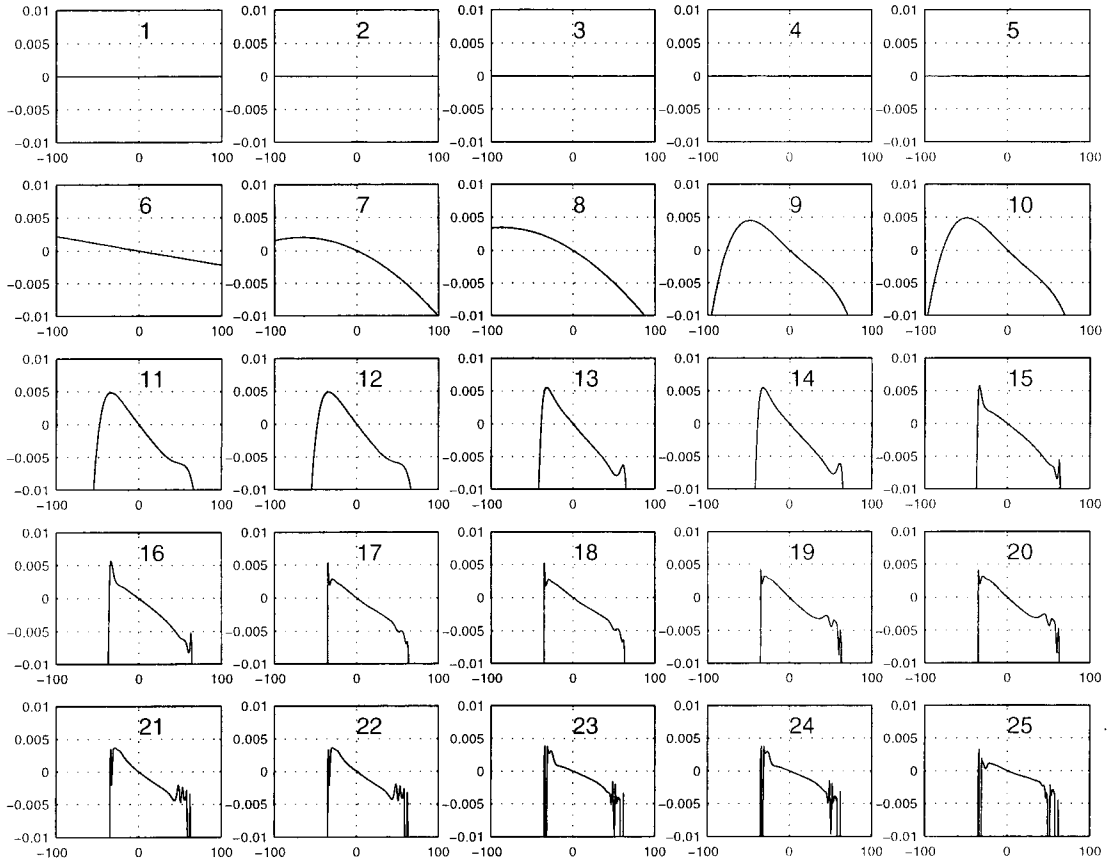

Figure 3.7: Two-Field-Sector magnet model: Dip3 deviation

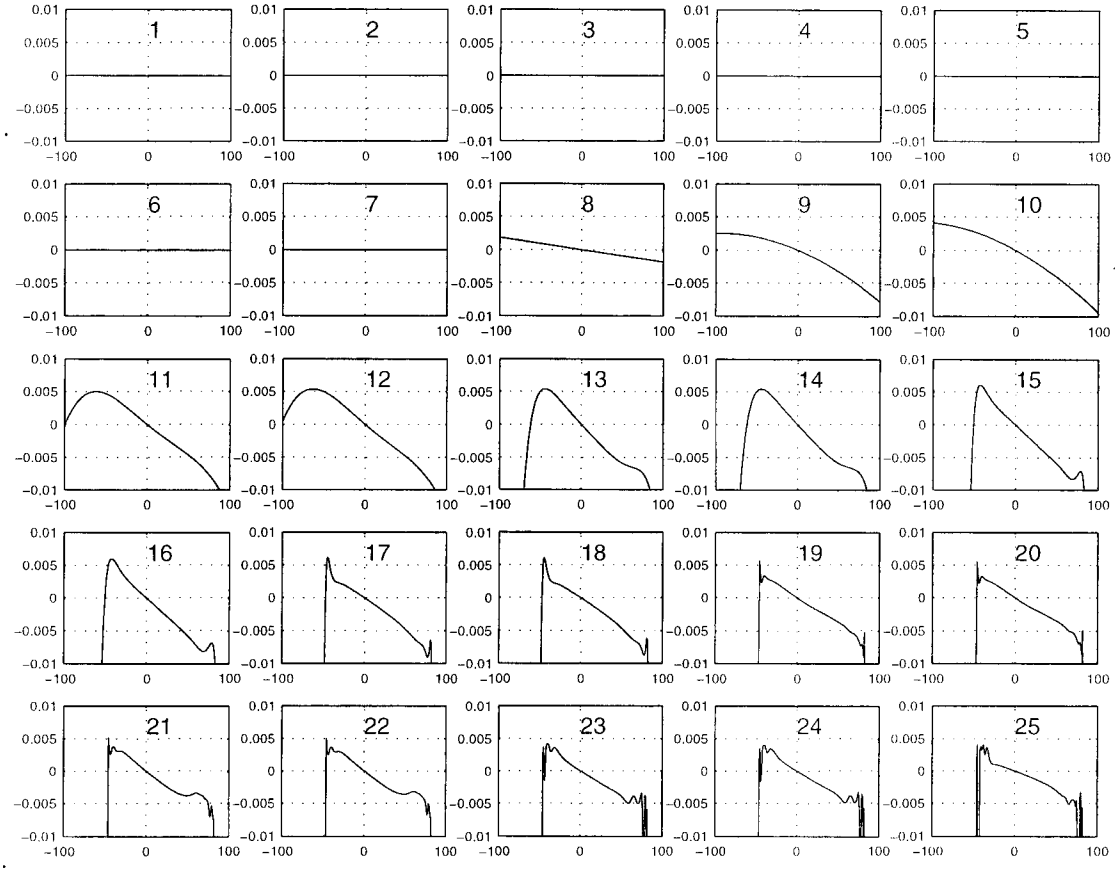

Figure 3.8: Two-Field-Sector magnet model: Dip4 deviation

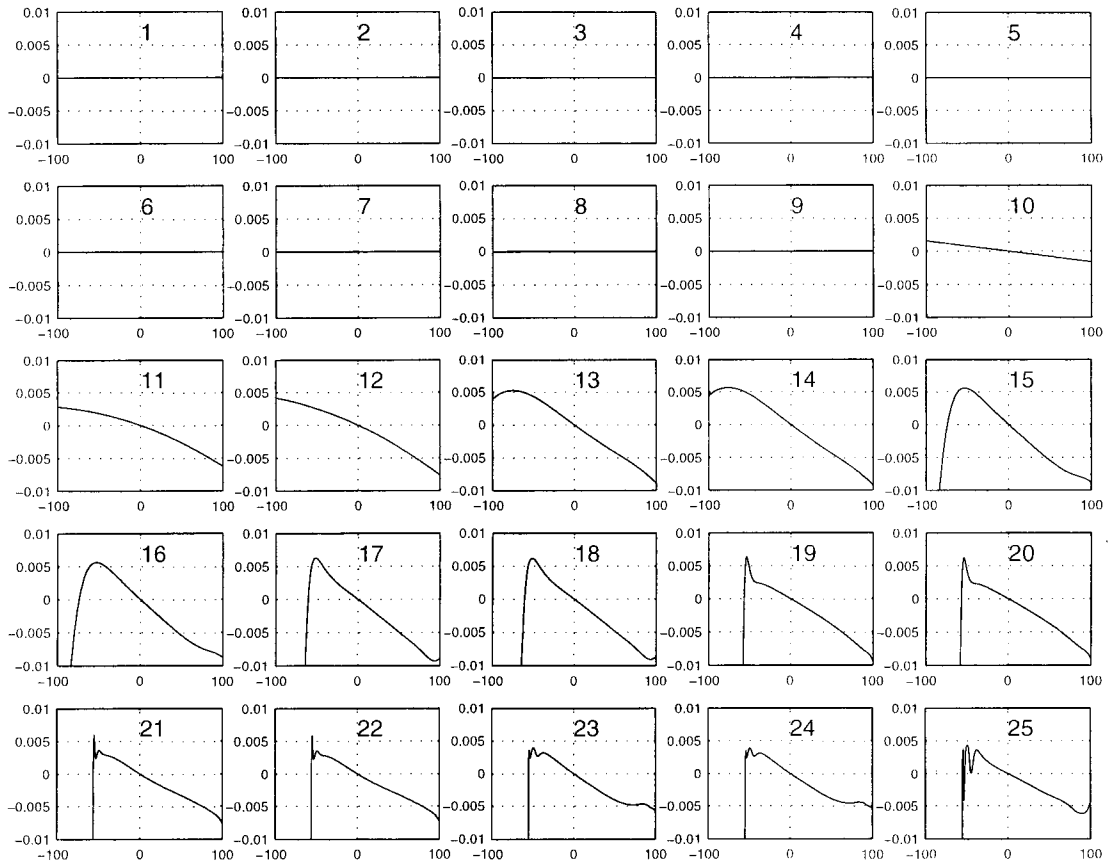

Figure 3.9: Two-Field-Sector magnet model: Dip5 deviation

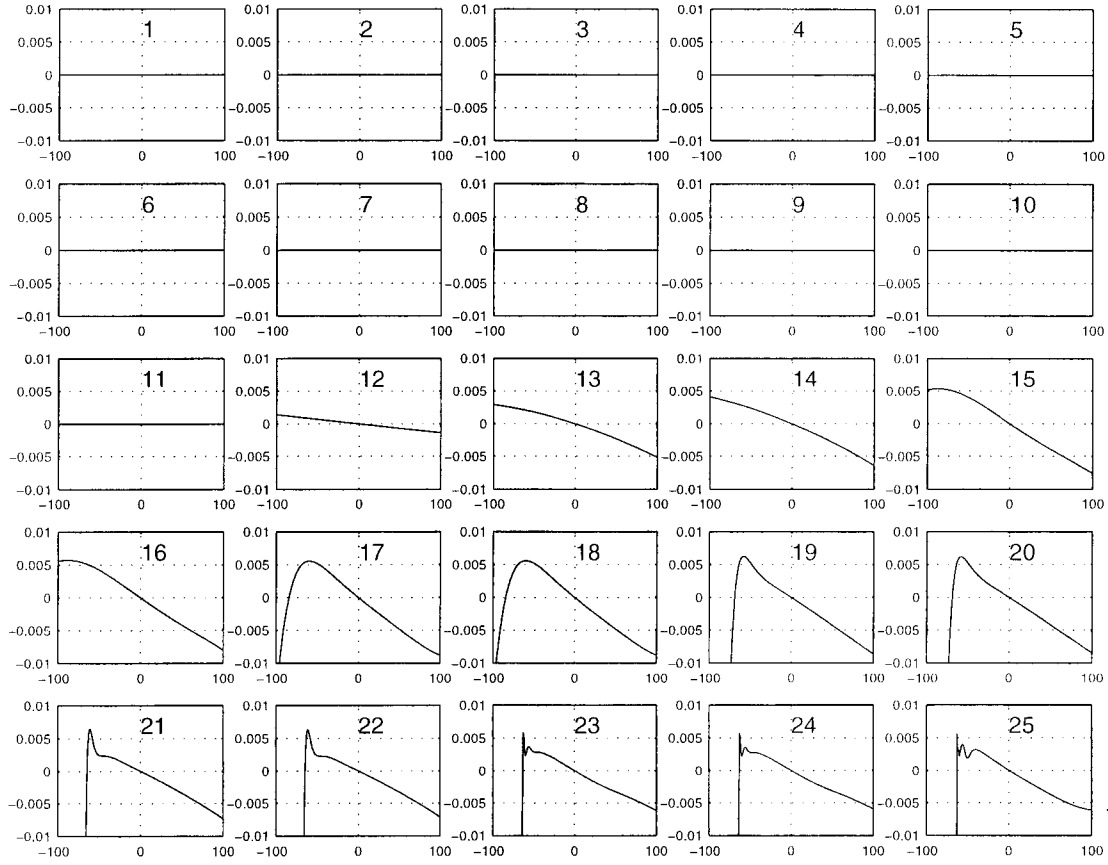

Figure 3.10: Two-Field-Sector magnet model: Dip6 deviation

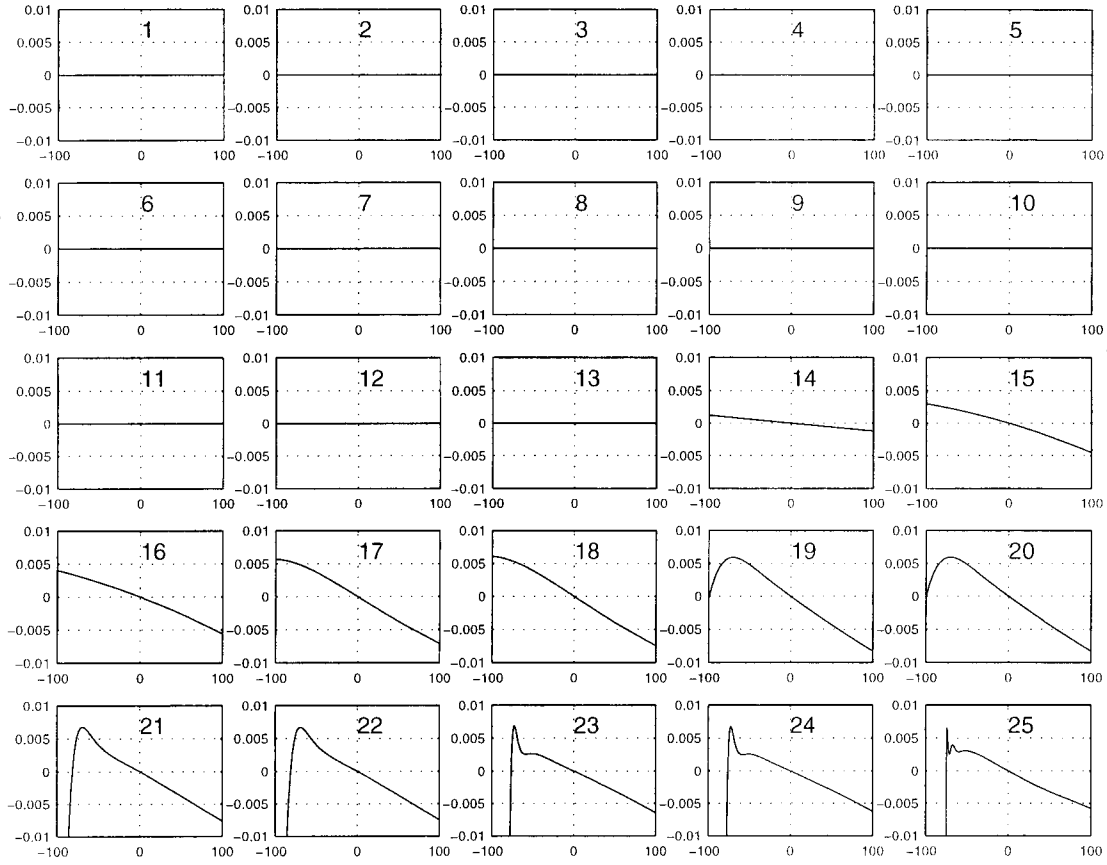

Figure 3.11: Two-Field-Sector magnet model: Dip7 deviation

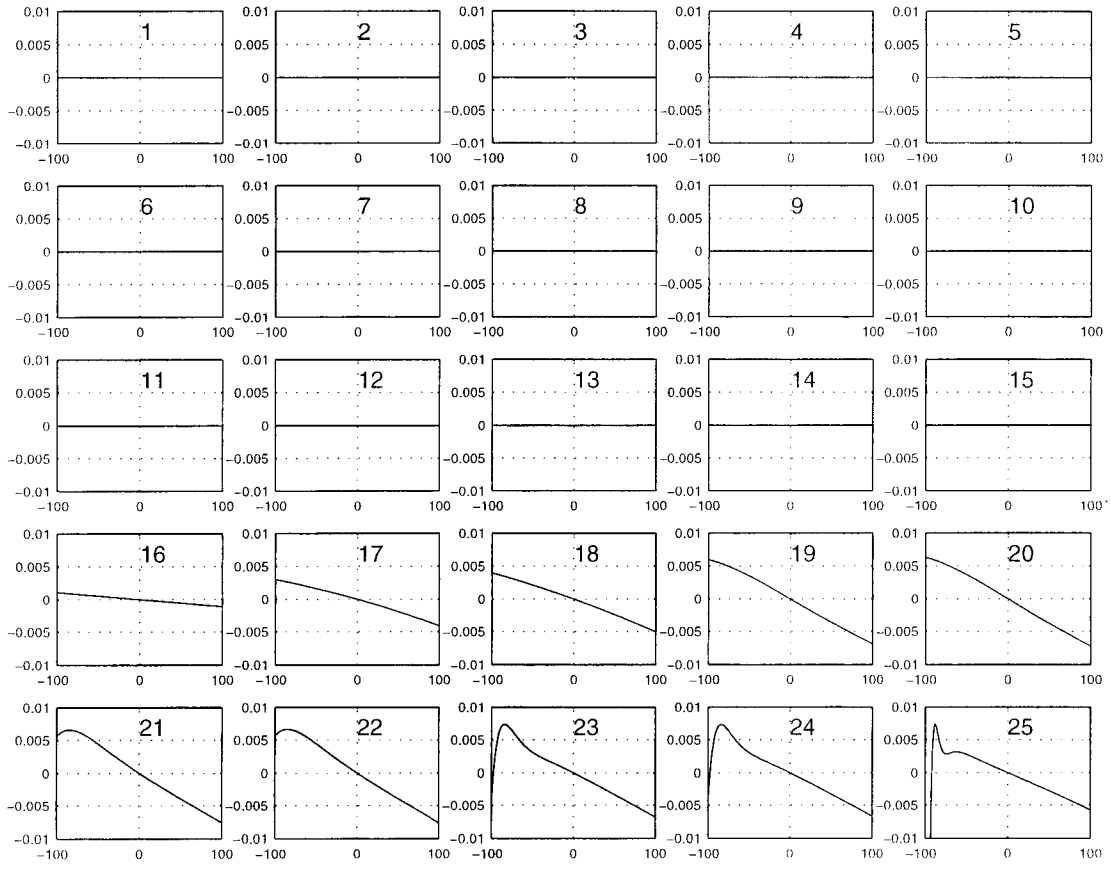

Figure 3.12: Two-Field-Sector magnet model: Dip8 deviation

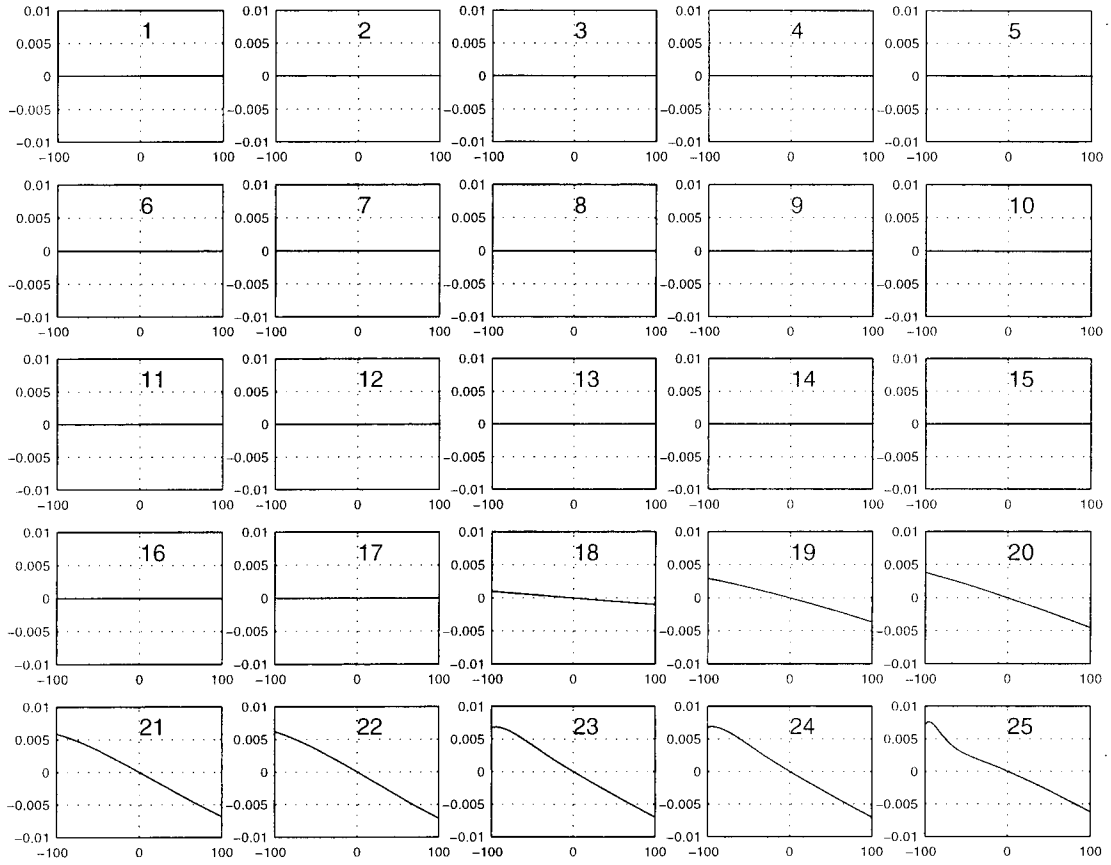

Figure 3.13: Two-Field-Sector magnet model: Dip9 deviation

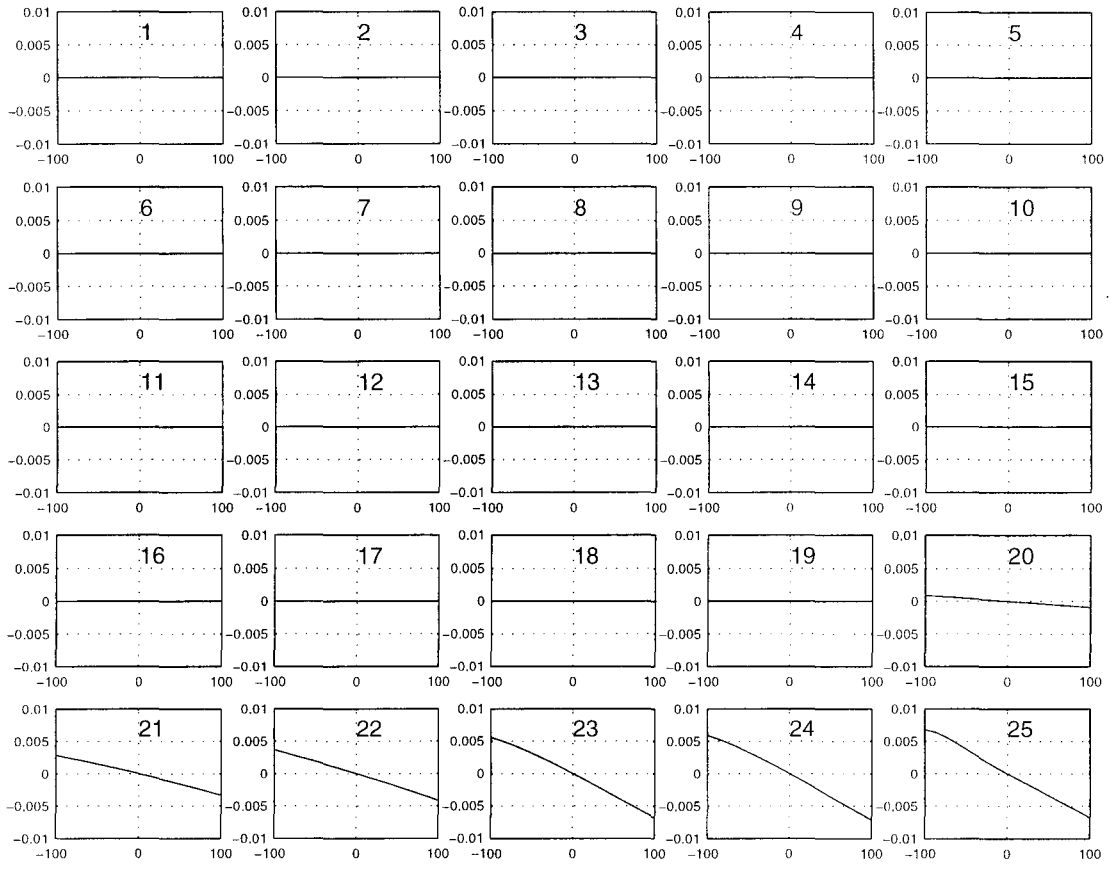

Figure 3.14: Two-Field-Sector magnet model: Dip10 deviation

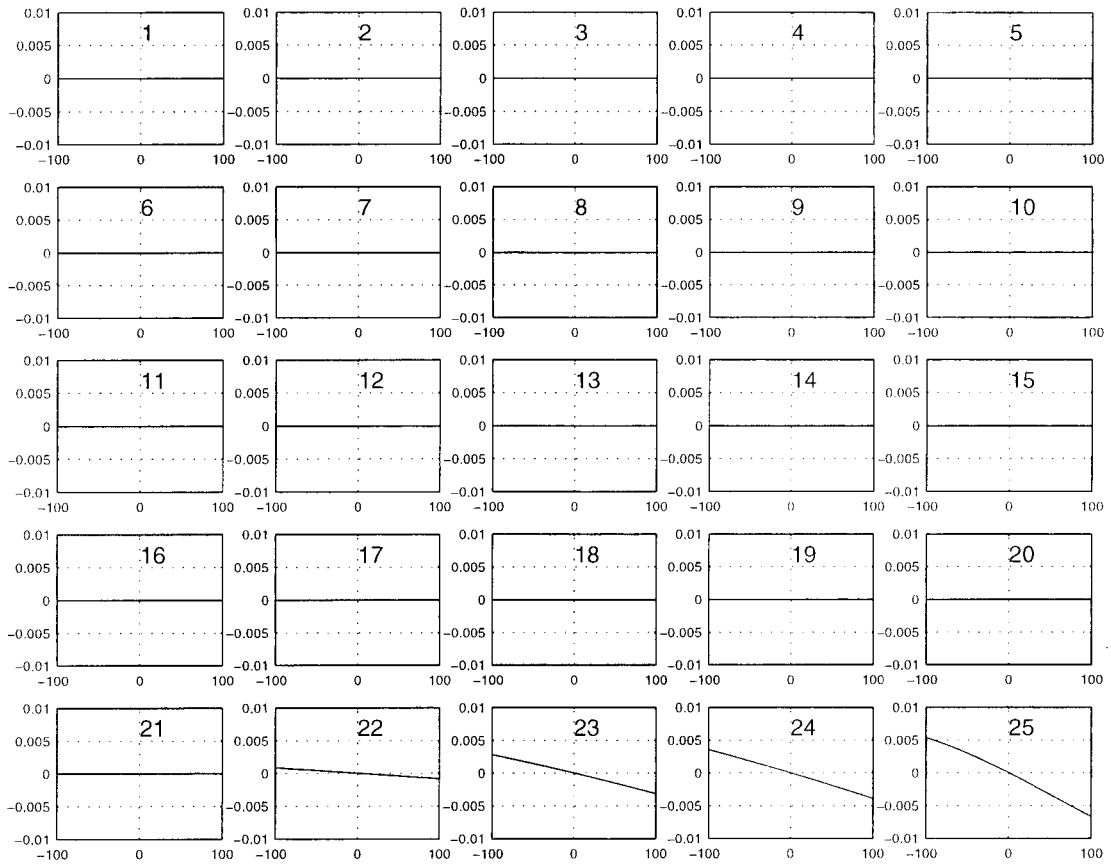

Figure 3.15: Two-Field-Sector magnet model: Dip11 deviation

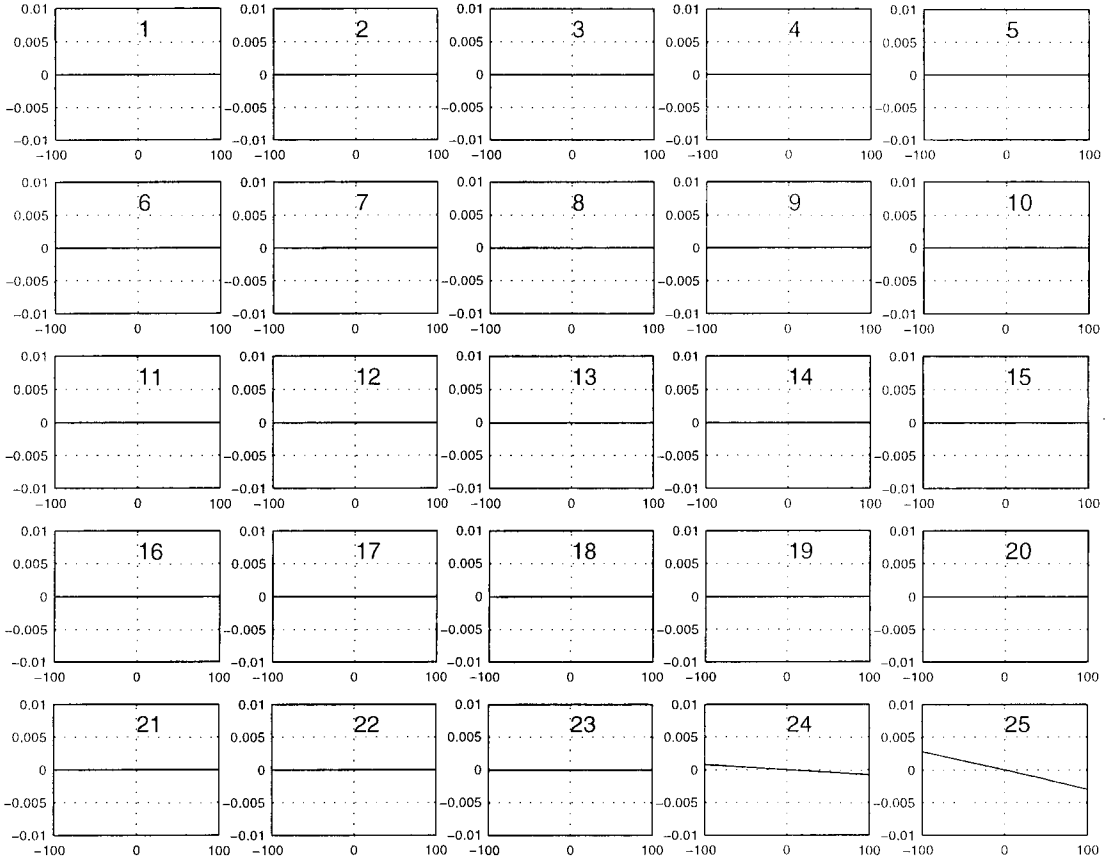

Figure 3.16: Two-Field-Sector magnet model: Dip12 deviation

4 Response plots of adjusted homogeneous magnet model

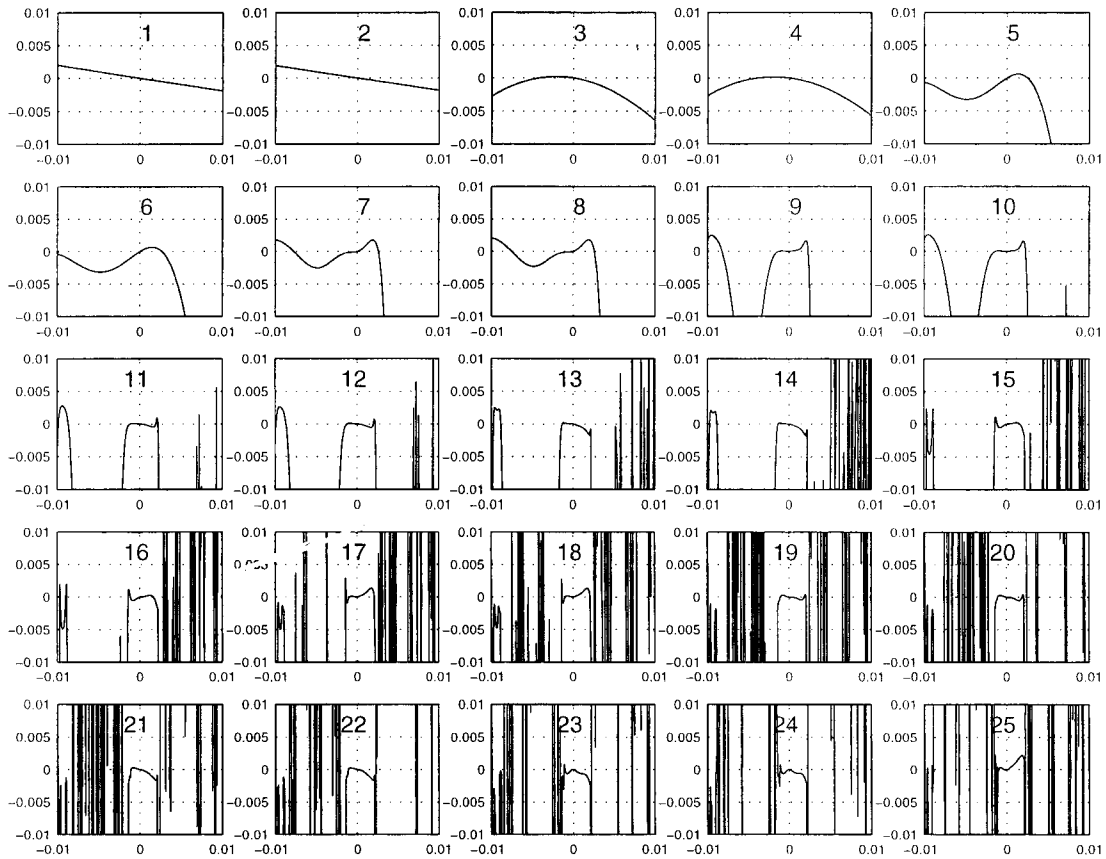

Figure 4.1: Adjusted Homogeneous magnet model: M deviation

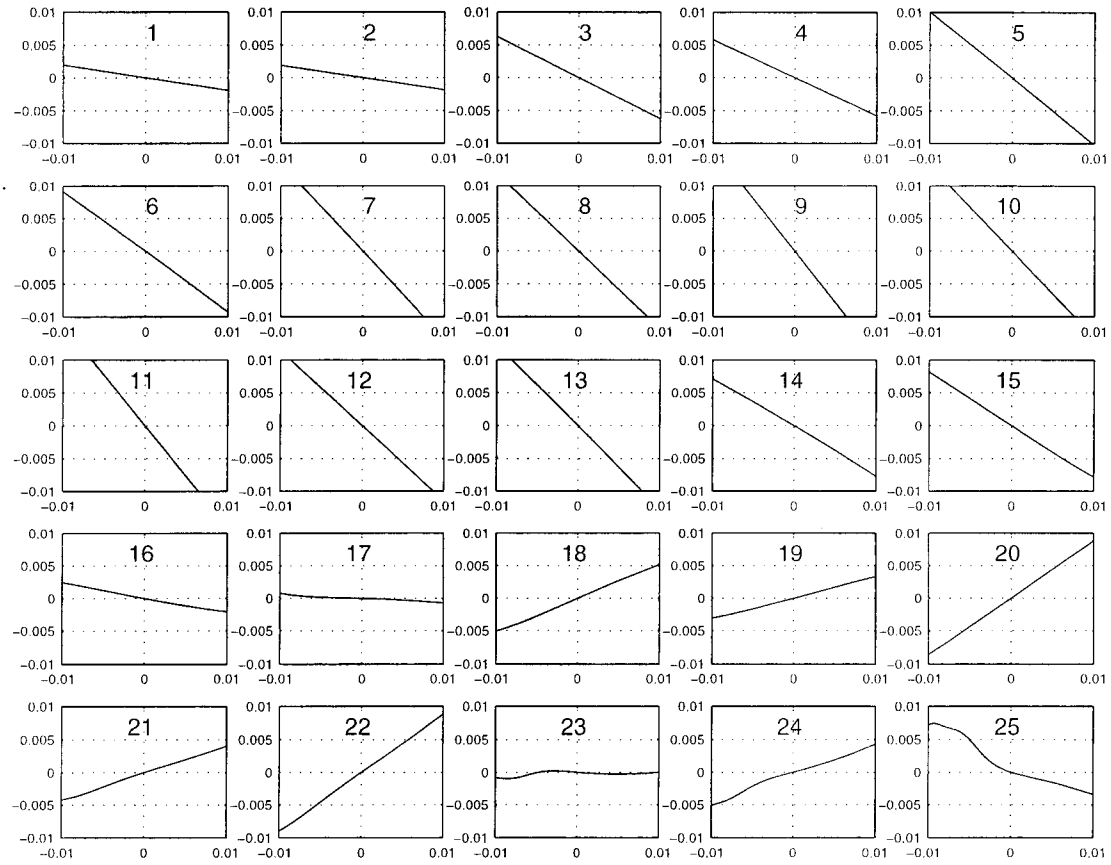

Figure 4.2: Adjusted Homogeneous magnet model: D deviation

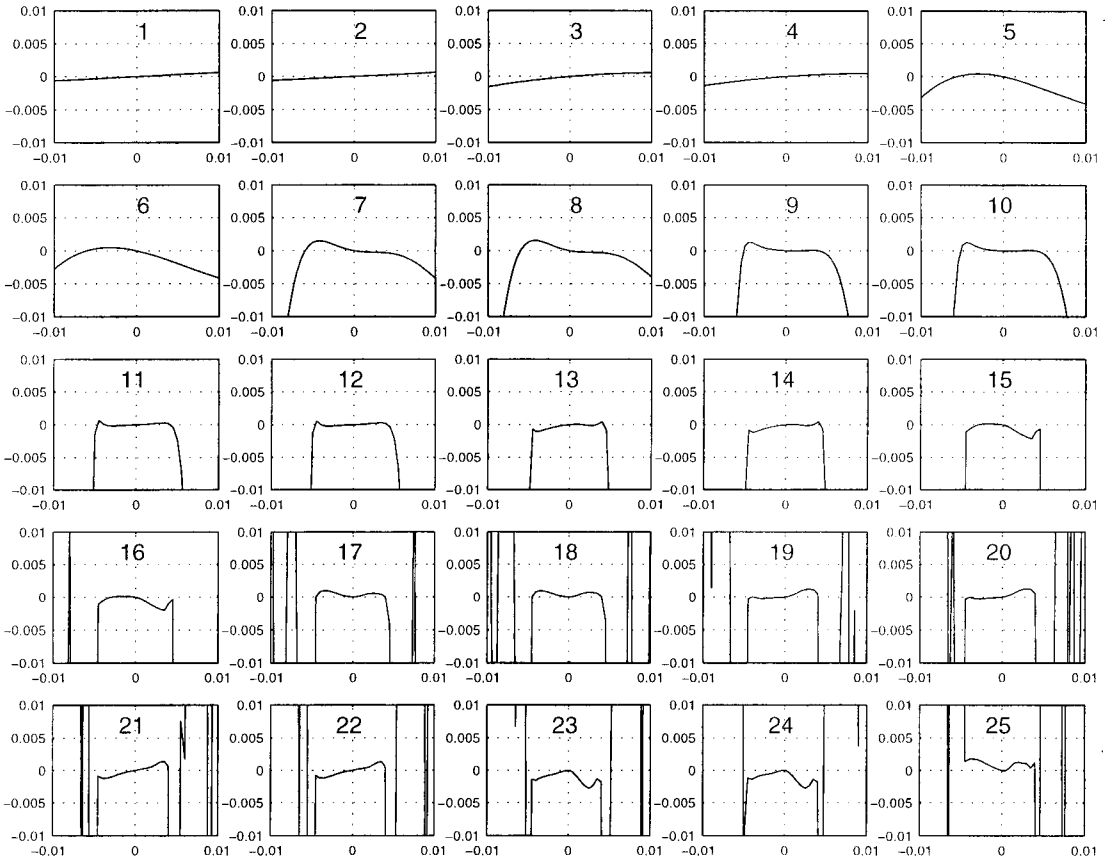

Figure 4.3: Adjusted Homogeneous magnet model: E deviation

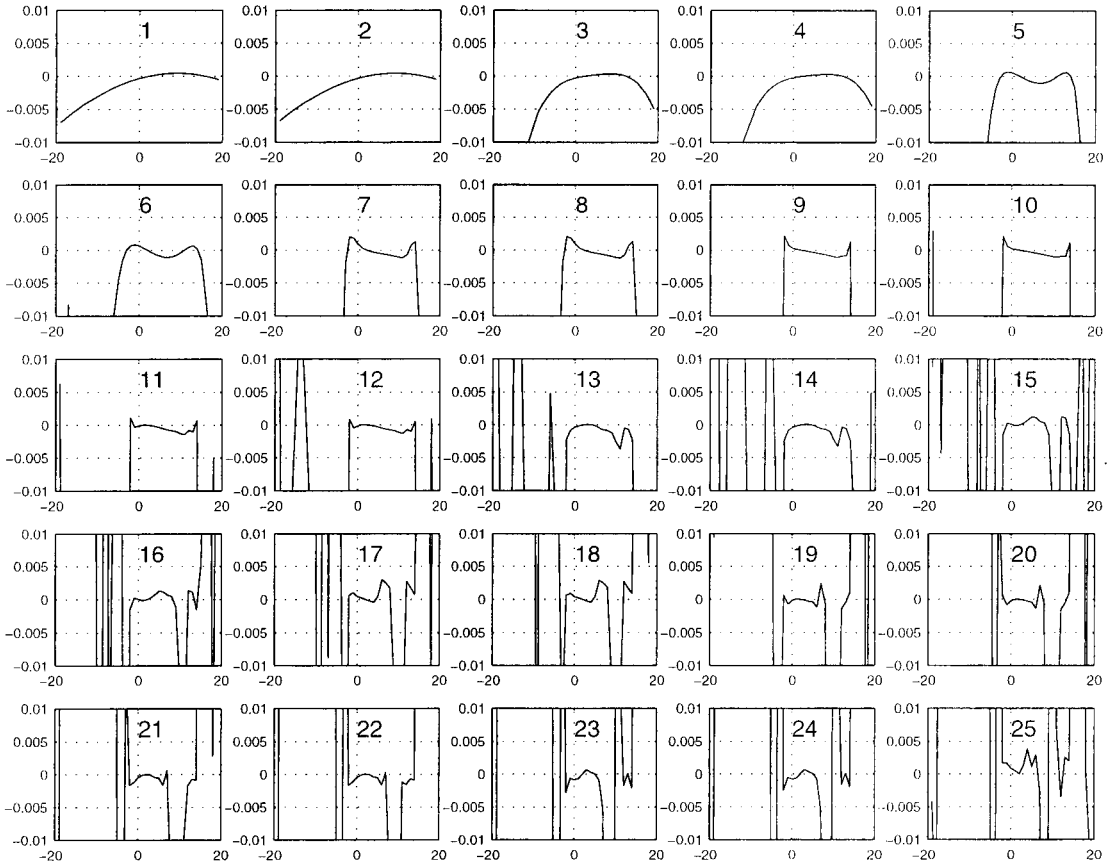

Figure 4.4: Adjusted Homogeneous magnet model: P deviation

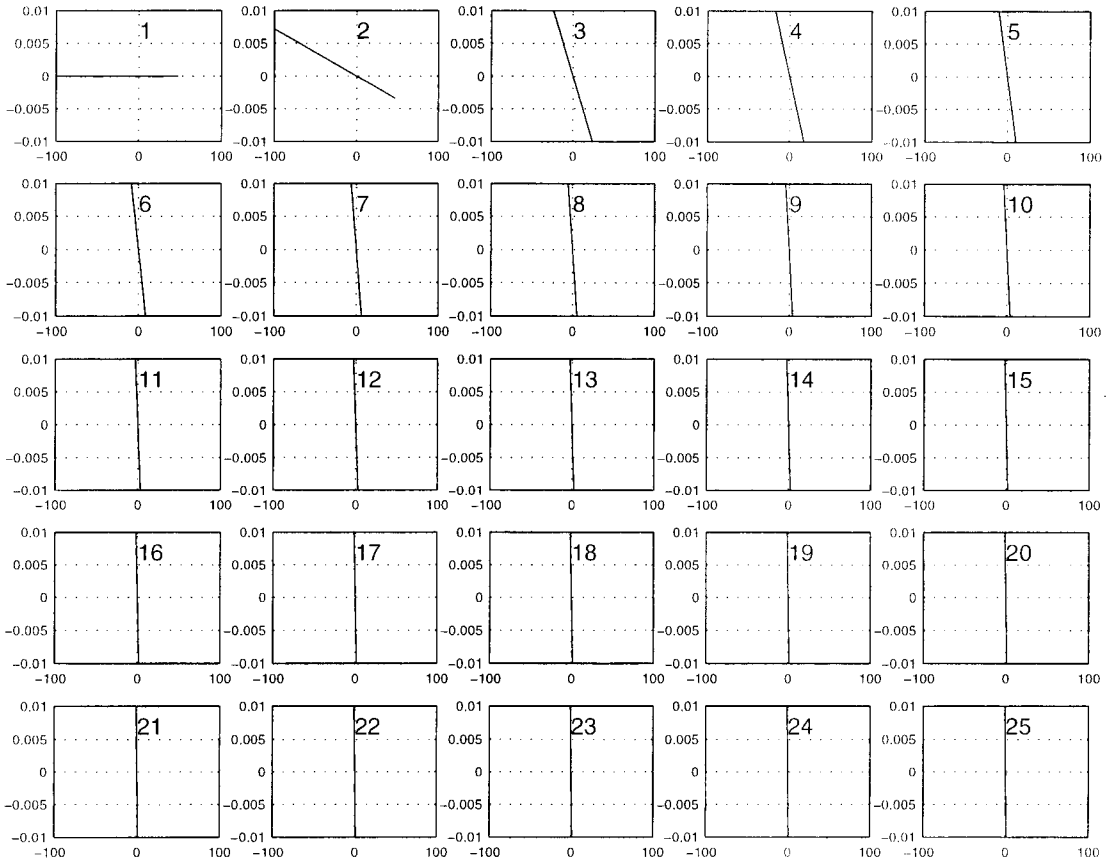

Figure 4.5: Adjusted Homogeneous magnet model: Dip1 deviation

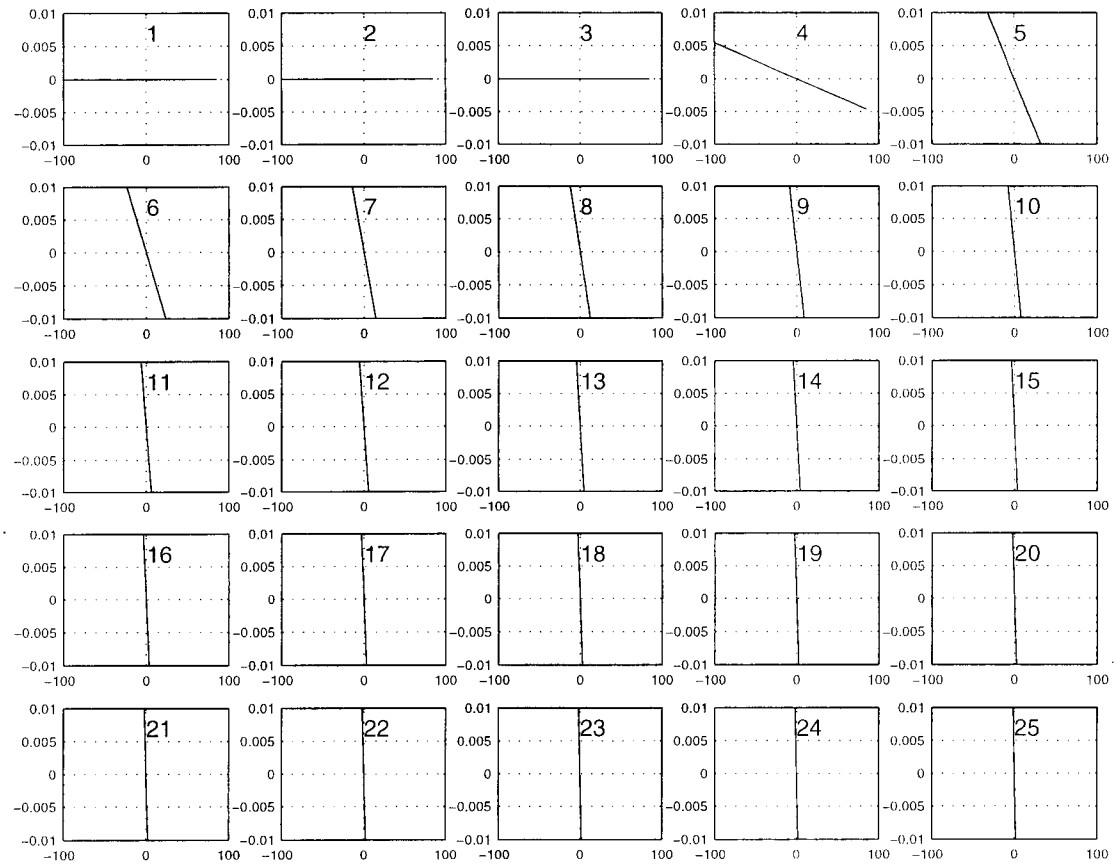

Figure 4.6: Adjusted Homogeneous magnet model: Dip2 deviation

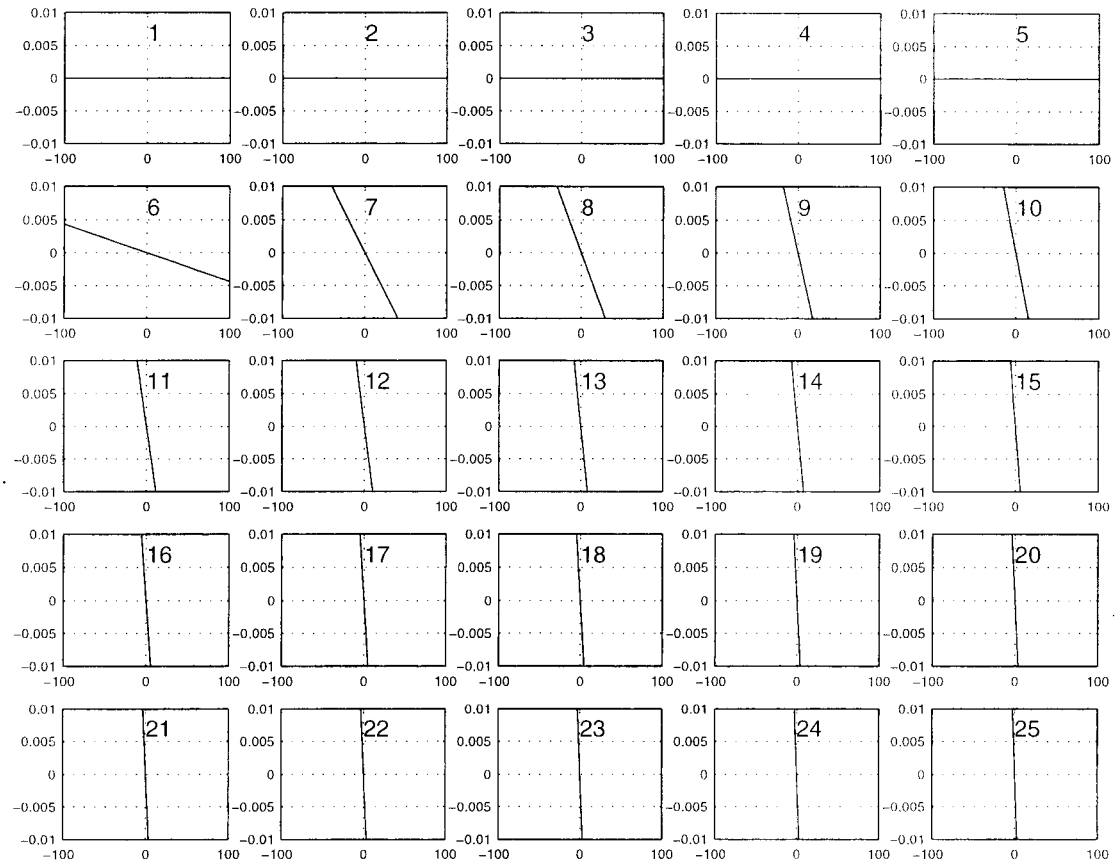

Figure 4.7: Adjusted Homogeneous magnet model: Dip3 deviation

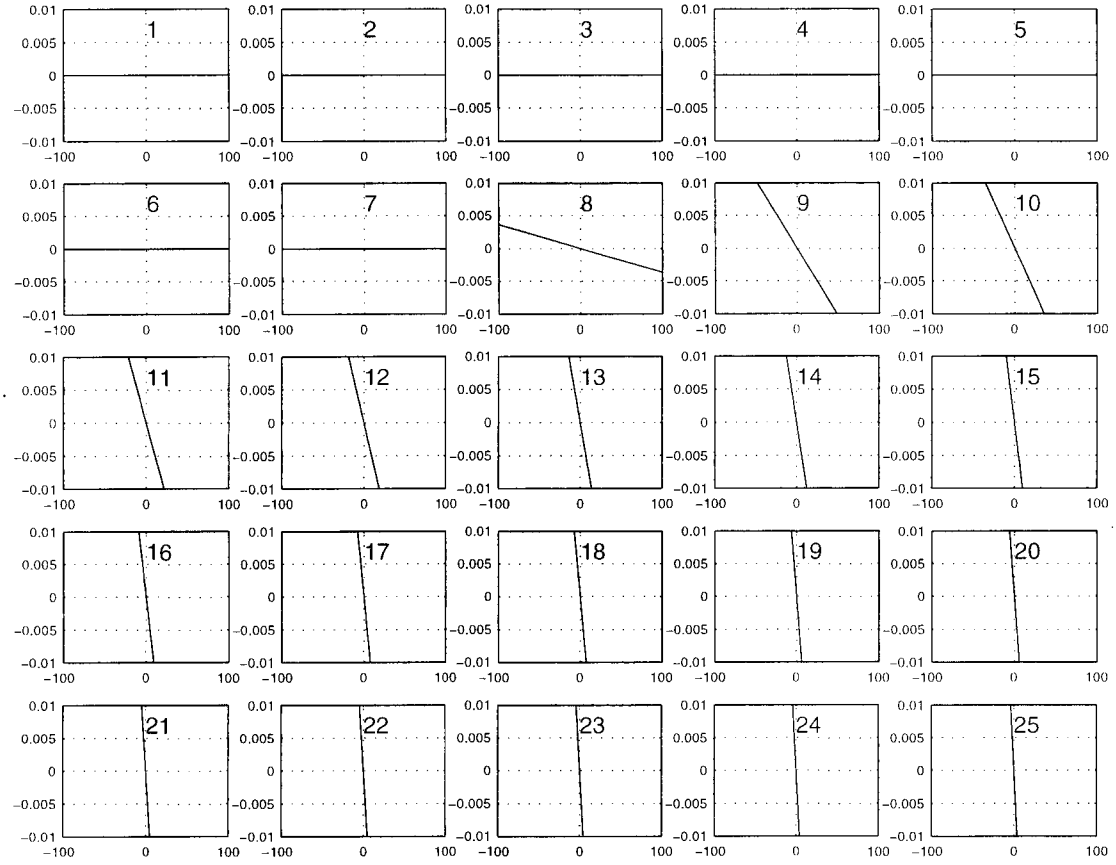

Figure 4.8: Adjusted Homogeneous magnet model: Dip4 deviation

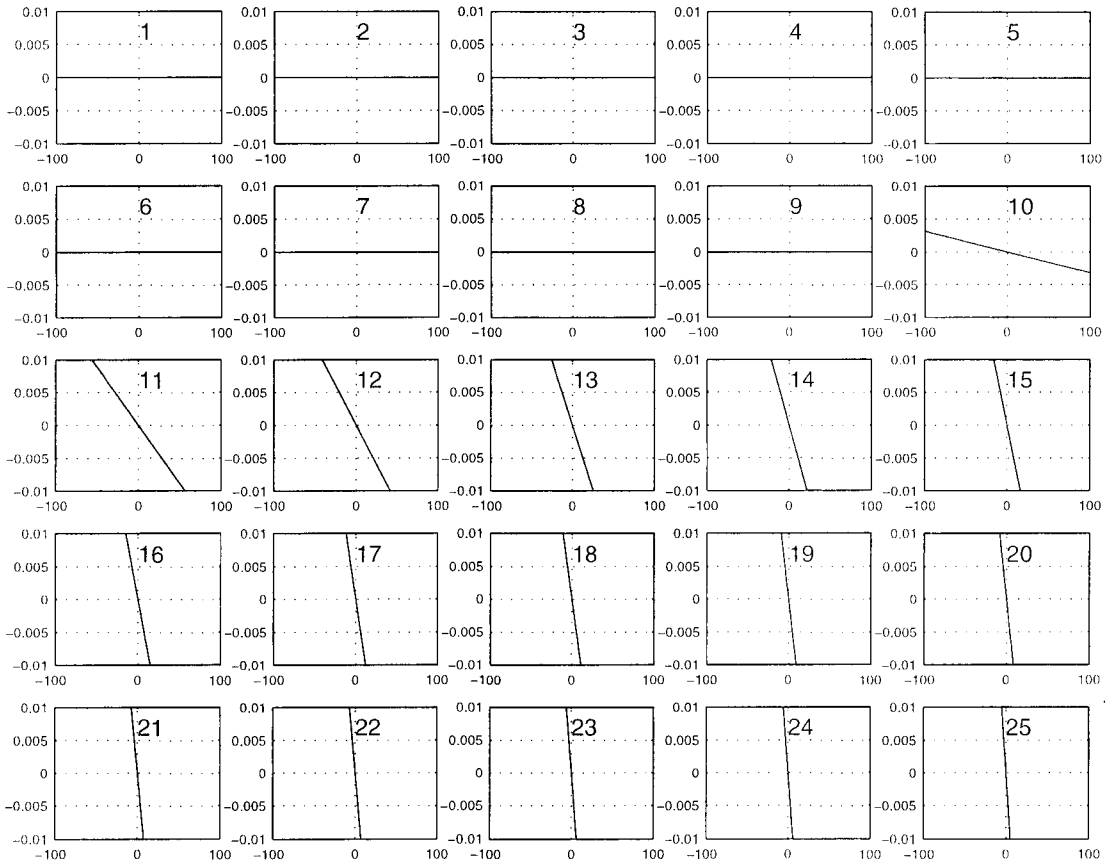

Figure 4.9: Adjusted Homogeneous magnet model: Dip5 deviation

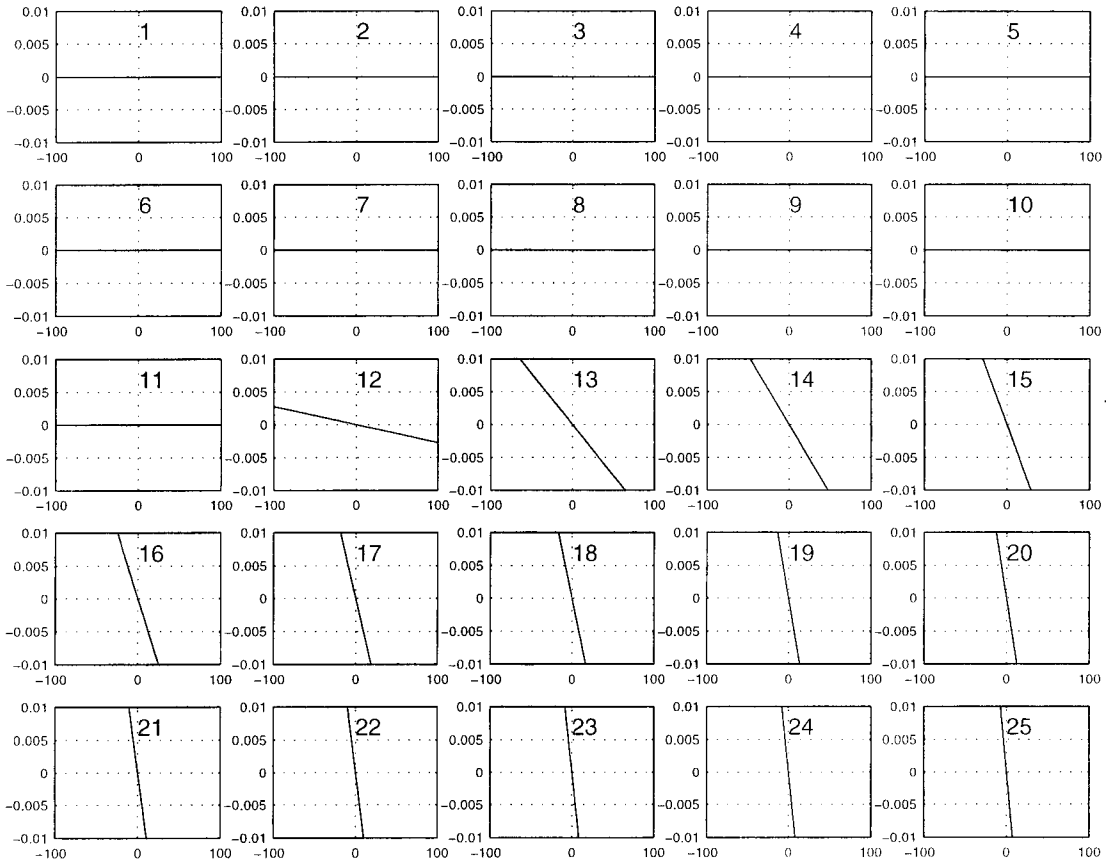

Figure 4.10: Adjusted Homogeneous magnet model: Dip6 deviation

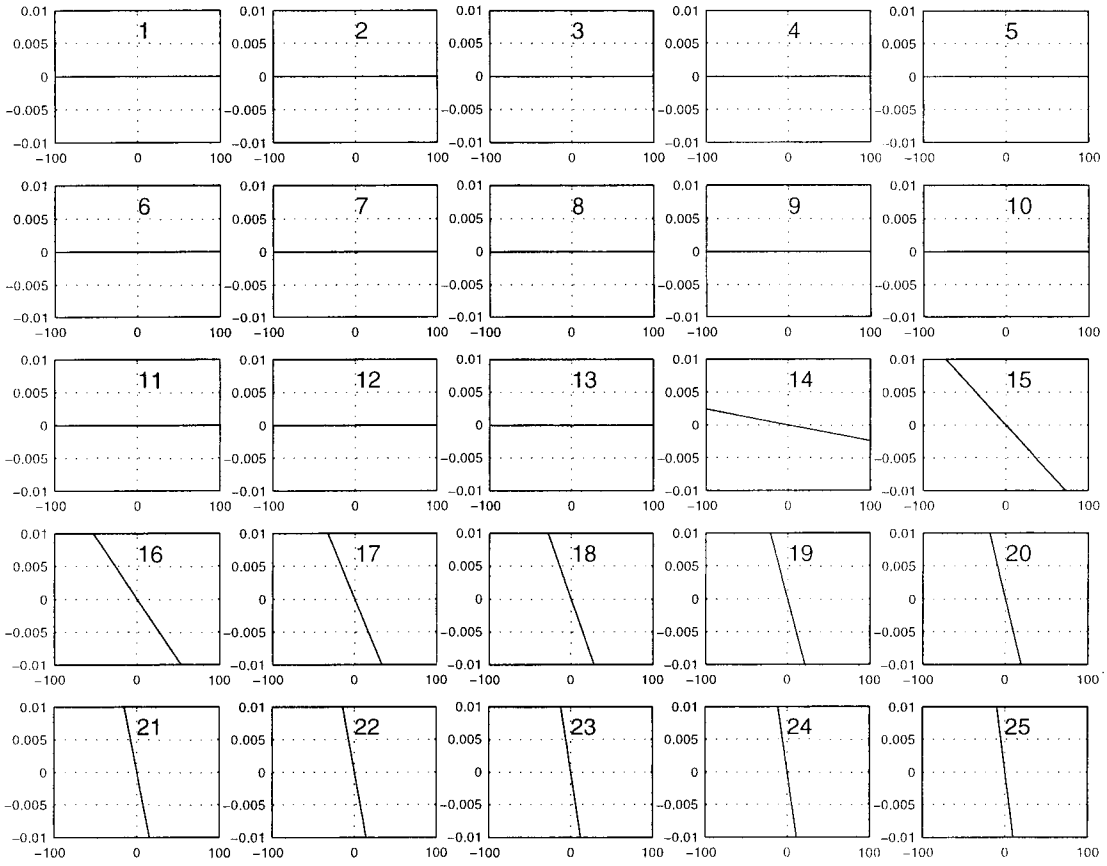

Figure 4.11: Adjusted Homogeneous magnet model: Dip7 deviation

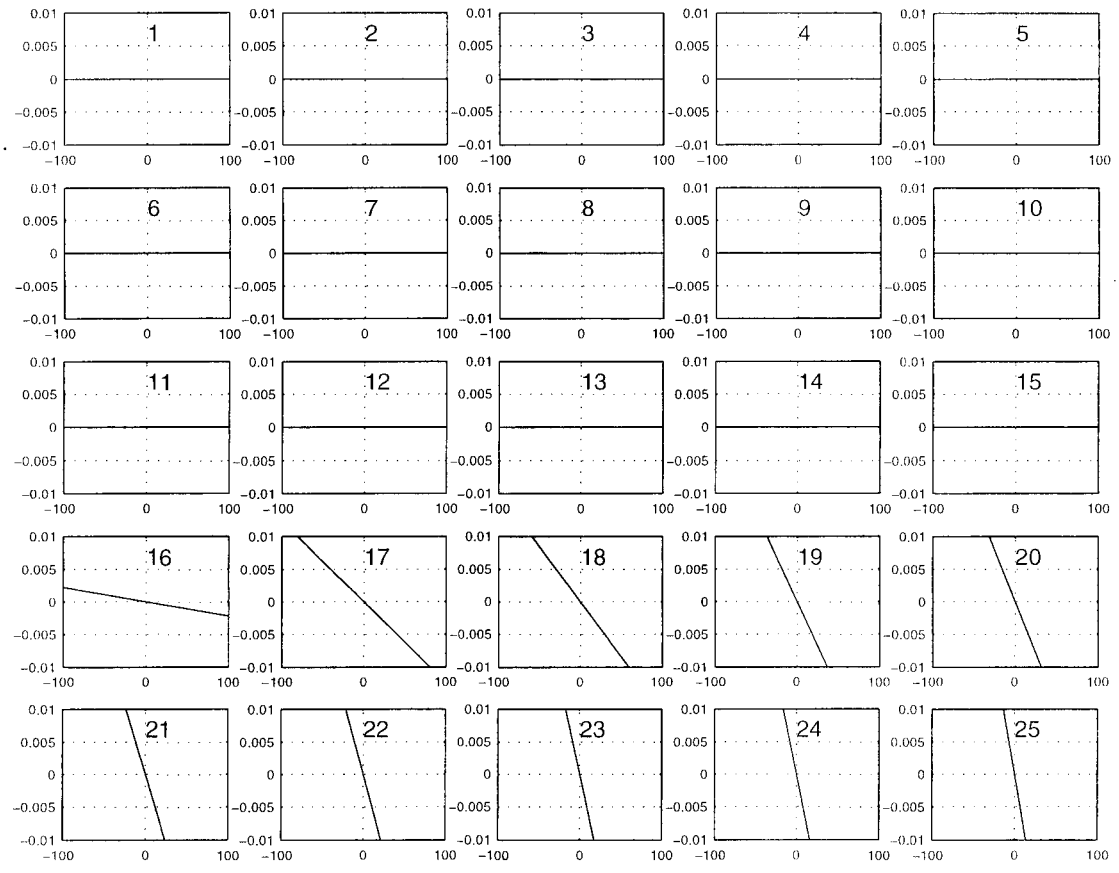

Figure 4.12: Adjusted Homogeneous magnet model: Dip8 deviation

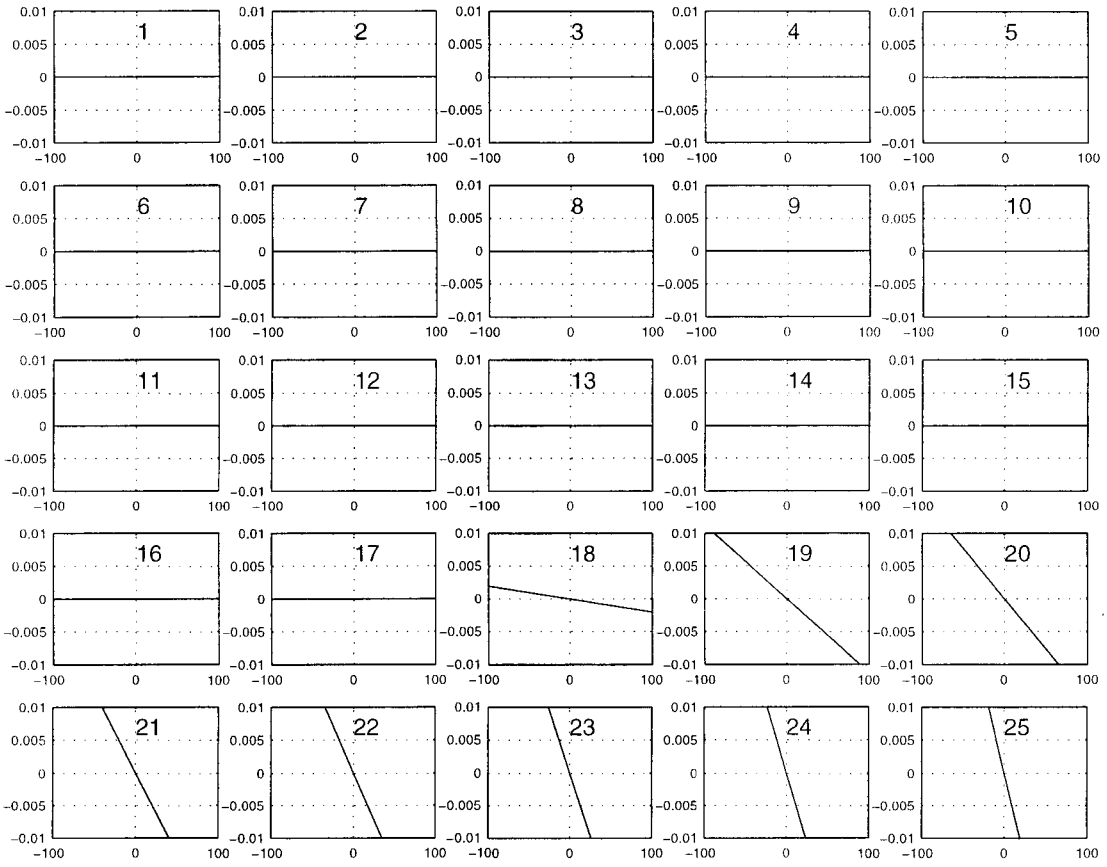

Figure 4.13: Adjusted Homogeneous magnet model: Dip9 deviation

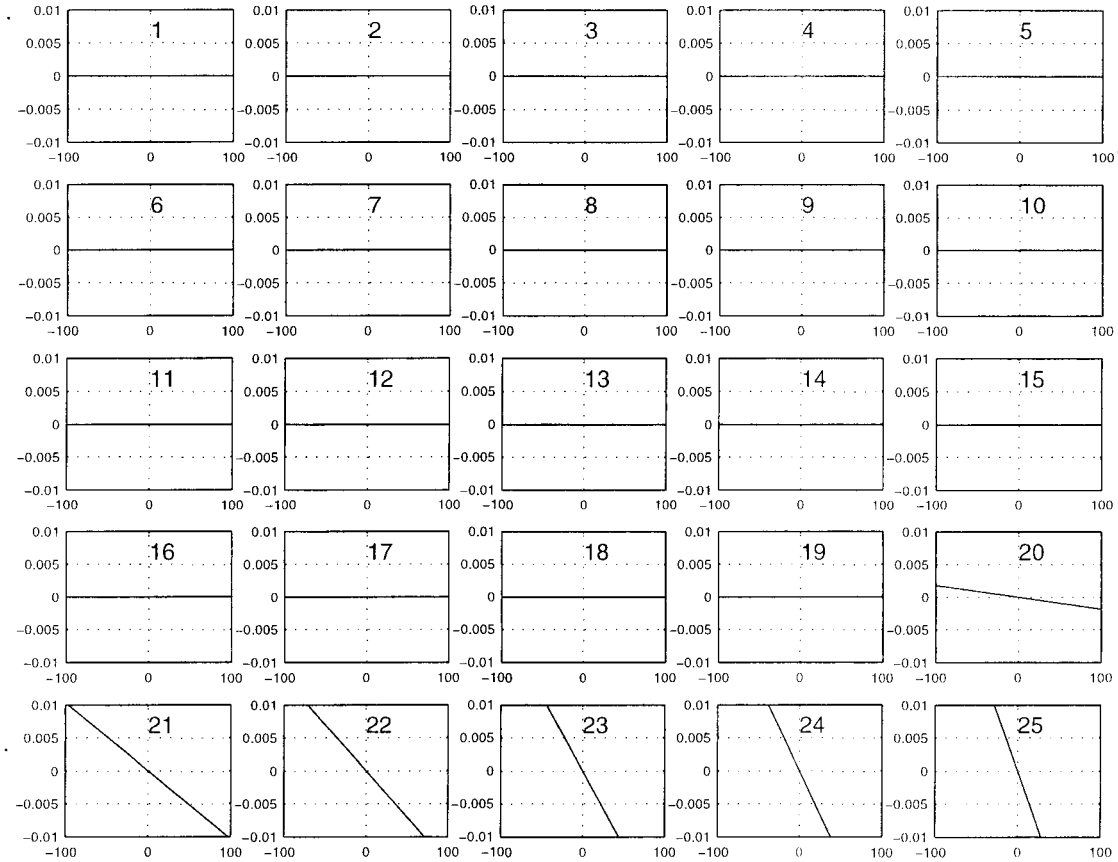

Figure 4.14: Adjusted Homogeneous magnet model: Dip10 deviation

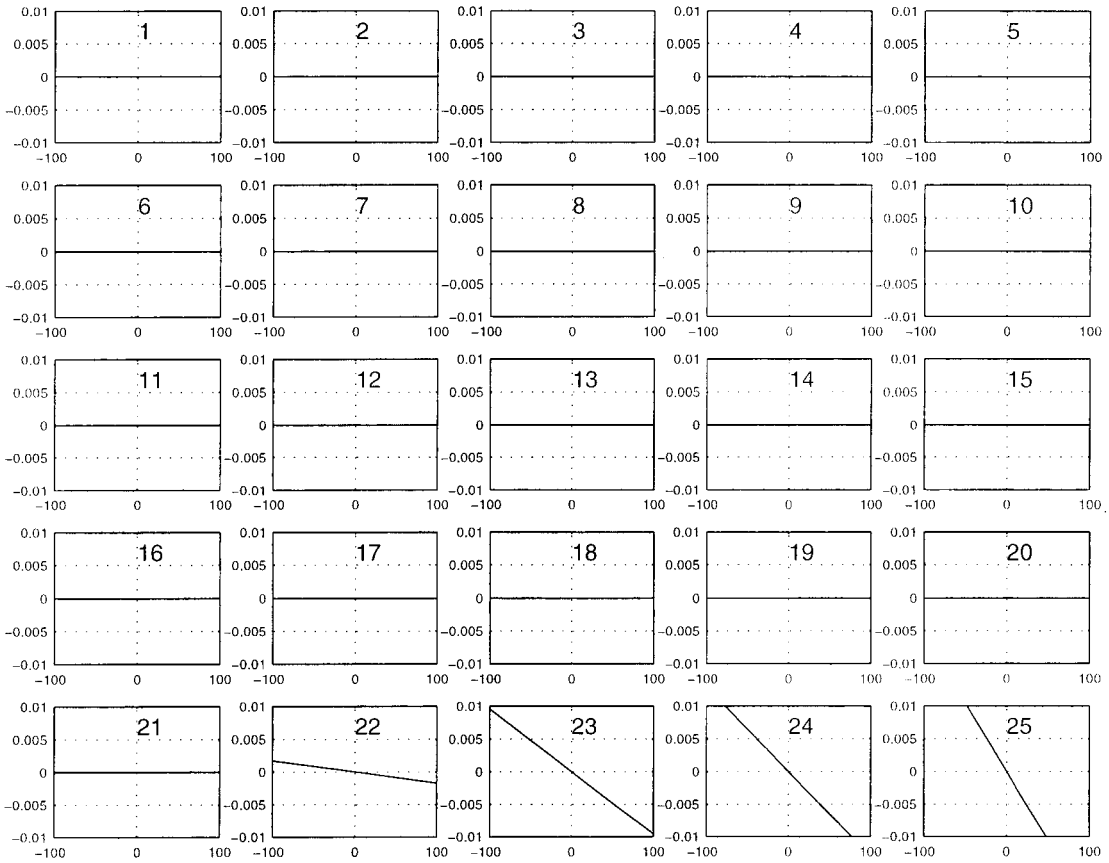

Figure 4.15: Adjusted Homogeneous magnet model: Dip11 deviation

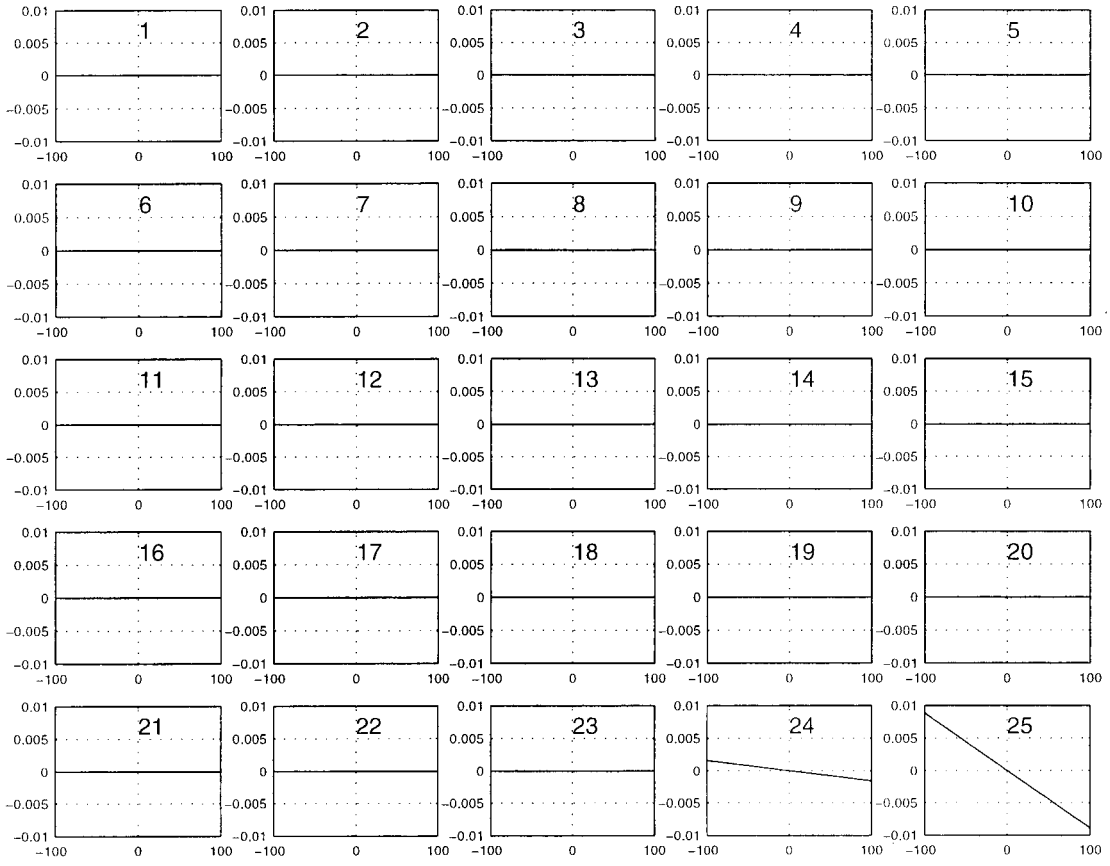

Figure 4.16: Adjusted Homogeneous magnet model: Dip12 deviation

5 Response plots of adjusted two-field-sector magnet model

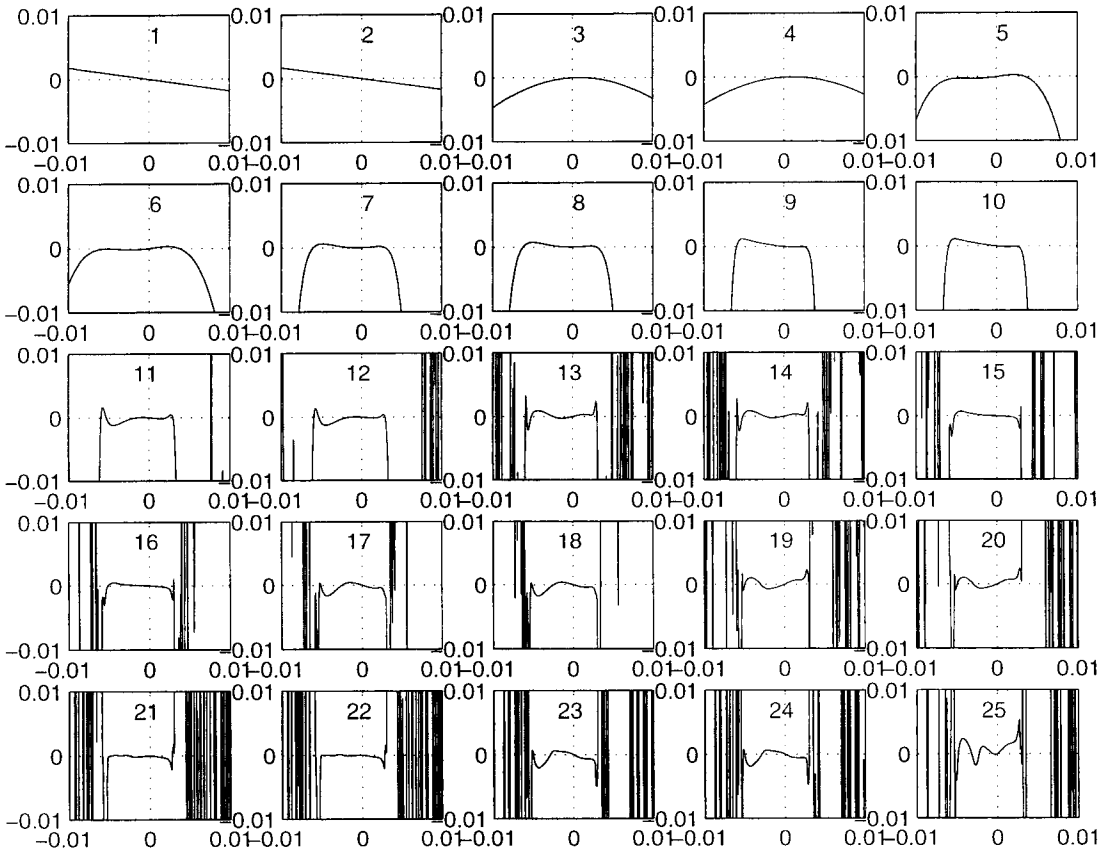

Figure 5.1: Adjusted Two-Field-Sector magnet model: M deviation

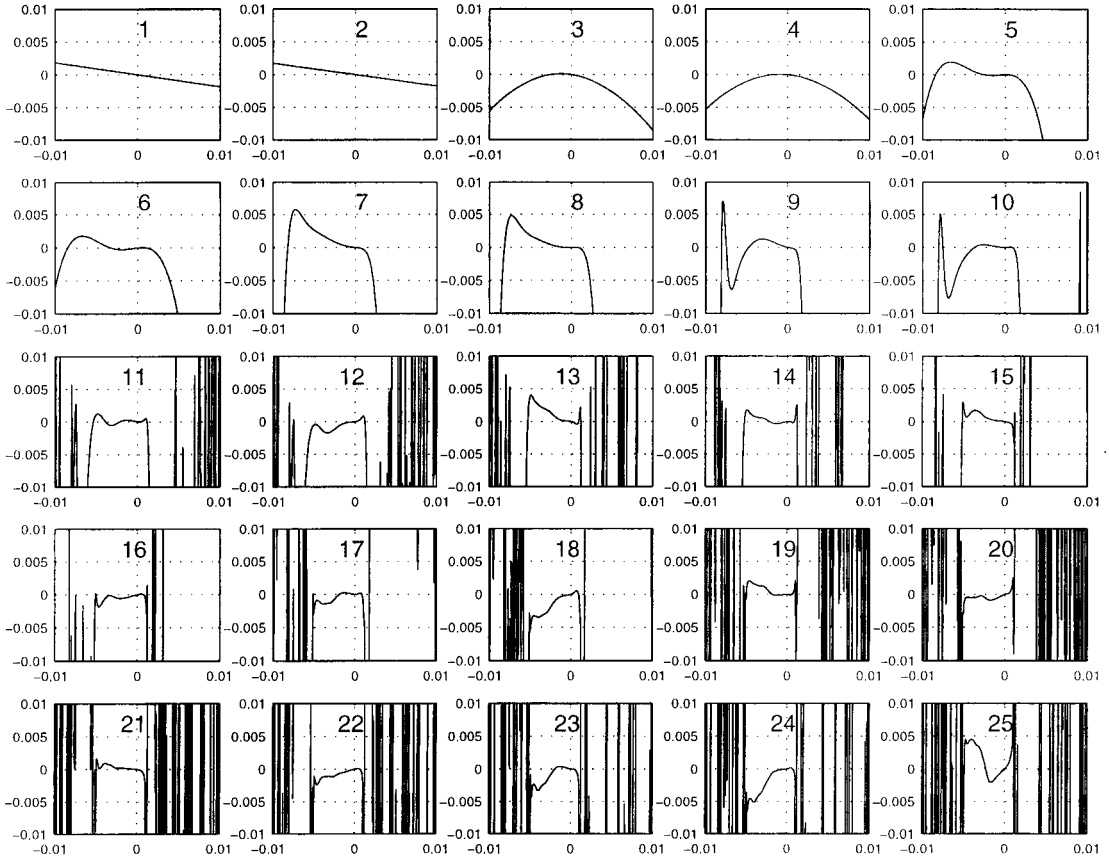

Figure 5.2: Adjusted Two-Field-Sector magnet model: D deviation

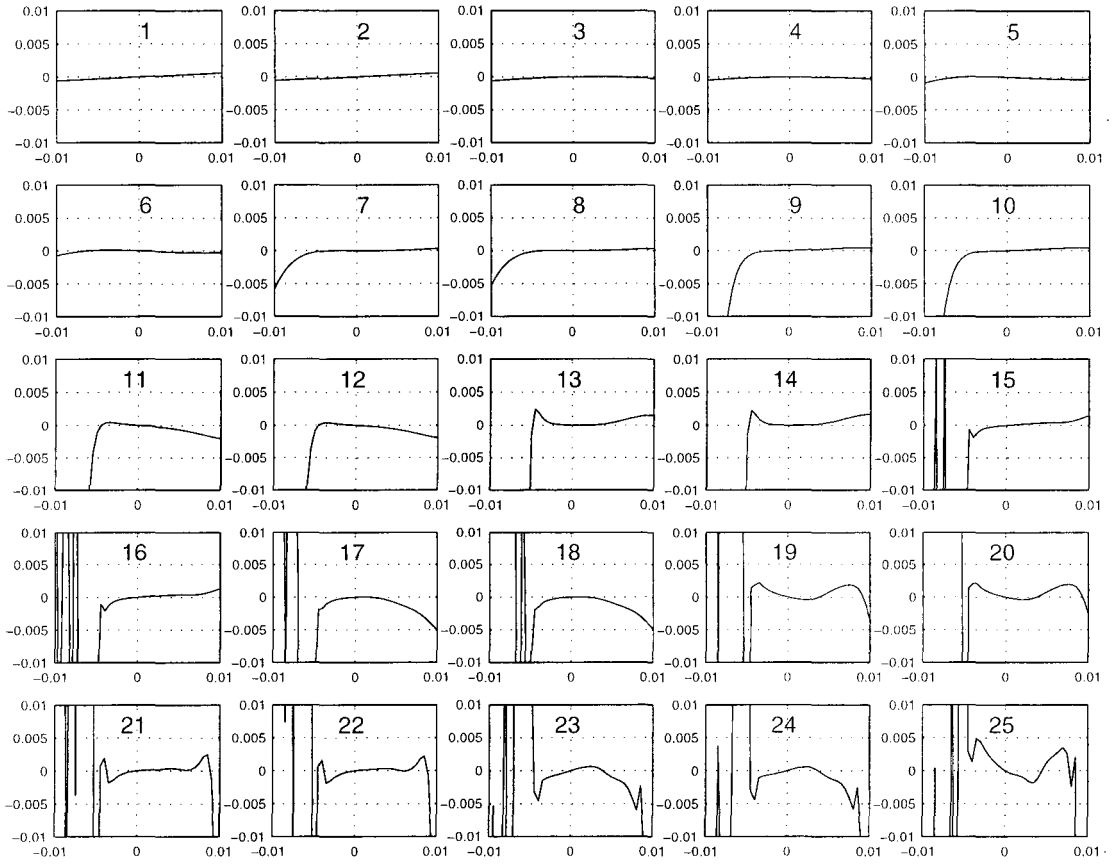

Figure 5.3: Adjusted Two-Field-Sector magnet model: E deviation

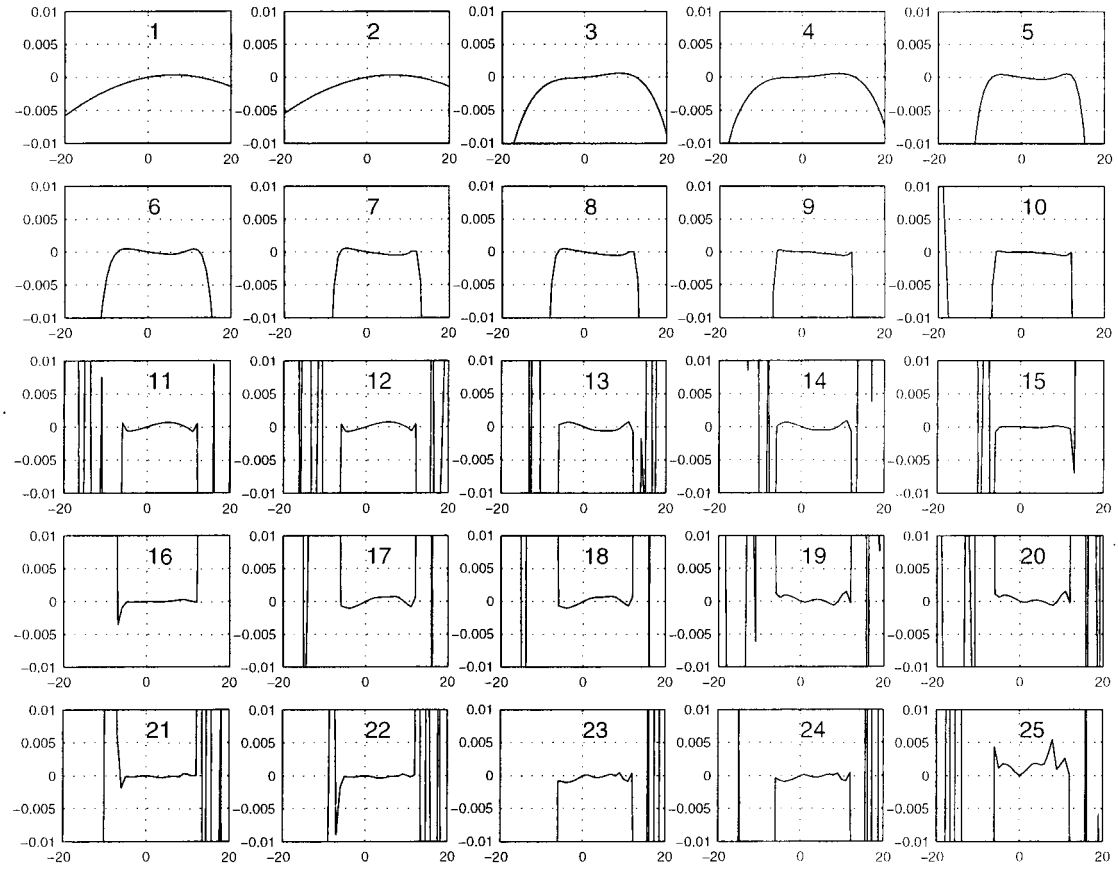

Figure 5.4: Adjusted Two-Field-Sector magnet model: P deviation

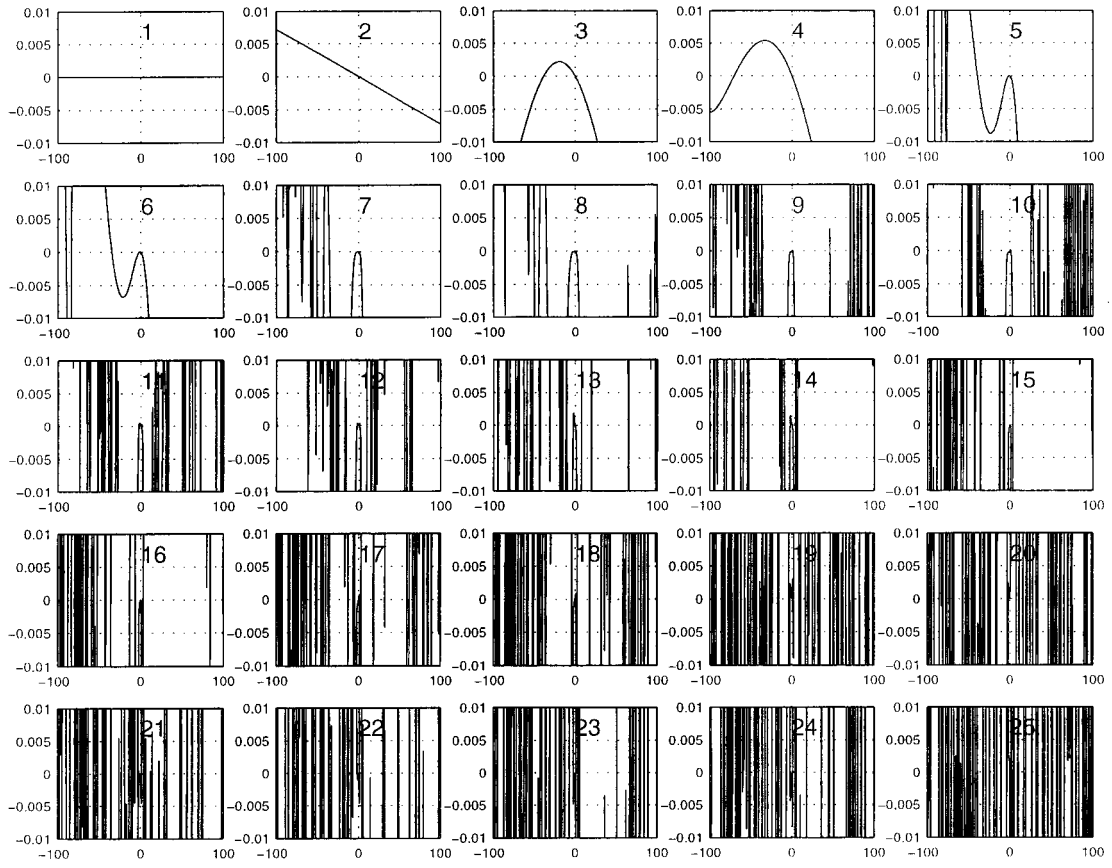

Figure 5.5: Adjusted Two-Field-Sector magnet model: Dip1 deviation

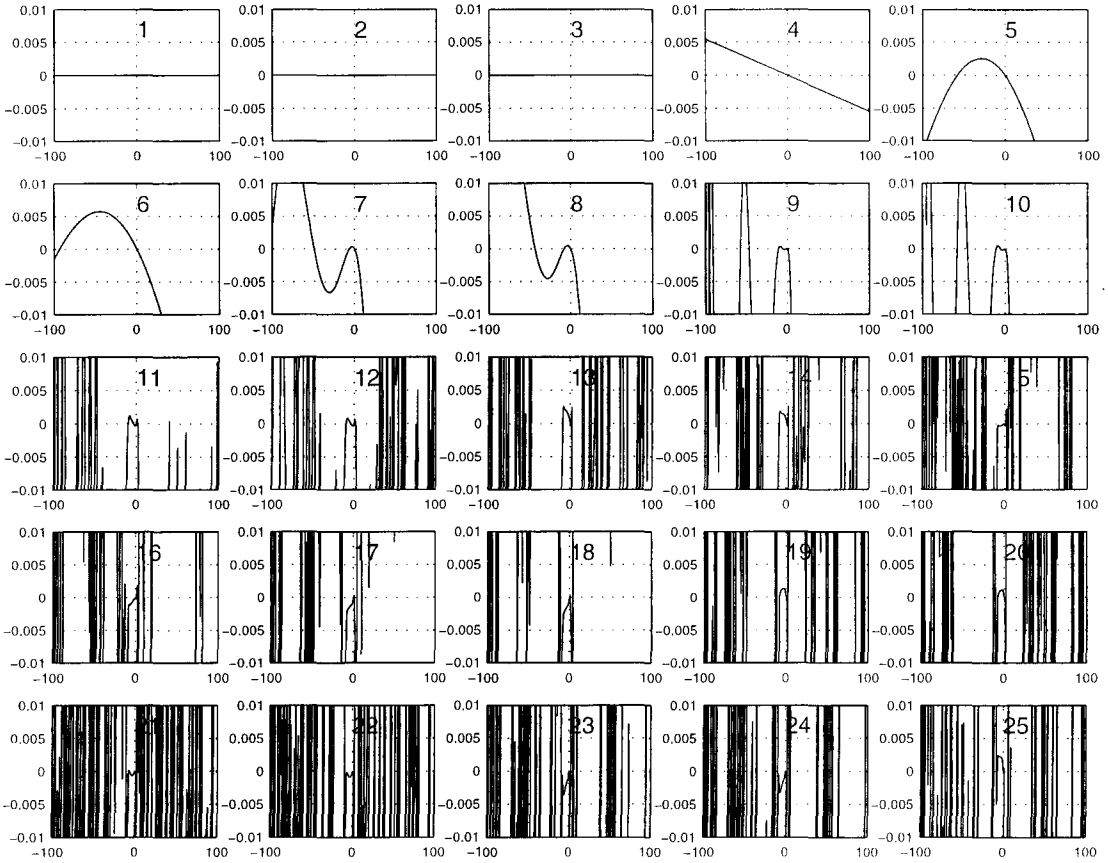

Figure 5.6: Adjusted Two-Field-Sector magnet model: Dip2 deviation

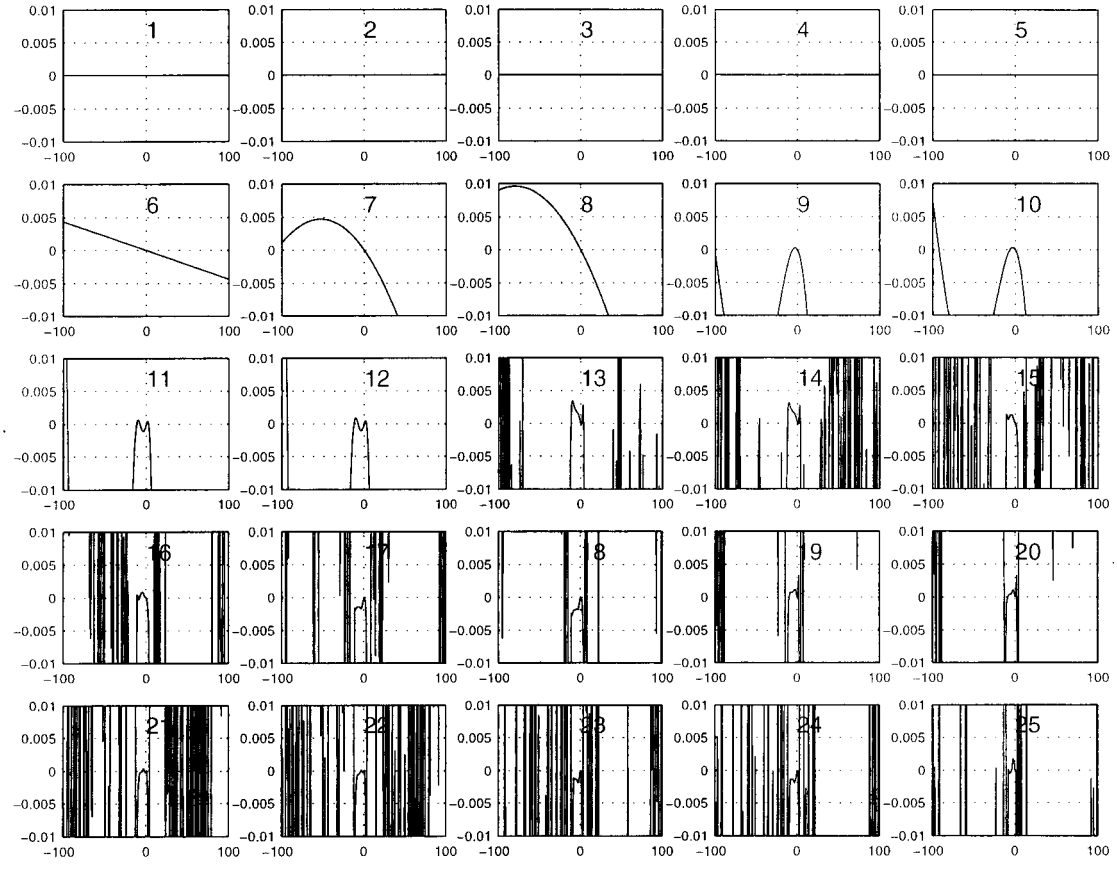

Figure 5.7: Adjusted Two-Field-Sector magnet model: Dip3 deviation

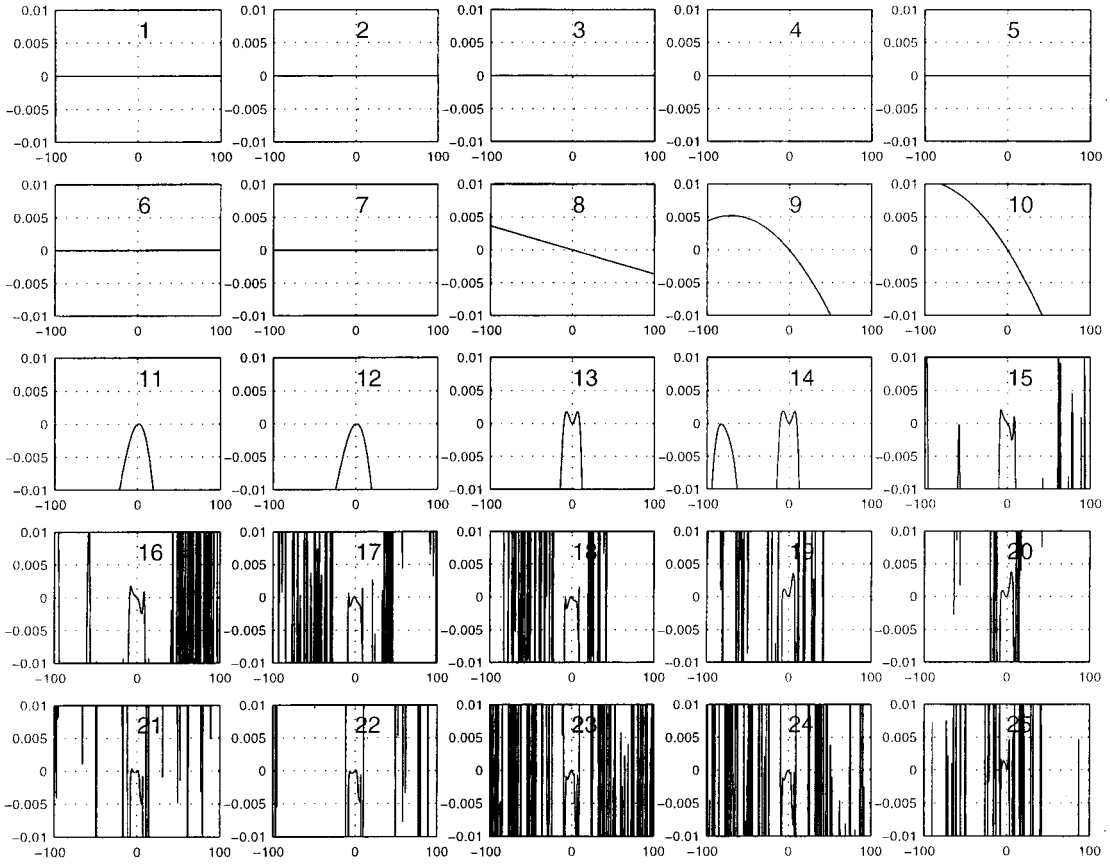

Figure 5.8: Adjusted Two-Field-Sector magnet model: Dip4 deviation

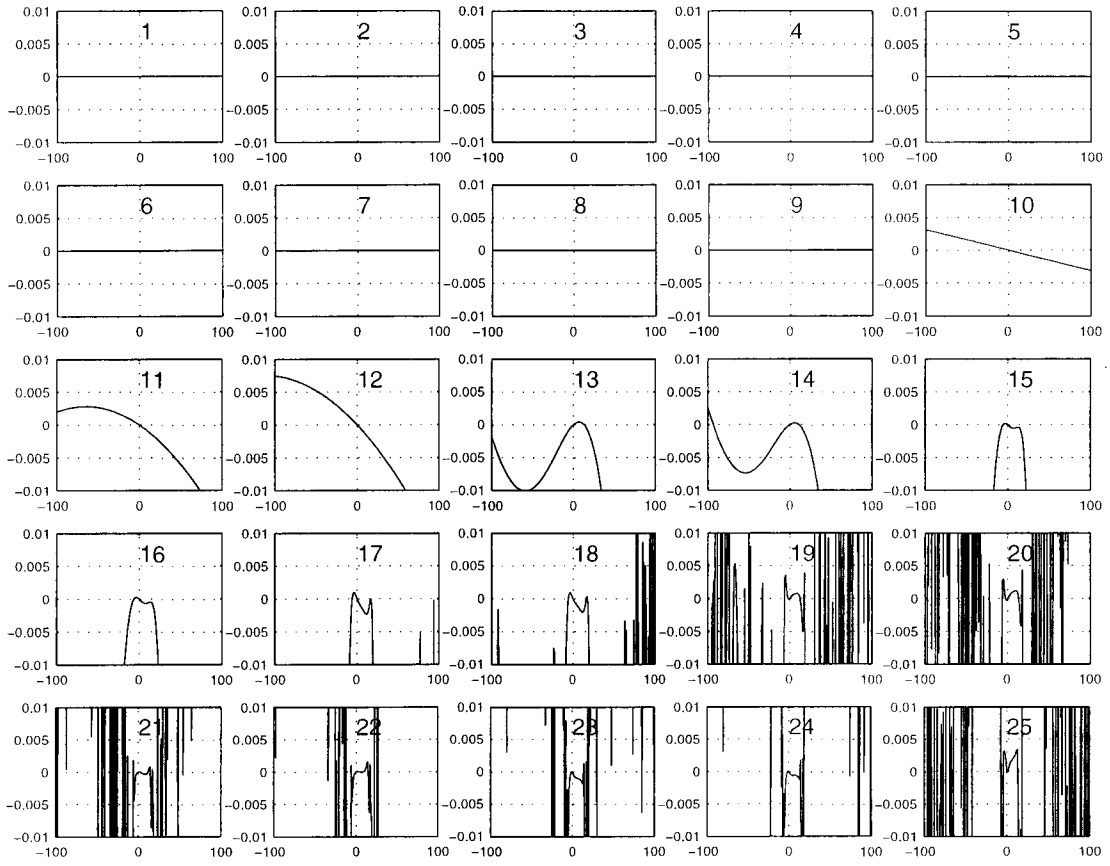

Figure 5.9: Adjusted Two-Field-Sector magnet model: Dip5 deviation

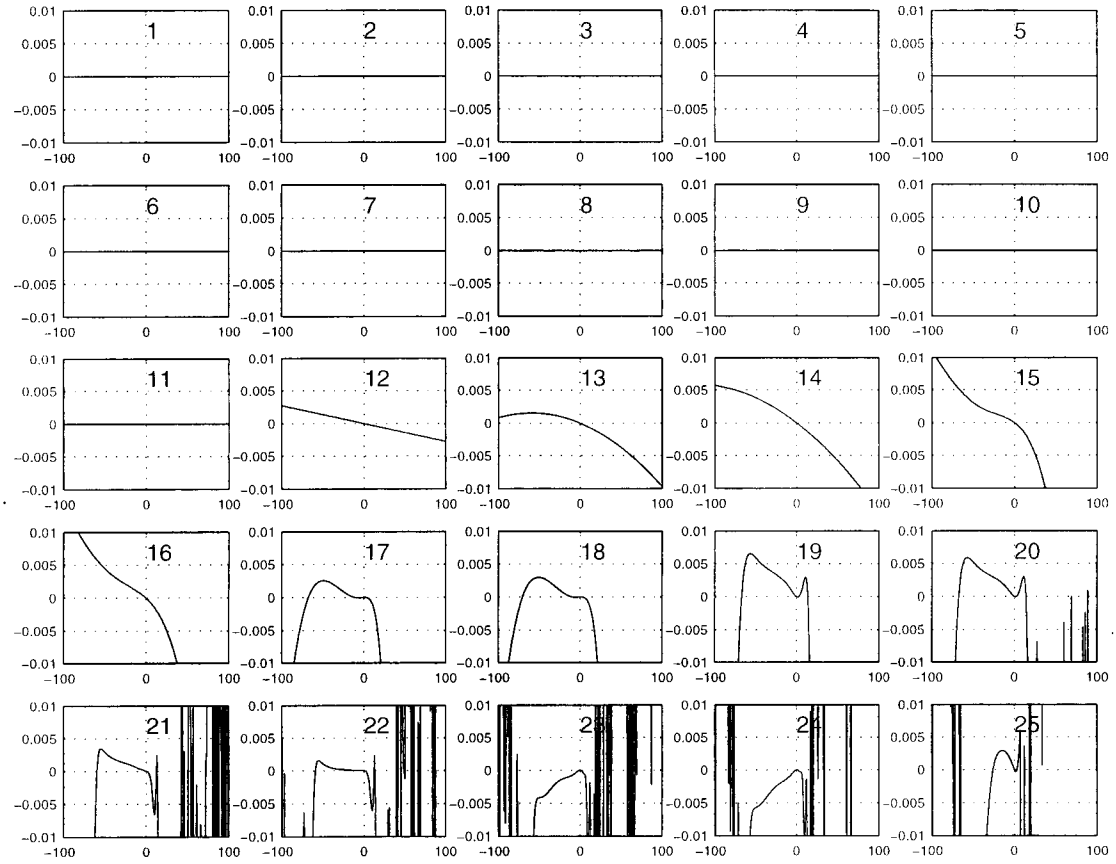

Figure 5.10: Adjusted Two-Field-Sector magnet model: Dip6 deviation

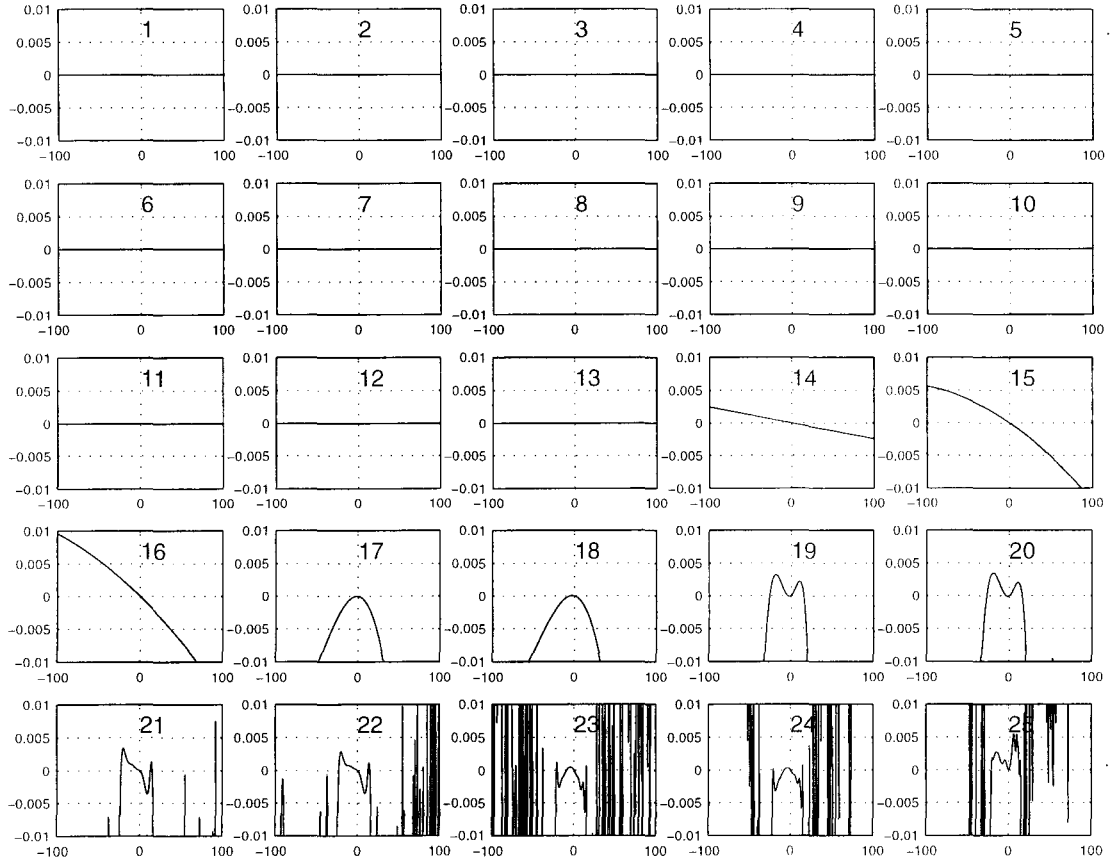

Figure 5.11: Adjusted Two-Field-Sector magnet model: Dip7 deviation

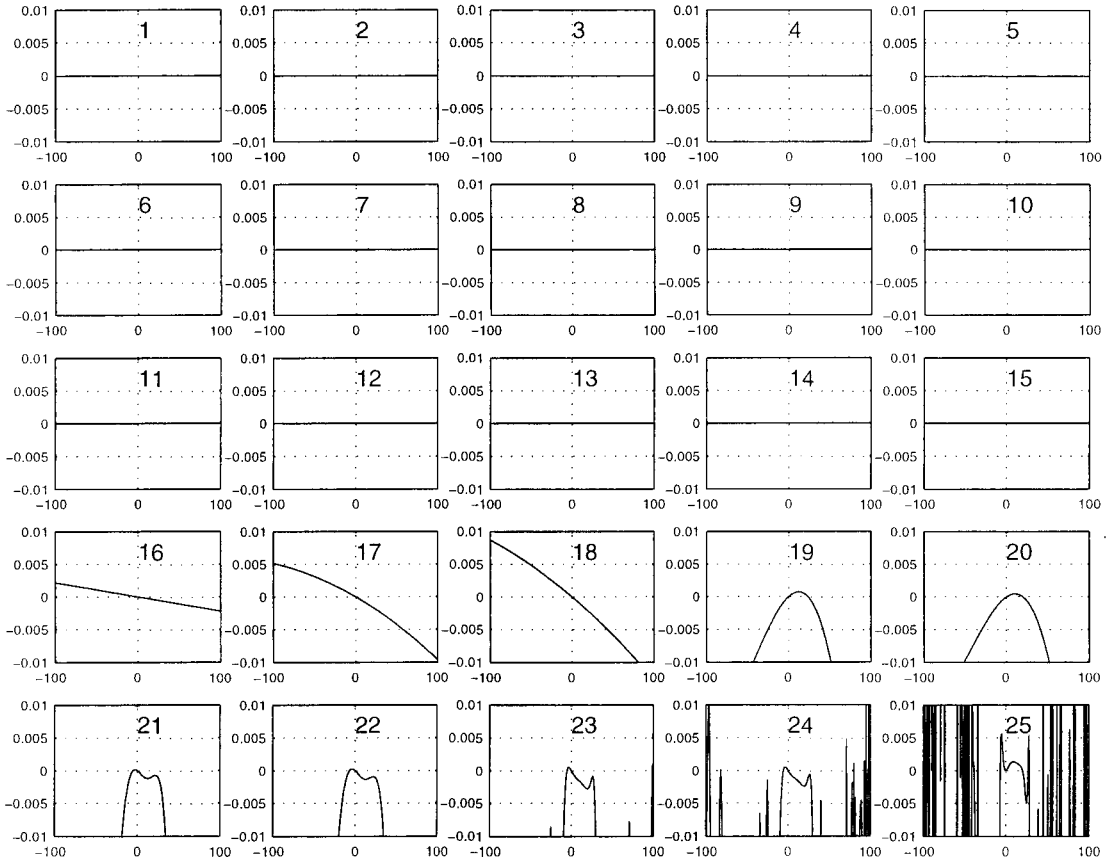

Figure 5.12: Adjusted Two-Field-Sector magnet model: Dip8 deviation

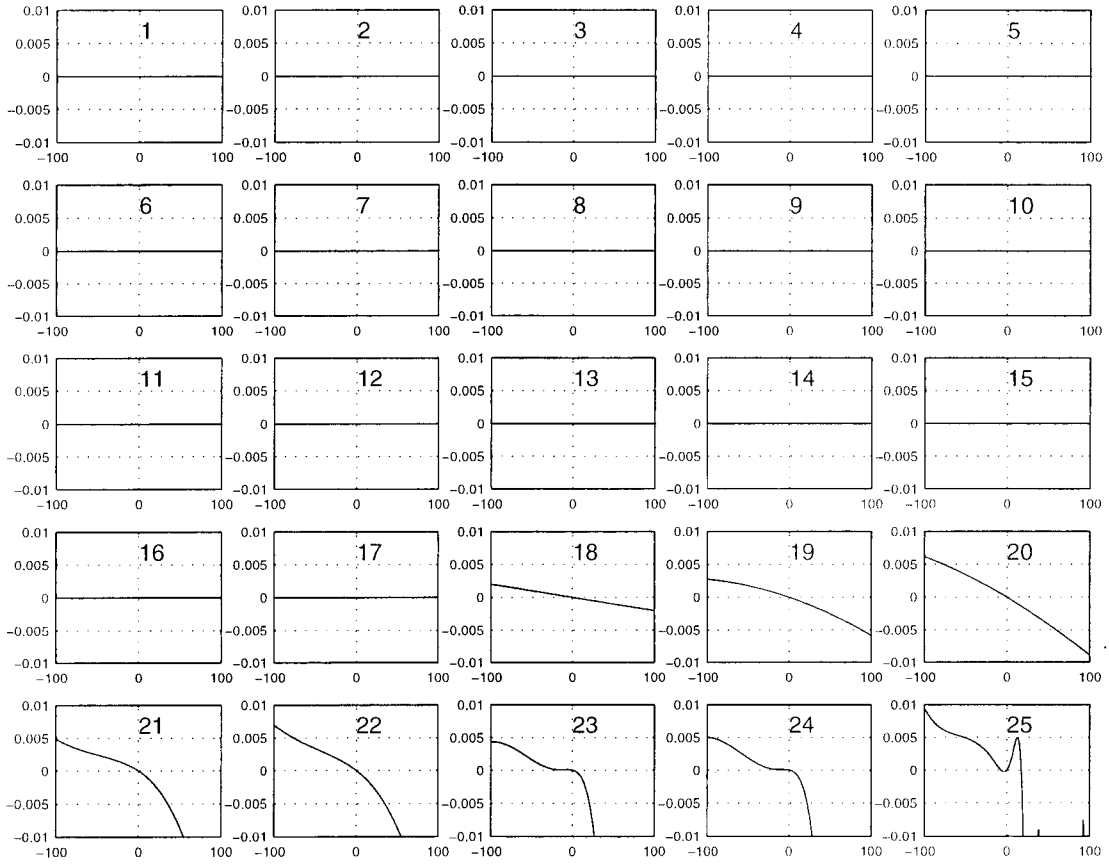

Figure 5.13: Adjusted Two-Field-Sector magnet model: Dip9 deviation

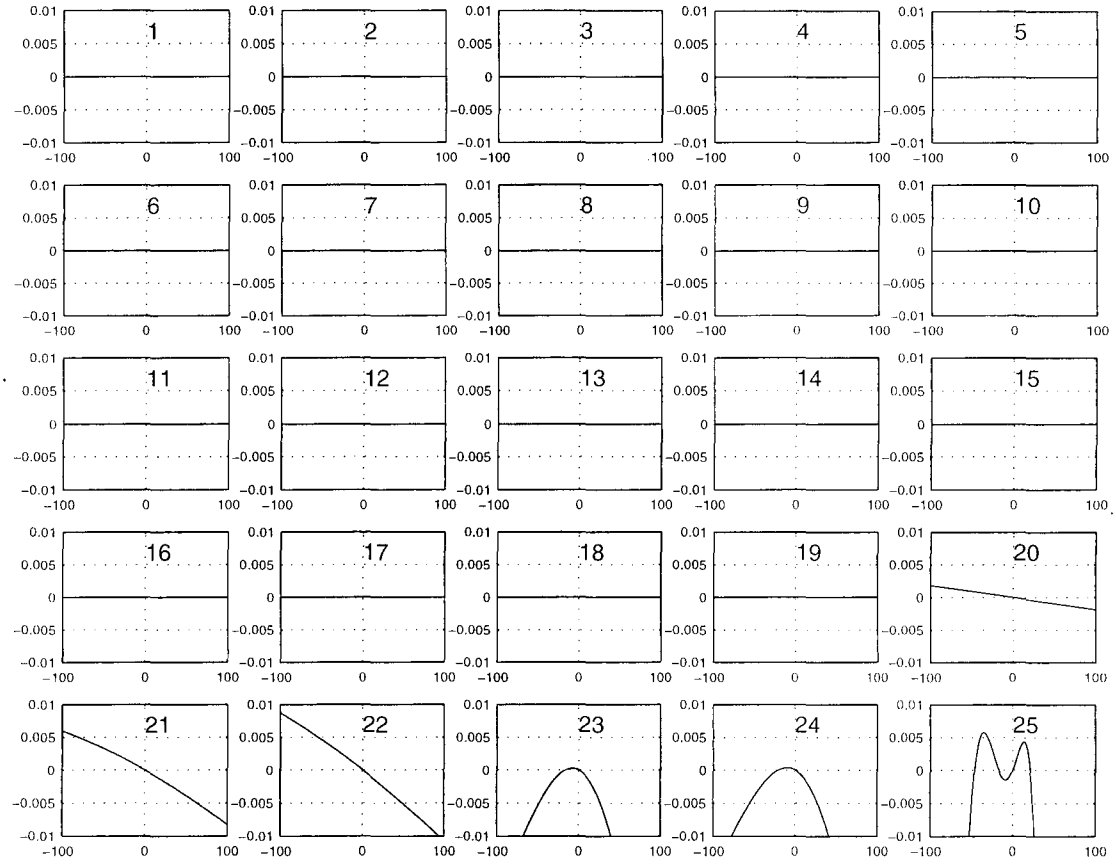

Figure 5.14: Adjusted Two-Field-Sector magnet model: Dip10 deviation

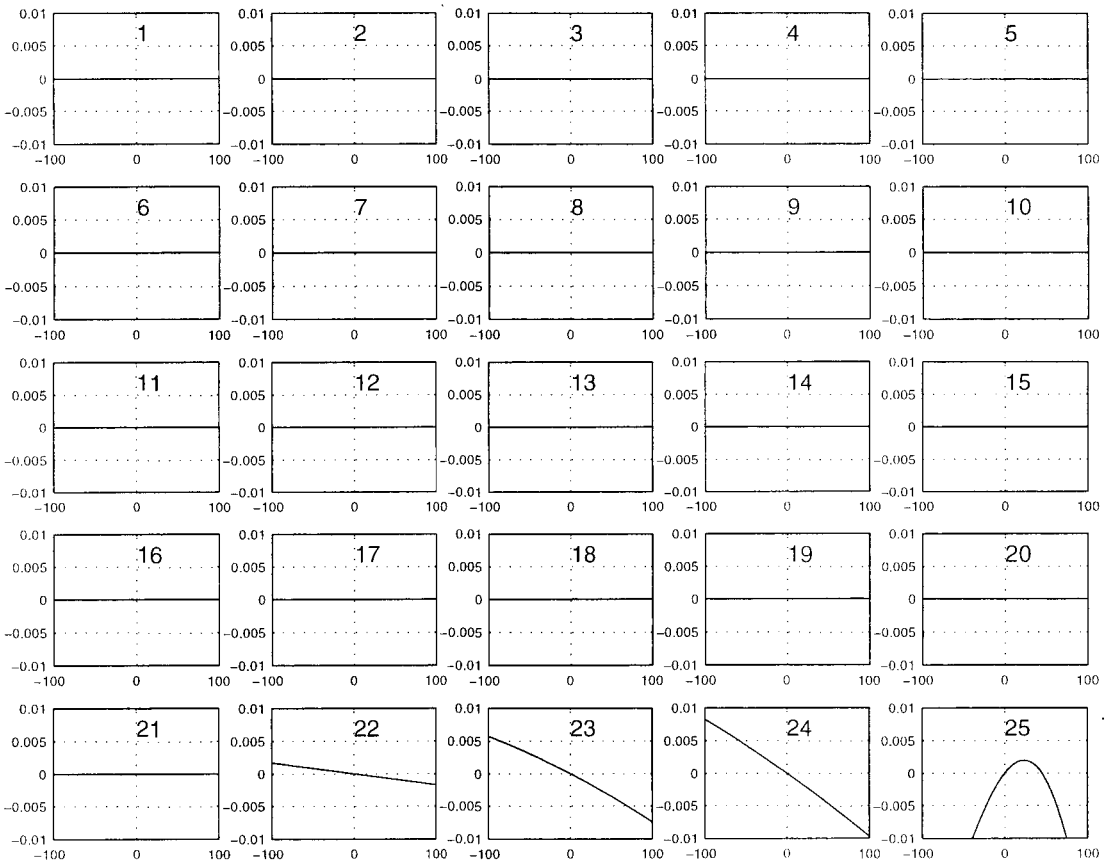

Figure 5.15: Adjusted Two-Field-Sector magnet model: Dip11 deviation

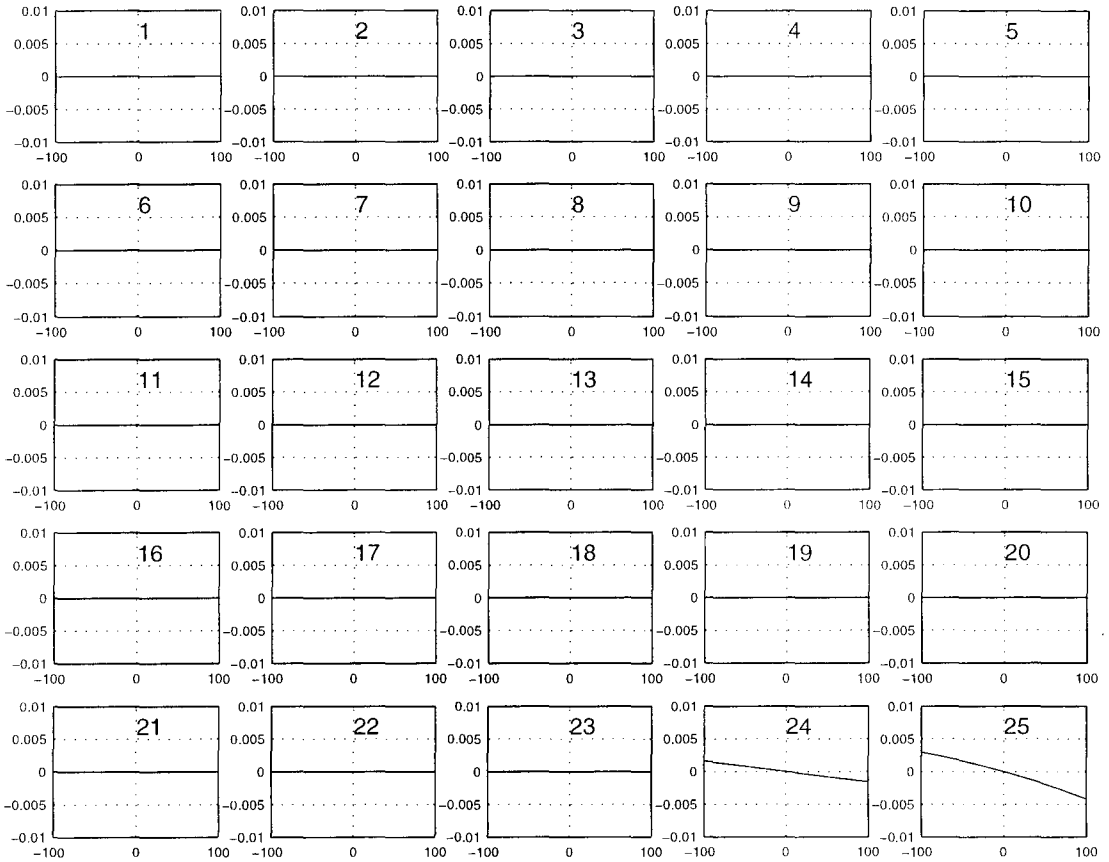

Figure 5.16: Adjusted Two-Field-Sector magnet model: Dip12 deviation